1
Nanoplasmonics: Fundamentals and Applications

Mark I. Stockman

Abstract A review of nanoplasmonics is given. This includes fundamentals, nanolocalization of optical energy and hot spots, ultrafast nanoplasmonics and control of the spatiotemporal nanolocalization of optical fields, and quantum nanoplasmonics (spaser and gain plasmonics). This chapter reviews both fundamental theoretical ideas in nanoplasmonics and selected experimental developments. It is designed both for specialists in the field and general physics readership.

Keywords Plasmonics • Nanoconcentration of optical energy • Plasmonic eigenmodes • Hot spots • Nanoscale localization • Ultrafast nanoplasmonics • Spaser • Nanolasers • Amplification and loss compensation

1.1 Introduction

1.1.1 Preamble

This is a review chapter on fundamentals of nanoplasmonics. Admittedly, the selection of the included subjects reflects the interests and expertise of the author.

We have made a conscious decision not to include such important and highly developed subject as SERS (Surface Enhanced Raman Scattering). The reason is that this subject is too large and too specialized for this chapter. There is an extensive literature devoted to SERS. This includes both reviews and original publications – see, e.g., Refs. [1–5] and a representative collective monograph [6]. Another important subject that we do not include in this review is the extraordinary transmission

M.I. Stockman (✉)
Center for Nano-Optics (CeNO) and Department of Physics and Astronomy,
Georgia State University, Atlanta, GA 30340, USA
e-mail: mstockman@gsu.edu

B. Di Bartolo et al. (eds.), *Nano-Structures for Optics and Photonics*,
NATO Science for Peace and Security Series B: Physics and Biophysics,
DOI 10.1007/978-94-017-9133-5_1,

of light through subwavelength holes – there are extensive literature and excellent reviews on this subject – see, e.g., [7–11]. Also, due to limitations of time and space we do not cover systematically a subject of particular interest to us: the adiabatic nanoconcentration of optical energy [12]. There are many important experimental developments and promising applications of this phenomenon [12–22]. This field by itself is large enough to warrant a dedicated review. We only briefly touch this subject in Sect. 1.4.5.

Another important class of questions that we leave mostly outside of this review chapter are concerned with applications of nanoplasmonics. Among this applications are sensing, biomedical diagnostics, labels for biomedical research, nanoantennas for light-emitting diodes, etc. There exist a significant number of reviews on the applications of nanopalsmonics, of which we mention just a few below, see also a short feature article [23]. Especially promising and important are applications to cancer treatment [24, 25], sensing and solar energy conversion to electricity [26], and photo-splitting of hydrogen [27] and water [28] ("artificial photosynthesis" for solar production of clean fuels).

Presently, nanoplasmonics became a highly developed and advanced science. It would have been an impossible task to review even a significant part of it. We select some fundamental subjects in plasmonics of high and general interest. We hope that our selection reflects the past, shows the modern state, and provides an attempt of a glimpse into the future. Specifically, our anticipation is that the ultrafast nanoplasmonics, nanoplasmonics in strong field, and the spaser as a necessary active element will be prominently presented in this future. On the other hand, it is still just a glimpse into it.

1.1.2 Composition of the Chapter

In Sect. 1.2, we present an extended introduction to nanoplasmonics. Then we consider selected subfields of nanoplasmonics in more detail. Nanoplasmonics is presently a rather developed science with a number of effects and rich applications [23]. In the center of our interest and, in our opinion, the central problem of nanoplasmonics is control and monitoring of the localization of optical energy in space on the nanometer scale and in time on the femtosecond or even attosecond scale.

In Sect. 1.3, we consider ultimately small nanoplasmonic systems with size less or on the order of skin depth l_s where we employ the so-called quasistatic approximation to describe in an analytical form the nanolocalized optical fields, their eigenmodes and hot spots, and introduce the corresponding Green's functions and solutions. This section is focused on the spatial nanoconcentration of the local optical fields.

In Sect. 1.4 we present ideas and results of ultrafast nanoplasmonics and coherent control of nanoscale localization of the optical fields, including control in time with femtosecond resolution. We will describe both theoretical ideas and some experimental results.

One of the most important problems of the nanoplasmonics, where only recently solutions and first experimental results have been obtained, is the active and gain nanoplasmonics. Its major goal is to create nanoscale quantum generators and amplifiers of optical energy. In Sect. 1.5, we present theory and a significant number of experimental results available to date regarding the spaser and related polaritonic spasers (nanolasers or plasmonic lasers). We also consider a related problem of loss compensation in metamaterials.

1.2 Basics of Nanoplasmonics

1.2.1 Fundamentals

Nanoplasmonics is a branch of optical condensed matter science devoted to optical phenomena on the nanoscale in nanostructured metal systems. A remarkable property of such systems is their ability to keep the optical energy concentrated on the nanoscale due to modes called surface plasmons (SPs). It is well known [29] and reviewed below in this chapter that the existence of SPs depends entirely on the fact that dielectric function ε_m has a negative real part, $\mathrm{Re}\,\varepsilon_m < 0$. The SPs are well pronounced as resonances when the losses are small enough, i.e., $\mathrm{Im}\,\varepsilon_m \ll -\mathrm{Re}\,\varepsilon_m$. This is a known property of a good plasmonic metal, valid, e.g., for silver in the most of the visible region. We will call a substance a good plasmonic metal if these two properties

$$\mathrm{Re}\,\varepsilon_m < 0\,, \quad \mathrm{Im}\,\varepsilon_m \ll -\mathrm{Re}\,\varepsilon_m \tag{1.1}$$

are satisfied simultaneously.

There is a limit to which an electromagnetic wave can be concentrated. We immediately note that, as we explain below, nanoplasmonics is about concentration of *electromechanical* energy at optical frequencies (in contrast to electromagnetic energy) on the nanoscale.

The scale of the concentration of electromagnetic energy is determined by the wavelength and can be understood from Fig. 1.1a. Naively, let us try to achieve the strongest light localization using two parallel perfect mirrors forming an ideal Fabry-Perot resonator. A confined wave (resonator mode) should propagate normally to the surface of the mirrors. In this case, its electric field $\mathbf{E}$ is parallel to the surface of the mirror. The ideal mirror can be thought of as a metal with a zero skin depth that does not allow the electric field of the wave $\mathbf{E}$ to penetrate inside. Therefore the field is zero inside the mirror and, due to the Maxwell boundary conditions, must be zero on the surface of the mirror. The same condition should be satisfied at the surface of the second mirror. Thus, the length L of this Fabry-Perot cavity should be equal an integer number n of the half-wavelengths of light in the inner dielectric, $L = n\lambda/2$. The minimum length of this resonator is, obviously $\lambda/2$. This implies that light cannot be confined tighter than to a length of $\lambda/2$ in each direction, with the minimum modal volume of $\lambda^3/8$.

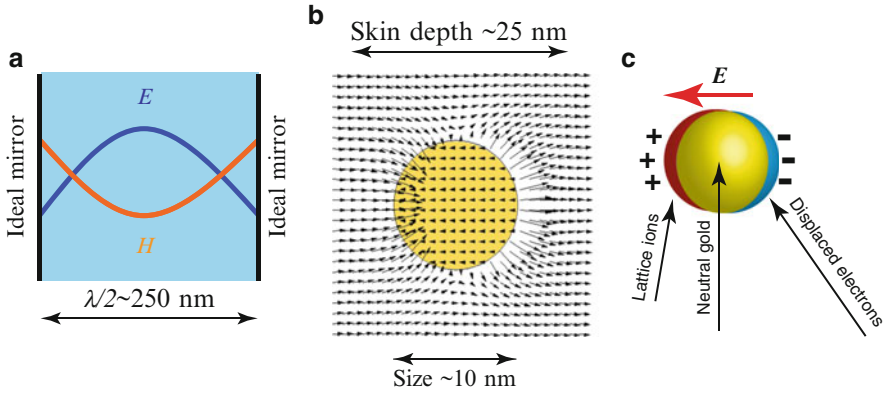

Fig. 1.1 (**a**) Localization of optical fields by ideal mirrors and (**b**) by a gold nanoparticle. (**c**) Schematic of charge separation is shown in panel

One may think that it is impossible to achieve a localization of the optical energy to smaller volume than $\lambda^3/8$ by any means, because the ideal mirrors provide the best confinement of electromagnetic waves. There are two implied assumptions: (i) The optical energy is electromagnetic energy, and (ii) The best confinement is provided by ideal mirrors. Both these assumptions must be abandoned to achieve nanolocalization of optical energy.

Consider a nanoplasmonic system whose size is less than or comparable to the skin depth

$$l_s = \lambda\!\!\!^{-}\left[\mathrm{Re}\left(\frac{-\varepsilon_m^2}{\varepsilon_m+\varepsilon_d}\right)^{1/2}\right]^{-1}, \tag{1.2}$$

where $\lambda\!\!\!^{-} = \lambda/(2\pi) = \omega/c$ is the reduced vacuum wavelength. For for single-valence plasmonic metals (silver, gold, copper, alkaline metals) $l_s \approx 25$ nm in the entire optical region.

For such a plasmonic nanosystem with $R \lesssim l_s$, the optical electric field penetrates the entire system and drives oscillations of the metal electrons. The total energy of the system in this case is a sum of the potential energy of the electrons in the electric field and their mechanical kinetic energy. While the magnetic field is present, non-relativistic electrons' interaction with it is weak proportional to a small parameter $v_F/c \sim \alpha \sim 10^{-2}$, where v_F is the electron speed at the Fermi surface, c is speed of light, and $\alpha = e^2/\hbar c$ is the fine structure constant. Thus in this limit, which is conventionally called quasistatic, the effects of the magnetic component of the total energy is relatively small. Hence, this total energy is mostly *electromechanical* (and not electromagnetic) energy. (At this point, it may be useful to refer to Eq. (1.107), which expresses the Brillouin formula for the total energy $\mathscr{E}$ of a system in such a quasistatic case.) This is why the wavelength, which determines the length

scale of the energy exchange between the electric and magnetic components of an electromagnetic wave does not define the limit of the spatial localization of energy. Because the size of the system R is smaller than any electromagnetic length scale, of which smallest is l_s, it is R that defines the spatial scale of the optical energy localization. Thus the optical fields are confined on the nanoscale, and their spatial distribution scales with the system's size. This physical picture is at the heart of the nanoplasmonics.

Consider as an example a gold nanosphere of radius $R < l_s$, e.g., $R \sim 10\,\text{nm}$, subjected to a plane electromagnetic wave, as shown in Fig. 1.1b. The field penetrates the metal and causes displacement of electrons with respect to the lattice resulting in the opposite charges appearing at the opposing surfaces, as illustrated in Fig. 1.1c. The attraction of these charges causes a restoring force that along with the (effective) mass of the electrons defines an electromechanical oscillator called a SP. When the frequency ω_{sp} of this SP is close to the frequency of the excitation light wave, a resonance occurs leading to the enhanced local field at the surface, as illustrated in Fig. 1.1b.

This resonant enhancement has also an adverse side: loss of energy always associated with a resonance. The rate of this loss is proportional to $\text{Im}\,\varepsilon_m$ [30]. This leads to a finite lifetime of SPs. The decay rate of the plasmonic field γ is $\propto (\text{Im}\,\varepsilon_m)^{-1}$. In fact, it is given below in this chapter as Eq. (1.49) in Sect. 1.3.4. This expression has originally been obtained in Ref. [31] and is also reproduced below for convenience,

$$\gamma = \frac{\text{Im}\, s(\omega)}{\frac{\partial \text{Re}\, s(\omega)}{\partial \omega}} \approx \frac{\text{Im}\, \varepsilon_m(\omega)}{\frac{\partial \text{Re}\varepsilon_m(\omega)}{\partial \omega}}\,, \tag{1.3}$$

where

$$s(\omega) = \frac{\varepsilon_d}{\varepsilon_d - \varepsilon_m(\omega)} \tag{1.4}$$

is Bergman's spectral parameter [29]. Note that γ does not explicitly depend on the system geometry but only on the optical frequency ω and the permittivities. However, the system's geometry determines the SP frequency ω and, thus, implicitly enters these equations. The approximate equality in Eq. (1.3) is valid for relatively small relaxation rates, $\gamma \ll \omega$. Apart from γ, an important parameter is the so-called quality factor

$$Q = \frac{\omega}{2\gamma} \approx \frac{\omega \frac{\partial \text{Re}\varepsilon_m(\omega)}{\partial \omega}}{2\text{Im}\, \varepsilon_m(\omega)} \tag{1.5}$$

The quality factor determines how many optical periods free SP oscillations occur before field decays. It also shows how many times the local optical field at the surface of a plasmonic nanoparticle exceeds the external field.

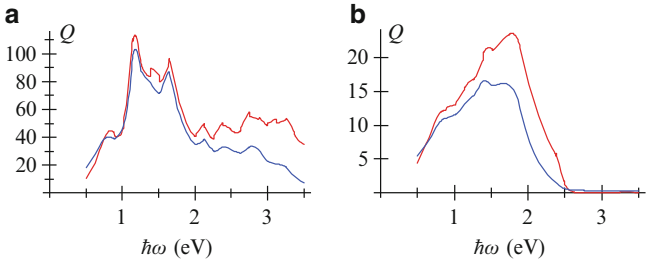

Fig. 1.2 (**a**) Quality factor Q for silver and (**b**) for gold calculated according to Eq. (1.5) (*red*) and Eq. (1.6) (*blue*) as a function of frequency ω

Note that another definition of the quality factor, which is often used, is

$$Q = \frac{-\mathrm{Re}\,\varepsilon_m(\omega)}{\mathrm{Im}\,\varepsilon_m(\omega)}\,. \tag{1.6}$$

The SP quality factors Q calculated according to Eqs. (1.5) and (1.6) for gold and silver using the permittivity data of Ref. [32] are shown in Fig. 1.2. The Q-factors found from these two definitions agree reasonably well in the red to near-infrared (near-ir) region but not in the yellow to blue region of the visible spectrum. The reason is that these two definitions would be equivalent if metals' permittivity were precisely described by a Drude-type formula $\mathrm{Re}\,\varepsilon_m(\omega) = -\omega_p^2/\omega^2$, where ω_p is the bulk plasma frequency; $\hbar\omega_p \approx 9\,\mathrm{eV}$ for one-electron metals such as silver, copper, gold, and alkaline metals. This formula is reasonably well applicable in the red and longer wavelength part of the spectrum, but not in the yellow to blue part where the d-band transitions are important. Note that silver is a much better plasmonic metal than gold: its Q-factor is several-fold of that of gold.

The finite skin depth of real metals leads to an effect related to nanoplasmonic confinement: a phase shift $\Delta\varphi$ for light reflected from a metal mirror deviates from a value of $\Delta\varphi = \pi$ characteristic of an ideal metal. As suggested in Ref. [33], this allows for ultrasmall cavities whose length $L \ll \lambda$. While generally this is a valid idea, there two problems with Ref. [33] that affect the validity of its specific results. First, the Fresnel reflection formulas used in this article to calculate $\Delta\varphi$ are only valid for infinite surfaces but not for the "nanomirrors" in a nanocavity. Second, Eq. (1.1) of this article expressing Q is incorrect: it contains in the denominator a quantity $\partial\left[\omega\mathrm{Im}\varepsilon_m(\omega)\right]/\partial\omega$ instead of $2\mathrm{Im}\,\varepsilon_m(\omega)$ as in Eq. (1.5). The correct expression [30] for Ohmic losses defining the Q-factor, which we reproduce as Eq. (1.108), is proportional to $\mathrm{Im}\,\varepsilon_m(\omega)$ as in Eq. (1.5) and not to $\partial\left[\omega\mathrm{Im}\varepsilon_m(\omega)\right]/\partial\omega$, which constitutes a significant difference.

The lifetime τ of the SPs is related to the spectral width as

$$\tau = \frac{1}{2\gamma}\,. \tag{1.7}$$

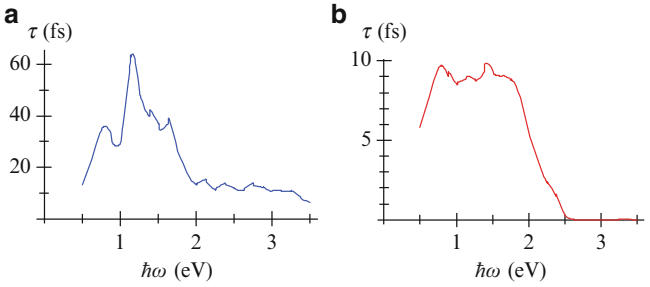

Fig. 1.3 (**a**) Lifetime τ of SPs for silver and (**b**) for gold calculated according to Eq. (1.7) as a function of frequency ω

Note that the SP spectral width γ, quality factor Q, and lifetime τ depend explicitly only on frequency ω and the type of the metal (permittivity ε_m) but not on the nanosystem's geometry or surrounding dielectric. However, this geometry and the ambient-dielectric permittivity ε_d do affect the modal frequency and enter the corresponding Eqs. (1.3), (1.5), and (1.7) implicitly via ω.

The dependence of the SP lifetime τ on frequency ω calculated for gold and silver using permittivity [32] is illustrated in Fig. 1.3. This lifetime is in the range 10–60 fs for silver and 1–10 fs for gold in the plasmonic region. These data show that nanoplasmonic phenomena are ultrafast (femtosecond).

However, the fastest linear response time τ_c of SPs, as any other linear response system, depends not on the relaxation time but solely on the bandwidth. In fact, it can be calculated as a quarter period (i.e., a time interval between zero and the maximum field) of the beating between the extreme spectral components of the plasmonic oscillations,

$$\tau_c = \frac{1}{4}\frac{2\pi}{\Delta\omega}\,, \tag{1.8}$$

where $\Delta\omega$ is the spectral bandwidth of the plasmonic spectrum. For gold and silver, this bandwidth is the entire optical spectrum, i.e., $\hbar\Delta\omega \approx 3.5\,\text{eV}$. If aluminum is included among system's plasmonic metals, this bandwidth is increased to $\hbar\Delta\omega \approx 9\,\text{eV}$. This yields this coherent reaction time $\tau_c \sim 100\,\text{as}$. Thus nanoplasmonics is potentially attosecond science.

While the characteristic size of a nanoplasmonic system should be limited from the top by the skin depth, $R \ll l_s$, it is also limited from the bottom by the so called nonlocality length l_{nl} – see, e.g., [34,35]. This nonlocality length is the distance that an electron with the Fermi velocity v_F moves in space during a characteristic period of the optical field,

$$l_{nl} \sim v_F/\omega \sim 1\,\text{nm}\,, \tag{1.9}$$

where an estimate is shown for the optical spectral region. For metal nanoparticles smaller than l_{nl}, the spatial dispersion of the dielectric response function and the related Landau damping cause broadening and disappearance of SP resonances [34, 35].

Thus, we have arrived at the basic understanding of the qualitative features of nanoplasmonics. Consider a plasmonic nanosystem whose size R satisfies a condition $l_{nl} \ll R \ll l_s$. This nanosystem is excited by an external field in resonance. In this case, the local optical field in the vicinity of such a nanosystem is enhanced by a factor $\sim Q$, which does not depend on R. The spatial extension of the local field scales with the size of the nanosystem $\propto R$. This is because $R \ll l_s$, and l_s is the smallest electromagnetic length; thus there is no length in the system that R can be comparable to. When the external field changes, the local field relaxes with the relaxation time Q/ω that does not depend on R; the lifetimes of the SP are in the femtosecond range.

In many cases of fundamental and applied significance, the size of a nanosystem can be compoarable to or even greater than l_s but still subwavelength, $\lambda \gg R \gtrsim l_s$. In such a case, the coupling to far-field radiation and radiative losses may greatly increase as we will discuss below in Sects. 1.2.2 and 1.2.3. Another important subfield of nanoplasmonics that is related to extended systems is the surface plasmon polaritons – see, e.g., a collective monograph [36]. We consider some polaritonic phenomena relevant to coherent control below in Sect. 1.4.5.

1.2.2 Nanoantennas

Consider a molecule situated in the near-field of a metal plasmonic nanosystem. Such a molecule interacts not with the external field but with the local optical field $\mathbf{E}(\mathbf{r})$ at its location $\mathbf{r}$. The interactions Hamiltonian of such a molecule with the optical field is $H' = -\mathbf{E}(\mathbf{r})\mathbf{d}$, where $\mathbf{d}$ is the dipole operator of this molecule. Note that a modal expansion of the quantized local field operator is given below in this chapter by Eq. (1.64).

Consequently, the enhanced local fields cause enhancement of radiative and nonradiative processes in which such a molecule participate. In particular, the rates of both the excitation and emission are enhanced proportionality to the local field intensity, i.e., by a factor of $\sim Q^2$. This effect is often referred to as nanoantenna effect [37–64] in analogy with the common radio-frequency antennas For the recent review of the concept and applications of optical nanoantennas see Ref. [65]. Currently, the term nanoantenna or optical antenna is used so widely that it has actually became synonymous with the entire field of nanoplasmonics: any enhancement in nanoplasmonic systems is called a nanoantenna effect.

General remarks about the terms “nanoantenna” or “optical antenna” are due. The term “antenna” has originated in the conventional radio-frequency technology where it is used in application to receivers for devices that convert the wave energy of far-field radio waves into local (near-field) electric power used to drive

the input circuitry. For transmitters, antennas perform the inverse transformation: from the local field electric power to that of the emitted radio waves. Due to the general properties of time reversal symmetry there is no principal difference between the receiving and transmitting antennas: any receiving antenna can work as a transmitting one and vice versa. The mechanism of the efficiency enhancement in the radio frequency range is a combination of spatial focusing (e.g., for parabolic antennas) and resonant enhancement (e.g., for a dipole antenna). In all cases, the size of the radio antenna is comparable to or greater than the wavelength. Thus one may think that a receiving antenna collects energy from a large geometric cross section and concentrates it in a small, subwalength area.

The receiving antennas in radio and microwave technology are loaded by matched impedance loads that effectively withdraw the energy from them. This suppresses the radiation by such antennas but simultaneously dampens their resonances and makes them poor resonators.

In majority of cases, the optical antennas are not matched-loaded because they are designed not to transduce energy efficiently but to create high local fields interacting with molecules or atoms, which do not load these antennas significantly. (There are exceptions though: for instance, the nanoantenna in Ref. [66] is loaded with an adiabatic nanofocusing waveguide.) The unloaded antennas efficiently loose energy to radiation (scattering), which dampens their resonances.

A question is whether this concept of collecting energy form a large geometric cross section is a necessary paradigm also in nanoplasmonics. The answer is no, which is clear already from the fact that the enhancement of the rates of both the excitation and emission of a small chromophore (molecule, rear earth ion, etc.) in the near field of a small ($R \lesssim l_s$) plasmonic nanoparticle is $\sim Q^2$ and *does not depend* on the nanoparticle size R. This enhancement is due to the coherent resonant accumulation of the energy of the SPs during $\sim Q$ plasmonic oscillations and has nothing to do with the size of the nanoparticle. Thus such an enhancement does not quite fit into the concept of antennas as established in the radio or microwave technology.

Another test of the nanoantenna concept is whether the efficiency of a nanoantenna is necessarily increased with its size. The answer to this question is generally no. This is because for plasmonic nanoparticles, with the increase of size there is also an increased radiative loss – see below Sect. 1.2.3. In contrast, for many types of radio-frequency antennas (dish antennas or microwave-horn antennas, for instance), the efficiency does increase with the size.

1.2.3 Radiative Loss

As we described above in conjunction with Fig. 1.1c, the interaction of optical radiation with a nanoplasmonic system occurs predominantly via the dipole oscillations. The radiative decay of SPs occur via spontaneous emission of photons, which is a process that does not exist in classical physics and requires a quantum-mechanical

treatment. To find the radiative life time of a SP state quantum-mechanically, we need to determine the transitional dipole matrix element $\mathbf{d}_{0p}$ between the ground state $|0\rangle$ and a single-plasmon excited state $|p\rangle$. To carry out such a computation consistently, one needs to quantize the SPs, which we have originally done in Ref. [31] and present below in Sect. 1.5.4.1.

However, there is a general way to do it without the explicit SP quantization, which we present below in this section. We start with the general expression for the polarizability α of a nanosystem obtained using quantum mechanics – see e.g., Ref. [67], which near the plasmon frequency has a singular form,

$$\alpha = \frac{1}{\hbar}\frac{\left|\mathbf{d}_{0p}\right|^2}{\omega - \omega_{sp}} , \tag{1.10}$$

where ω_{sp} is the frequency of the resonant SP mode. This can compared with the corresponding pole expression of the polarizability of a nanoplasmonic system, which is given below as Eq. (1.55), to find absolute value of the matrix element $\left|\mathbf{d}_{0p}\right|$.

Here, for the sake of simplicity, we will limit ourselves to a particular case of a nanosphere whose polarizability is given by a well-known expression

$$\alpha = R^3 \frac{\varepsilon_m(\omega) - \varepsilon_d}{\varepsilon_m(\omega) + 2\varepsilon_d} , \tag{1.11}$$

where R is the radius of the nanosphere. The SP frequency $\omega = \omega_{sp}$ corresponds to the pole of α, i.e., it satisfies an equation

$$\mathrm{Re}\, \varepsilon_m(\omega_{sp}) = -2\varepsilon_d , \tag{1.12}$$

where we neglect $\mathrm{Im}\, \varepsilon_m$. In the same approximation, near $\omega = \omega_{sp}$, we obtain from Eq. (1.11),

$$\alpha = -3R^3\varepsilon_d \left[\left(\omega - \omega_{sp}\right)\frac{\partial \mathrm{Re}\, \varepsilon_m(\omega_{sp})}{\partial \omega_{sp}}\right]^{-1} . \tag{1.13}$$

Comparing the two pole approximations of Eqs. (1.10) and (1.13), we obtain the required expression for the dipole moment of a quantum transition between the ground state and the SP state,

$$\left|\mathbf{d}_{0p}\right|^2 = \hbar 3R^3\varepsilon_d \left[\frac{\partial \mathrm{Re}\, \varepsilon_m(\omega_{sp})}{\partial \omega_{sp}}\right]^{-1} . \tag{1.14}$$

Consider the well-known quantum-mechanical expression for the dipole-radiation rate (see, e.g., Ref. [67]),

$$\gamma^{(r)} = \frac{4}{3}\frac{\omega^3\sqrt{\varepsilon_d}}{\hbar c^3}\left|\mathbf{d}_{0p}\right|^2 . \tag{1.15}$$

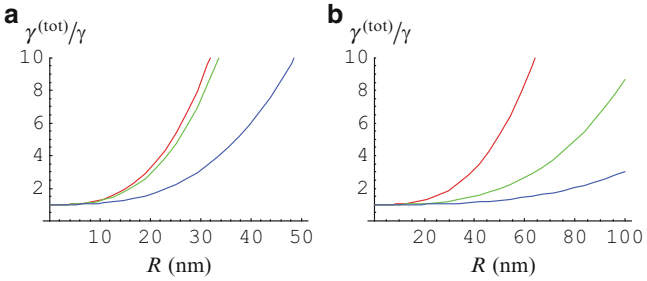

Fig. 1.4 Ratio of the rates of the total to internal loss, $\gamma^{(tot)}/\gamma$, for a nanosphere as a function of its radius R for (**a**) silver and (**b**) gold. The *blue*, *green*, and *red lines* correspond to the embedding dielectric with $\varepsilon_d = 1, 2$, and 5, respectively. The computations are made at the SP frequency ω_{sp}, which for these value of ε_d is for silver $\hbar\omega_{sp} = 3.5, 3.2, 2.5\,\text{eV}$, and for gold $\hbar\omega_{sp} = 2.6, 2.4, 2.0\,\text{eV}$, correspondingly

Substituting Eq. (1.14) into (1.15), we obtain the desired expression for the quantum-mechanical rate of the radiative decay of the SP state as

$$\gamma^{(r)} = 4\varepsilon_d^{3/2}\left(\frac{\omega_{sp}R}{c}\right)^3\left[\frac{\partial \text{Re}\,\varepsilon_m(\omega_{sp})}{\partial\omega_{sp}}\right]^{-1}. \tag{1.16}$$

Note that for losses not very large (which is the case in the entire plasmonic region for noble metals), the Kramers-Kronig relations for $\varepsilon_m(\omega)$ predict [30] that

$$\frac{\partial \text{Re}\,\varepsilon_m(\omega_{sp})}{\partial\omega_{sp}} > 0\,, \tag{1.17}$$

which guarantees that $\gamma^{(r)} > 0$ in Eq. (1.16).

Comparing this expression to Eq. (1.3) (see also Eq. (1.49)), we immediately conclude that, in contrast to the internal (radiationless) loss rate γ, the radiative rate is proportional to the volume of the system (i.e., the number of the conduction electrons in it), which is understandable. Thus for systems small enough, the radiative rate can be neglected. The quality factor of the SP resonance is actually defined by the total decay rate $\gamma^{(tot)}$ (cf. Eq. (1.5)),

$$Q = \frac{\omega_{sp}}{2\gamma^{(tot)}}\,, \quad \gamma^{(tot)} = \gamma + \gamma^{(r)}\,. \tag{1.18}$$

Therefore, Q is lower for larger nanoparticles, tending to a constant for small R. To quantify it, we find a ratio

$$\frac{\gamma^{(tot)}}{\gamma} = 1 + \frac{4}{\text{Im}\,\varepsilon_m(\omega_{sp})}\left(\frac{\sqrt{\varepsilon_d}\,\omega_{sp}R}{c}\right)^3. \tag{1.19}$$

We illustrate behavior of this rate ratio of the total to internal loss, $\gamma^{(tot)}/\gamma$, in Fig. 1.4. General conclusion is that the radiative loss for silver is not very important for nanospheres in the true quasistatic regime, i.e., for $R < l_s \approx 25\,\text{nm}$ but is

a dominant mechanism of loss for $R > 30\,\text{nm}$, especially in high-permittivity environments. In contrast, for gold the radiative loss is not very important in the quasistatic regime due to the much higher intrinsic losses, except for a case of a relatively high ambient permittivity, $\varepsilon_d = 5$.

Though it is outside of the scope of this chapter, we would like to point out that there is a general approach to combat radiative losses in relatively large nanoparticles. This is related to the well-known Fano resonances originally discovered by Ugo Fano in atomic spectra [68]. These resonances can be described in the following way. In certain cases of optical excitation, when two quantum paths lead to the same final quantum state of the system, the resonance peaks have specific asymmetric line shapes due to the interference of these quantum paths.

An analogous phenomenon is also known in nanoplasmonics and metamaterials [69–77]. They can be explained in the following way [77]. Apart from bright plasmonic resonances with high transitional dipole moment, there are also dark ones [78], which by themselves are not very prominent in optical spectra. However, if a bright resonance and a dark resonance coexist in a certain spectral range – which is not unlikely, because the bright resonances are wide spanning relatively wide wavelength ranges – then their optical fields interfere. This interference significantly enhances the manifestation of the dark resonance: it acquires strength from the bright resonance and shows itself as an asymmetric peak-and-dip profile characteristic of a Fano resonance. An important, albeit counterintuitive, property of the Fano resonances is that, exactly at the frequency of the Fano dip, the hot spots of the nanolocalized optical fields in the nanosystem are strongest. This is because at this frequency the nanosystem emits minimal light intensity and, consequently, it does not wastefully deplete the energy of the plasmon oscillations. This leads to a decreased radiative loss and a high quality resonance quality factor.

Thus at the frequency of a Fano resonance, the radiative loss is significantly suppressed. The width of the Fano resonances is ultimately determined by the internal (Ohmic) losses described by $\text{Im}\,\varepsilon_m$. Summarizing, the Fano resonances enable one using relatively large nanoplasmonic particles or plasmonic metamaterials to achieve narrow spectral features with high local fields. These can be applied to plasmonic sensing and to produce spasers and nanolasers – see Sect. 1.5.

1.2.4 Other Important Issues of Plasmonics in Brief

There are other very important issues and directions of investigation in plasmonics that we will not be able to review in any details in this chapter due to the limitations of time and space. Below we will briefly list some of them.

1.2.4.1 Enhanced Mechanical Forces in Nanoplasmonic Systems

The resonantly enhanced local fields in the vicinity of plasmonic nanoparticles lead to enhanced nanolocalized forces acting between the nanoparticles, see, e.g.,

Refs. [79–85]. A perspective application of plasmonically-enhanced forces is optical manipulation (tweezing) of micro- and nanoparticles [86–92].

Another direction of research is opened up by the recently introduced theoretically surface-plasmon-induced drag-effect rectification (SPIDER) [93], which is based on transfer of the linear momentum from decaying surface-plasmon polaritons (SPPs) to the conduction electrons of a metal nanowire. The SPIDER effect bears a promise to generate very high terahertz fields in the vicinity of the metal nanowire.

1.2.4.2 Interaction Between Electrons and Surface Plasmons

The surface plasmonics, as it is called today, originated by a prediction of electron energy losses for an electron beam in thin metal films below the energy of the bulk plasmons [94]. This is how coherent electronic excitations called SPPs today were predicted. Soon after this prediction, the SPP-related energy losses were experimentally confirmed [95, 96]. Presently, the electron energy loss spectroscopy (EELS) in nanopalsmonics is a thriving field of research. We refer to a recent review [97] for further detail.

A distinct and original direction of research is control of mechanical motion of metal nanoparticles using electron beams [98]. It is based on the same principles as optically-induced forces. The difference in this case is that the SP oscillations in nanoparticles are excited locally, with an Angstrom precision, by a beam of fast electrons – see also Sect. 1.2.4.1 above.

There are other important phenomena in plasmonics based on electron-SP interaction called nonlocality [99]. One of them is dephasing of plasmons causing their decay into electron-hole pairs, which is called Landau damping, contributing to $\mathrm{Im}\,\varepsilon_m$. There is necessarily a related phenomenon of spatial dispersion contributing to $\mathrm{Re}\,\varepsilon_m$. These become important for plasmonics when the size of the nanosystem become too small, $R \lesssim l_{nl}$ – see Eq. (1.9). The nonlocality and Landau damping degrade plasmonic effects. The nonlocal effects lead to an increased decay rate of dipolar emitters at metal surfaces [34] and limits resolution of plasmonic imaging, making the so-called "perfect" lens [100] rather imperfect [35]. In aggregates, the nonlocality of dielectric responses causes reduction of local fields and widening of plasmonic resonances [101]. These broadening effects have initially been taken into account purely phenomenologically by adding an additional contribution to the width of plasmonic resonances $\sim A/\tau_{nl}$, where $A = const$ [102]. Practically, if the size of a nanoparticle is less then 3 nm, the non-local broadening of the SP resonances is very significant; otherwise, it can be neglected in a reasonable approximation.

The above-mentioned publications [34, 35, 99, 101] on the nonlocality phenomena are based on a semi-phenomenological approach where the nonlocality is treated via applying additional boundary conditions stemming from the electron scattering by the boundaries of the plasmonic system. A more advanced approach to nonlocality in nanoplasmonics, albeit treatable only for very small, $R \lesssim 1$ nm, nanoparticles, is based on an ab initio quantum-chemical approach of time-dependent density functional theory (usually abbreviated as TD-DFT) [103–109].

It shows that while for larger particles and relatively large spacing between them ($\gtrsim$1 nm), the semi-phenomenological models work quite well, for smaller nanoparticles and gaps the predicted local fields are significantly smaller. This is understandable because in ab initio theories there are phenomena that are important in the extremely small nanosystem such as a significant dephasing due to the stronger coupling between the collective plasmon and one-particle electron degrees of freedom, discreetness of the one-electron spectrum, spill-out of the conduction-band electrons (extension of their wave function outside of the lattice region) and the corresponding undescreening of the d-band electrons, and simply the discreetness of the lattice.

In the latest set of publications, e.g., [108, 109], this approach is called quantum nanoplasmonics. We would argue that this approach is traditionally called quantum chemistry because what is found from the TD-DFT quantum-mechanically is the dielectric response (susceptibility or polarizability) of the nanosystems. However, even to calculate theoretically the permittivity of a bulk method, one has to employ quantum-mechanical many-body approaches such as the random-phase approximation, self-consistent random-phase approximation (or GW-aproximation), or TD-DFT, etc. The only difference from the above-sited works is that for bulk metals the size effects are absent. Therefore permittivities can be adopted from experimental measurements such as Ref. [32, 110].

Based on the arguments of the preceding paragraph, we would reserve the therm "quantum plasmonics" for the subfields of nanoplasmonics studying phenomena related to quantum nature and behavior SPs and SPPs. This term has been proposed in our 2003 paper [31] introducing the spaser as a quantum generator of nanolocalized optical fields – see Sect. 1.5 and references sited therein. A related field of studies devoted to quantum behavior of single SPPs also can reasonably be called quantum plasmonics as proposed later in Refs. [111, 112].

While the decay of SP excitations is usually a parasitic phenomenon, there are some effects that completely depend on it. One of them is the SPIDER [93] mentioned above in Sect. 1.2.4.1. It is based on the transfer of the energy and momentum from SPPs to the conduction electrons, which microscopically occurs through the decay of the SPPs into electron-hole pairs leading to production of hot electrons.

Yet another range of phenomena associated with a plasmon-dephasing decay into incoherent electron-hole pairs (Landau damping) has come to the forefront lately. This is the plasmon-assisted and enhanced generation of a dc electric current due to rectification in Schottky diodes involving hot electrons [61, 113–115]. This phenomenon is promising for applications to photodetection and solar energy conversion. Note that the use of the Schottky contacts between the plasmonic metal and a semiconductor permits one to eliminate a requirement that the photon energy $\hbar\omega$ is greater that the band gap. This is replaced by a much weaker requirement that $\hbar\omega$ is greater than a significantly lower Schottky-barrier potential [116].

1.2.4.3 Nonlinear Photoprocesses in Nanoplasmonics

As became evident from the first steps of what now is called nanoplasmonics, the enhanced local fields in resonant metal nanosystems bring about strongly enhanced nonlinear responses [117–120].

Nonlinear nanoplasmonics is presently a very large and developed field. Some of its phenomena related to coherent control and spasing are discussed in Sects. 1.4, and 1.5. Here we will give a classification of the nonlinear nanoplasmonic phenomena and provide some examples, not attempting at being comprehensive.

Nonlinearities in nanoplasmonics can occur in the nanostructured plasmonic metal, in the embedding medium (dielectric), or in both. Correspondingly, we classify them as intrinsic, extrinsic, or combined. As an independent classification, these nonlinearities can be classified as weak (perturbative) or strong (nonperturbative). The perturbative nonlinearities can be coherent (or parametric), characterized by nonlinear polirizabilities [121] and incoherent such as nonlinear absorption, two-photon fluorescence, surface-enhanced hyper-Raman scattering (SEHRS) [122], nonlinear photo-modification, two-photon electron emission [123], etc.

Let us give some examples illustrating a variety of nonlinear photoprocesses in nanoplasmonics.

- Second-harmonic generation from nanostructured metal surfaces and metal nanoparticles [57, 124–132] is a coherent, perturbative (second-order or three-wave mixing), intrinsic nonlinearity.
- Enhanced four wave mixing (sum- or difference frequency generation) at metal surfaces [133] is a coherent, perturbative (third-order or four-wave), intrinsic nonlinearity.
- Another four-wave mixing process in a hybrid plasmonic-photonic waveguide involves nonlinearities in both metal and dielectric [134] and, therefore, is classified as a coherent, combined, perturbative third-order nonlinear process.
- An all-optical modulator consisting of a plasmonic waveguide covered with CdSe quantum dots [135] is based on a perturbative third-order, combined nonlinearity. To the same class belongs a nanoscale-thickness metamaterial modulator [136].
- An ultrafast all-optical modulator using polaritons in an aluminum plasmonic waveguide is based on perturbative third-order, intrinsic nonlinearity [137]. There are arguments that this nonlinearity is incoherent, based on interband population transfer of carriers [137].
- Nonperturbative (strong-field), coherent, extrinsic nonlinearity is plasmon-enhanced generation of high harmonics [138] where the enhanced nanoplasmonic fields excite argon atoms in the surrounding medium. Spaser [31] belongs to the same class where the nonlinearity is the saturation of the gain medium by the coherent plasmonic field [139]. The same is true for the loss compensation by gain [140, 141].
- Intrinsic perturbative nonlinearities in nanoplasmonics stemming from a redistribution of the electron density caused by the ponderomotive forces of nanoplasmonic fields have been predicted for surface plasmon polaritons [93, 142].

An intrinsic nonperturbative nonlinear process is the predicted plasmon soliton [143] where strong local optical fields in a plasmonic waveguide cause a significant redistribution of the conduction-electron density.

- There are also relevant strongly-nonlinear processes in non-plasmonic materials that are based on nanolocalized fields and are very similar to those in plasmonics. Among them are near-field enhanced electron acceleration from dielectric nanospheres with intense few-cycle laser fields [144]. Another such a process is a strong optical-field electron emission from tungsten nanotips controlled with an attosecond precision [145].
- Finally, a recently predicted phenomenon of metallization of dielectrics by strong optical fields [146, 147] belongs to a new class of highly-nonlinear phenomena where strong optical fields bring a dielectric nanofilm into a plasmonic metal-like state.

1.3 Nanolocalized Surface Plasmons (SPs) and Their Hot Spots

1.3.1 SPs as Eigenmodes

Assuming that a nanoplasmonic system is small enough, $R \ll \lambda\!\!\!^{-}, R \lesssim l_s$, we employ the so-called quasistatic approximation where the Maxwell equations reduce to the continuity equation for the electrostatic potential $\varphi(\mathbf{r})$,

$$\frac{\partial}{\partial \mathbf{r}} \varepsilon(\mathbf{r}) \frac{\partial}{\partial \mathbf{r}} \varphi(\mathbf{r}) = 0 \,. \tag{1.20}$$

The systems permittivity (dielectric function) varying in space is expressed as

$$\varepsilon(\mathbf{r}) = \varepsilon_m(\omega) \Theta(\mathbf{r}) + \varepsilon_d [1 - \Theta(\mathbf{r})] \,. \tag{1.21}$$

Here $\Theta(\mathbf{r})$ is the so-called characteristic function of the nanosystem, which is equal to 1 when $\mathbf{r}$ belongs to the metal and 0 otherwise. We solve this equation following the spectral theory developed in Refs. [78, 148, 149].

Consider a nanosystem excited by an external field with potential $\varphi_0(\mathbf{r})$ at an optical frequency ω. This potential is created by external charges and, therefore, satisfies the Laplace equation within the system,

$$\frac{\partial^2}{\partial \mathbf{r}^2} \varphi_0(\mathbf{r}) = 0 \,. \tag{1.22}$$

We present the field potential as

$$\varphi(\mathbf{r}) = \varphi_0(\mathbf{r}) + \varphi_1(\mathbf{r}) \,, \tag{1.23}$$

where $\varphi_1(\mathbf{r})$ is the local field.

Substituting Eq. (1.23) into Eq. (1.20) and taking Eqs. (1.21) and (1.22) into account, we obtain a second-order elliptic equation with the right-hand side that describes the external excitation source,

$$\frac{\partial}{\partial \mathbf{r}} \Theta(\mathbf{r}) \frac{\partial}{\partial \mathbf{r}} \varphi_1(\mathbf{r}) - s(\omega) \frac{\partial^2}{\partial \mathbf{r}^2} \varphi_1(\mathbf{r}) = -\frac{\partial}{\partial \mathbf{r}} \Theta(\mathbf{r}) \frac{\partial}{\partial \mathbf{r}} \varphi_0(\mathbf{r}) \,, \tag{1.24}$$

where $s(\omega)$ is Bergman's spectral parameter [148] defined by Eq. (1.4).

As a convenient basis to solve this field equation we introduce eigenmodes (SPs) with eigenfunctions $\varphi_n(\mathbf{r})$ and the corresponding eigenvalues s_n, where n is the full set of indices that identify the eigenmodes. These eigenmodes are defined by the following generalized eigenproblem,

$$\frac{\partial}{\partial \mathbf{r}} \Theta(\mathbf{r}) \frac{\partial}{\partial \mathbf{r}} \varphi_n(\mathbf{r}) - s_n \frac{\partial^2}{\partial \mathbf{r}^2} \varphi_n(\mathbf{r}) = 0 \,, \tag{1.25}$$

where the eigenfunctions $\varphi_n(\mathbf{r})$ satisfy the homogeneous Dirichlet-Neumann boundary conditions on a surface S surrounding the system. These we set as

$$\varphi_1(\mathbf{r})|_{\mathbf{r}\in S} = 0 \,, \quad \text{or} \quad \mathbf{n}(\mathbf{r}) \frac{\partial}{\partial \mathbf{r}} \varphi_1(\mathbf{r}) \bigg|_{\mathbf{r}\in S} = 0 \,, \tag{1.26}$$

with $\mathbf{n}(\mathbf{r})$ denoting a normal to the surface S at a point of $\mathbf{r}$. These boundary conditions (1.26) are essential and necessary to define the eigenproblem.

From Eqs. (1.25), (1.26) applying the Gauss theorem, we find

$$s_n = \frac{\int_V \Theta(\mathbf{r}) \left| \frac{\partial}{\partial \mathbf{r}} \varphi_n(\mathbf{r}) \right|^2 \mathrm{d}^3 r}{\int_V \left| \frac{\partial}{\partial \mathbf{r}} \varphi_n(\mathbf{r}) \right|^2 \mathrm{d}^3 r} \,. \tag{1.27}$$

From this equation, it immediately follows that all the eigenvalues are real numbers and

$$1 \geq s_n \geq 0 \,. \tag{1.28}$$

Physically, as one can judge from Eq. (1.27), an eigenvalue of s_n is the integral fraction of the eigenmode (surface plasmon) intensity $|\partial \varphi_n(\mathbf{r}) / \partial \mathbf{r}|^2$ that is localized within the metal.

Because the SP eigenproblem is real, and all the eigenvalues s_n are all real, the eigenfunctions φ_n can also be chosen real, though are not required to be chosen in such a way. Physically, it means that the quasistatic nanoplasmonic eigenproblem is time-reversible.

For the eigenproblem (1.25) and (1.26), we can introduce a scalar product of any two functions ψ_1 and ψ_2 as

$$(\psi_1 | \, \psi_2) = \int_V \left[\frac{\partial}{\partial \mathbf{r}} \psi_2^*(\mathbf{r}) \right] \left[\frac{\partial}{\partial \mathbf{r}} \psi_1(\mathbf{r}) \right] d^3 r \,, \tag{1.29}$$

This construct possesses all the necessary and sufficient properties of a scalar product: it is a binary, Hermitian self-adjoined, and positive-defined operation. It is easy to show that the eigenfunctions of Eqs. (1.25) and (1.26) are orthogonal. They can be normalized as

$$(\varphi_n | \varphi_m) = \delta_{nm} \,, \tag{1.30}$$

1.3.2 Inhomogeneous Localization of SPs and Hot Spots of Local Fields

One of the most fundamental properties of eigenmodes is their localization. By nature, the SP eigenmodes of small nanoplasmonic systems are localized and non-propagating. This generally follows from the fact that the eigenproblem (1.25) is real and has real eigenvalues, implying time-reversal invariance and, consequently, zero current carried by any eigenmode.

From the early days of nanoplasmonics, there has been keen attention paid to the localization of SP eigenmodes, because it was immediately clear that absence of any characteristic wavelength of the localized SPs leads to the possibility of their concentration in nanoscopic volumes of the space [117, 120, 150]. Many early publications claimed that the SPs in disordered nanoplasmonics systems, e.g., fractal clusters, experience Anderson localization [151–157].

However, a different picture of the SP localization, named inhomogeneous localization, has been introduced [78, 158–161]. In this picture of inhomogeneous localization, eigenmodes of very close frequencies with varying degree of localization, from strongly localized at the minimum scale of the system to delocalized over the entire nanosystem coexist. This phenomenon of inhomogeneous localization has been experimentally confirmed recently [162]. The eigenmodes experiencing the Anderson localization are dark, corresponding to dipole-forbidden transitions, and thus can only be excited from the near field [78].

A related phenomenon is the formation of hot spots in local fields of nanoplasmonic system that we introduced in Refs. [158, 159, 163, 164]. As characteristic of the inhomogeneous localization, the energy is localized by different SP eigenmodes at vastly different scales. However, it is the localization at the minimum scale that gives the highest local fields and energy density; these tightly-localized modes are the most conspicuous in the near-field intensity distributions as the hot spots. The hot spots exist in all kind of nanoplasmonic system but they are especially strongly pronounced in disordered and aperiodic systems [165].

We will illustrate the hot spots and the inhomogeneous localization of the SP eigenmodes using the results of the original works that established the phenomena [158,159] using plasmonic-metal fractal clusters as objects. The model of these fractals were the so-called cluster-cluster aggregates (CCA) [166, 167]. In Fig. 1.5, we show two representative eigenmodes with Bergman's eigenvalues of $s_n = 0.3202$

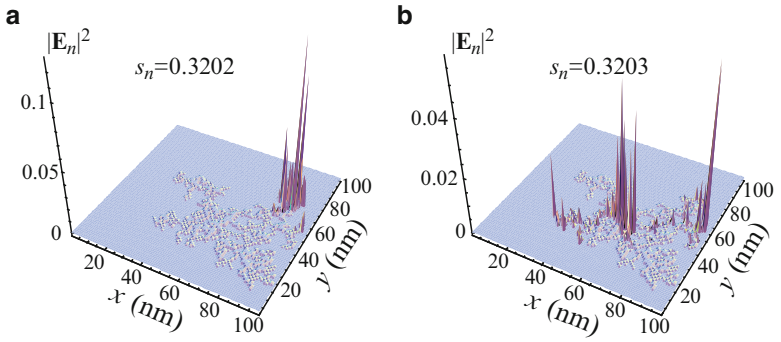

Fig. 1.5 Near-field intensity of eigenmodes computed for cluster-cluster aggregate (CCA) cluster. Square of the eigenmode electric field $|\mathbf{E}_n|^2$ is displayed against the projection of the cluster for two eigenmodes with close eigenvalues: (**a**) $s_n = 0.3202$ and (**b**) $s_n = 0.3203$. For silver embedding medium with a permittivity $\varepsilon_d \approx 2.0$, which is an approximate value for water, these modes correspond to a *blue* spectral range with $\hbar\omega \approx 3.13\,\text{eV}$ (Adapted from Ref. [158])

and $s_n = 0.3203$, which are very close in frequency (the blue spectral range for the case of silver in water). Both the eigenmodes are highly singular and are represented by sharp peaks – hot spots – that may be separated by the distances from the minimum scale of the system to the maximum scale that is on the order of the total size of the entire system. These eigenmodes possess very different topologies but very close eigenvalues and, consequently, have almost the same frequency $\hbar\omega \approx 3.13\,\text{eV}$ corresponding to the blue spectral range. This coexistence of the very different eigenmodes at the same frequency was called the inghomogeneous localization [158, 159].

The formation of host spots by the SP eigenmodes and the inhomogeneous localization of the eigenmodes are very pronounced for the fractal clusters. However, the same phenomena also take place in all dense random plasmonic systems. Physically, this phenomena is related to the absence of the characteristic length scale for SPs: the smallest electromagnetic scale is the skin depth $l_s \approx 25\,\text{nm}$, which is too large on the scale of the system to affect the SP localization. The inhomogeneous localization implies that eigenmodes can be localized on all scales but this localization is always singular. The hot spots are the concentration regions of the optical energy: sharp peaks on the minimum scale ("fine grain" size) of the system are most visible.

Note that there is a fundamental difference between the plasmonic hot spots and their counterpart in the wave optics: speckles produced by scattering of laser light from a random medium. In the speckle case, there is a characteristic size of the speckles on the order of a character distance L_s between them that is determined by diffraction:

$$L_s \sim \lambda D/A\,, \tag{1.31}$$

where λ is wavelength of light, A is an aperture (cross-size of the coherent spot of light on the scattering system), and D is the distance from the scatterer to the observation screen.

One of the plasmonic system models studied in significant detail is a random metal composite (RPC) also called a semi-continuous metal film [78, 128, 149, 156, 162, 168–171]. This is a planar system where metal occupies a given fill fraction f of the system's volume. At a low f, the RPC is a system of remote, randomly positioned metal particles. For high values of f, it is an almost continuous film with rare holes in it. For $f \approx 0.5$, there are percolation phenomena: there is a large connected random cluster of the metal extending between the boundaries of the system [172]. This connected percolation cluster is known to possess a fractal geometry.

To consider statistical measures of the SP localization, we introduce the localization radius L_n of an eigenmode, which is defined as the gyration radius of its electric field intensity $|\mathbf{E}_n(\mathbf{r})|^2$, where

$$E_n(\mathbf{r}) = -\frac{\partial}{\partial \mathbf{r}}\varphi_n(\mathbf{r}) \tag{1.32}$$

is the eigenmode electric field, as

$$L_n^2 = \int_V \mathbf{r}^2 |\mathbf{E}_n(\mathbf{r})|^2 \mathrm{d}^3 r - \left(\int_V \mathbf{r} |\mathbf{E}_n(\mathbf{r})|^2 \mathrm{d}^3 r \right)^2 . \tag{1.33}$$

We remind that due to Eq. (1.30), the eigenmode fields are normalized

$$\int_V |\mathbf{E}_n(\mathbf{r})|^2 \mathrm{d}^3 r = 1 , \tag{1.34}$$

so Eq. (1.33) is a standard definition of the gyration radius.

In Fig. 1.6a, we show the smoothed, discretized nanostructure of one particular sample of a RPC. This system is generated in the following way. We consider a volume of size, in our case, $32 \times 32 \times 32$ grid steps. In the central xz plane of this cube we randomly fill a cell of size 2×2 grid steps with metal with some probability f (fill factor or filling factor). Then we repeat this procedure with other 2×2 cells in that central xz plane. As a result, we arrive at a thin planar layer of thickness 2 grid steps in the y direction and fill factor of f in the central xz plane.

In Fig. 1.6b, we display all of the eigenmodes (SPs) of the above-described RPC in a plot of oscillator strength F_n versus localization length L_n. These eigenmodes are strikingly unusual.

First, there is a large number of eigenmodes with negligible oscillator strengths $F_n \lesssim 10^{-5}$. Note that the rounding-up relative error in our computations is $\sim 10^{-6}$, so these eigenmodes' oscillator strengths do not significantly differ from zero. Such eigenmodes do not couple to the far-field electromagnetic waves, and they can be neither observed nor excited from the far-field (wave) zone. We call them

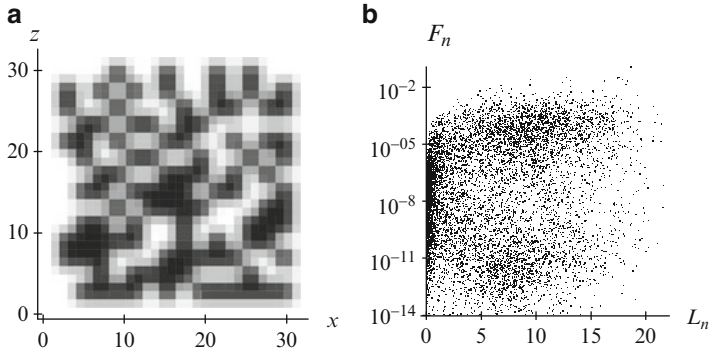

Fig. 1.6 For a planar random composite (in the xz-plane), the density of the metal component (panel (**a**)) and all eigenmodes plotted in the coordinates of oscillator strength F_n versus localization radius L_n (panel (**b**))

dark modes. They can, however, be excited and observed by NSOM (near-field scanning optical microscope) type probes in the near-field region. Such eigenmodes are also important from the computational-mathematical point of view because they are necessary for the completeness of the eigenmode set.

Second, in Fig. 1.6, there also are many eigenmodes with relatively large oscillator strengths, $F_n \gtrsim 10^{-4}$, which we call *luminous* or *bright* modes. These do couple efficiently to the far-zone fields.

Third, both the luminous and the dark modes have localization radii L_n with all possible values, from zero to one half of the diagonal system size, and with very little correlation between F_n and L_n, except for the superlocalized (zero-size) eigenmodes that are all dark. This wide range of L_n shows that *the Anderson localization does not occur for most of the modes, including all the luminous modes*. Similar to these findings in certain respects, deviations from the simple Anderson localization have been seen in some studies of the spatial structure of vibrational modes [173, 174], dephasing rates [175] in disordered solids induced by long-range (dipole-type) interactions. A direct confirmation of this picture of the inhomogeneous localization has been obtained in experiments studying fluctuations of the local density of states of localized SPs on disordered metal films [162].

To gain more insight, we show in Fig. 1.7 the local electric field intensities $|\mathbf{E}_n(\mathbf{r})|^2$ for particular eigenmodes of four extreme types, all with eigenvalues very close to $s_n = 0.2$. As a measure of the eigenmode oscillator strength, we show a normalized oscillator strength F_n. The data of Fig. 1.7 confirm the above-discussed absence of correlation between the localization length and oscillator strength, and also show that there is no correlation between the topology of the local field intensity and the oscillator strength – compare the pairs of eigenmodes: $s_n = 0.1996$ with $s_n = 0.2015$, and $s_n = 0.2$ with $s_n = 0.2011$. Note that the large and random changes of the intensities between the close eigenmodes evident in Fig. 1.7 is an underlying cause of the giant fluctuations [176] and chaos [177–179] of local fields.

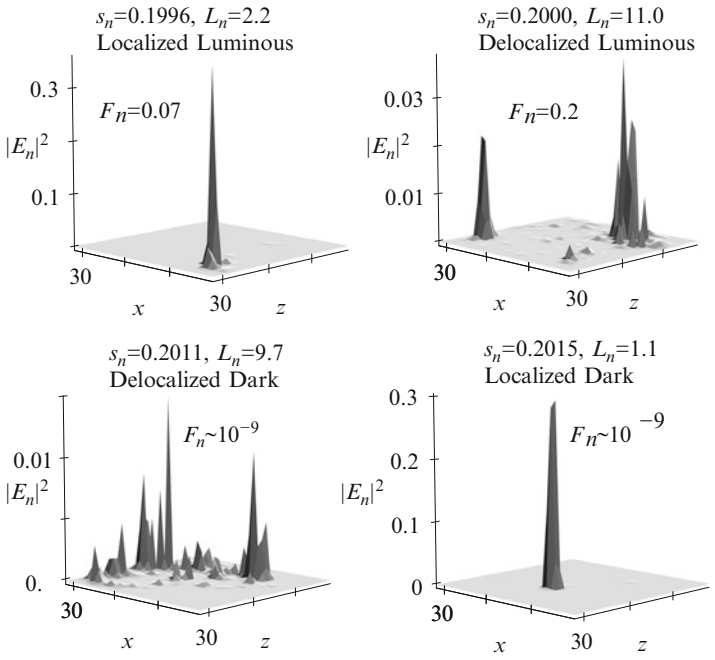

Fig. 1.7 Hot spots: Local field intensities $|\mathbf{E}_n(\mathbf{r})|^2$ of eigenmodes at the surface of the system shown in Fig. 1.6, versus spatial coordinates in the xz plane

A fundamental property of the SP eigenmodes, whether localized or delocalized, is that they may be thought of as consisting of hot spots. While the localized eigenmodes possess a single tight hot spots, the delocalized ones consist of several or many host spots. Note that the fields in the hot spots constituting a single eigenmode are coherent. In a sense, the hot spots are somewhat analogous to speckles produced by laser light scattered from a random system. However, such speckles are limited by the half-wavelength of light and cannot be smaller than that. In contrast, there is no wavelength limitations for the SP hot spots. They are limited only by the minimum scale of the underlying plasmonic system.

1.3.3 Retarded Green's Function and Field Equation Solution

Retarded Green's function $G^r(\mathbf{r}, \mathbf{r}'; \omega)$ of field equation (1.24), by definition, satisfies the same equation with the Dirac δ-function on the right-hand side,

$$\left[\frac{\partial}{\partial \mathbf{r}}\Theta(\mathbf{r})\frac{\partial}{\partial \mathbf{r}} - s(\omega)\frac{\partial^2}{\partial \mathbf{r}^2}\right] G^r(\mathbf{r}, \mathbf{r}'; \omega) = \delta(\mathbf{r} - \mathbf{r}') \,, \tag{1.35}$$

We expand this Green's function over the eigenfunctions φ_n using the orthonormality Eq. (1.30), obtaining

$$G^r(\mathbf{r}, \mathbf{r}'; \omega) = \sum_n \frac{\varphi_n(\mathbf{r})\, \varphi_n(\mathbf{r}')^*}{s(\omega) - s_n} \,. \tag{1.36}$$

This expression for Green's function is exact (within the quasistatic approximation) and contains the maximum information on the linear responses of a nanosystem to an arbitrary excitation field at any frequency. It satisfies all the general properties of Green's functions due to the analytical form of Eq. (1.36) as an expansion over the eigenmodes (surface plasmons). This result demonstrates separation of geometry of a nanosystem from its material properties and the excitation field. The eigenfunctions $\varphi_n(\mathbf{r})$ and eigenvalues s_n in Eq. (1.36) depend only on geometry of the nanosystem, but not on its material composition or the optical excitation frequency. In contrast, the spectral parameter $s(\omega)$ depends only on the material composition and the excitation frequency, but not on the system's geometry. One of the advantages of this approach is in its applications to numerical computations: the eigenproblem has to be solved only once, and then the optical responses of the nanosystem are determined by Green's function that can be found by a simple summation in Eq. (1.36).

This Green's function is called retarded because it describes responses that occur necessarily at later time moments with respect to the forces that cause them. (Note that this name and property have nothing to do with the electromagnetic retardation, which is due to the finite speed of light and is absent in the quasistatic approximation.) This property, also called Kramers-Kronig causality, is mathematically equivalent to all singularities of $G^r(\mathbf{r}, \mathbf{r}'; \omega)$ as a function of complex ω being situated in the lower half-plane. Consequently, $G^r(\mathbf{r}, \mathbf{r}'; \omega)$ as a function of ω satisfies the Kramers-Kronig dispersion relations [30]. By the mere form of the spectral expansion (1.36), this Green's function satisfies all other exact analytical properties. This guarantees that in numerical simulations it will possess these properties irrespectively of the numerical precision with which the eigenproblem is solved. This insures an exceptional numerical stability of computational Green's function approaches.

Once the Green's function is found from Eq. (1.36), the local optical field potential is found as contraction of this Green's function with the excitation potential $\varphi_0(\mathbf{r})$ as

$$\varphi_1(\mathbf{r}) = -\int_V G^r(\mathbf{r}, \mathbf{r}'; \omega) \frac{\partial}{\partial \mathbf{r}'} \Theta(\mathbf{r}') \frac{\partial}{\partial \mathbf{r}'} \varphi_0(\mathbf{r}')\, \mathrm{d}^3 r' \,. \tag{1.37}$$

From Eqs. (1.23) and (1.37) using the Gauss theorem, we obtain an expression for the field potential $\varphi(\mathbf{r})$ as a functional of the external (excitation) potential $\varphi_0(\mathbf{r})$,

$$\varphi(\mathbf{r}) = \varphi_0(\mathbf{r}) - \int_V \varphi_0(\mathbf{r}') \frac{\partial}{\partial \mathbf{r}'} \Theta(\mathbf{r}') \frac{\partial}{\partial \mathbf{r}'} G^r(\mathbf{r}, \mathbf{r}'; \omega)\, \mathrm{d}^3 r' \,. \tag{1.38}$$

Finally, differentiating this, we obtain a closed expression for the optical electric field $\mathbf{E}(\mathbf{r})$ as a functional of the excitation (external) field $\mathbf{E}^{(0)}(\mathbf{r})$ as

$$E_\alpha(\mathbf{r}) = E^{(0)}_\alpha(\mathbf{r}) + \int_V G^r_{\alpha\beta}(\mathbf{r},\mathbf{r}';\omega)\Theta(\mathbf{r}')E^{(0)}_\beta(\mathbf{r}')\,\mathrm{d}^3r' \,, \tag{1.39}$$

where $\alpha, \beta, \ldots$ are Euclidean vector indices ($\alpha, \beta, \cdots = x, y, z$) with summation over repeated indices implied; the fields are

$$\mathbf{E}(\mathbf{r}) = -\frac{\partial\varphi(\mathbf{r})}{\partial\mathbf{r}} \,, \quad \mathbf{E}^{(0)}(\mathbf{r}) = -\frac{\partial\varphi_0(\mathbf{r})}{\partial\mathbf{r}} \,, \tag{1.40}$$

and the tensor (dyadic) retarded Green's function is defined as

$$G^r_{\alpha\beta}(\mathbf{r},\mathbf{r}';\omega) = \frac{\partial^2}{\partial r_\alpha \partial r'_\beta} G^r(\mathbf{r},\mathbf{r}';\omega) \,. \tag{1.41}$$

One of the exact properties of this Green's function is its Hermitian symmetry,

$$G^r_{\alpha\beta}(\mathbf{r},\mathbf{r}';\omega) = G^r_{\beta\alpha}(\mathbf{r}',\mathbf{r};-\omega)^* \,. \tag{1.42}$$

If the excitation is an optical field, its wave front is flat on the scale of the nanosystem, i.e., $\mathbf{E}^{(0)} = \text{const}$. Then from Eq. (1.39) we get

$$E_\alpha(\mathbf{r}) = \left[\delta_{\alpha\beta} + g_{\alpha\beta}(\mathbf{r},\omega)\right] E^{(0)}_\beta \,, \tag{1.43}$$

where the local field enhancement (tensorial) factor is a contraction of the retarded dyadic Green's function,

$$g_{\alpha\beta}(\mathbf{r},\omega) = \int_V G^r_{\alpha\beta}(\mathbf{r},\mathbf{r}';\omega)\Theta(\mathbf{r}')\,\mathrm{d}^3r' \,. \tag{1.44}$$

1.3.4 SP Modes as Resonances

Each physical eigenmode is described by the corresponding pole of Green's function (1.36). Close to such a pole, Green's function and, consequently, local fields (1.43) become large, which describes the surface plasmon resonance of the nanosystem. A complex frequency of such a resonance can be found from the position of the corresponding pole in the complex plane of frequency,

$$s(\omega_n - i\,\gamma_n) = s_n \,, \tag{1.45}$$

where ω_n is the real frequency of the surface plasmon, and γ_n is its spectral width (relaxation rate).

Note that we presume $\gamma_n > 0$, i.e., a negative sign of the imaginary part of the physical surface frequency. This a presumption, which is confirmed by the solution presented below in this section, is based on the standard convention of the sign of an exponential in the field temporal evolution,

$$\mathbf{E}_n(\mathbf{r}, t) \propto \exp\left[-i\left(\omega_n - i\,\gamma_n\right)t\right] \propto \exp(-\gamma_n t)\ , \tag{1.46}$$

which decays exponentially for $t \to +\infty$, as should be. The wave functions of physical surface plasmons are the familiar eigenfunctions $\varphi_n(\mathbf{r})$, i.e., those of the geometric eigenmodes. However, their physical frequencies, of course, depend on the material composition of the system.

For weak relaxation, $\gamma_n \ll \omega_n$, one finds that this real surface plasmon frequency satisfies an equation

$$\mathrm{Re}[s(\omega_n)] = s_n\ , \tag{1.47}$$

and that the surface plasmon spectral width is expressed as

$$\gamma_n = \frac{\mathrm{Im}[s(\omega_n)]}{s_n'}, \qquad s_n' \equiv \left.\frac{\partial \mathrm{Re}[s(\omega)]}{\partial\omega}\right|_{\omega=\omega_n}\ . \tag{1.48}$$

In terms of the dielectric permittivity as functions of frequency

$$s'(\omega) = \frac{\varepsilon_d}{|\varepsilon_d - \varepsilon(\omega)|^2}\mathrm{Re}\frac{\partial\varepsilon_m(\omega)}{\partial\omega}\ , \quad \gamma(\omega) = \frac{\mathrm{Im}\varepsilon_m(\omega)}{\mathrm{Re}\frac{\partial\varepsilon_m(\omega)}{\partial\omega}}\ . \tag{1.49}$$

This expression has been given in Sect. 1.2.1 as Eq. (1.3). Importantly, the spectral width γ is a universal function of frequency ω and does not explicitly depend on the eigenmode wave function $\varphi_n(\mathbf{r})$ or system's geometry. However, the system's geometry does, of course, define the plasmon eigenfrequencies ω_n. This property has been successfully used in Ref. [180] where a method of designing nanoplasmonic systems with desired spectra has been developed. Note also that the classical SPs have been quantized in Ref. [31] in connection with the prediction of spaser, a nanoscale counterpart of laser (see Sect. 1.5).

As follows from Eq. (1.28), external frequency ω is within the range of the physical surface plasmon frequencies and, therefore, can be close to a surface plasmon resonance (pole of Green's function (1.36) as given by Eq. (1.45)) under the following conditions

$$0 \le \mathrm{Re}\, s(\omega) \le 1\ , \quad \mathrm{Im}\, s(\omega) \ll \mathrm{Re}\, s(\omega)\ . \tag{1.50}$$

These conditions are equivalent to

$$\varepsilon_d > 0\ , \quad 0 \le \mathrm{Re}\,\varepsilon_m(\omega) < 0\ , \quad \mathrm{Im}\,\varepsilon_m(\omega) \ll |\mathrm{Re}\,\varepsilon_m(\omega)|\ . \tag{1.51}$$

These conditions, in fact, constitute a definition of a plasmonic system, i.e., a system where a position of surface plasmon resonance can be physically approached: the dielectric permittivity of the metal component should be negative and almost real, while the permittivity of the second constituent (dielectric) should be positive, as assumed.

It is useful to write down an expression for Green's function (1.36) that is asymptotically valid near its poles, which can be obtained from Eqs. (1.47) and (1.48) as

$$G^r(\mathbf{r},\mathbf{r}';\omega) = \frac{1}{s'(\omega)} \sum_n \frac{\varphi_n(\mathbf{r})\,\varphi_n(\mathbf{r}')^*}{\omega - \omega_n + i\,\gamma_n}\,, \tag{1.52}$$

where γ_n is given above by Eqs. (1.48) or (1.49). This expression constitutes what is called the singular approximation or pole approximation of the Green's function. When an excitation frequency is in resonance with an SP frequency, i.e., $\omega = \omega_n$, the Green's function (1.52) increases in magnitude by $\sim\omega_n/\gamma_n \sim Q$ times, where the quality factor Q is given by Eq. (1.5).

Below, for the sake of reference, we give a modal expansion for the polarizability α of a nanoplasmonic system as a tensor,

$$\alpha_{\alpha\beta} = -\frac{\varepsilon_d}{4\pi} \sum_n \frac{1}{s_n(s - s_n)} M_{n\alpha} M^*_{n\beta}\,, \tag{1.53}$$

where the indexes α, β denote Cartesian components, and $\mathbf{M}_n$ is a coupling vector defined as

$$\mathbf{M}_n = -\int_V \Theta(\mathbf{r}) \frac{\partial \varphi_n(\mathbf{r})}{\partial \mathbf{r}}\, \mathrm{d}^3 r\,. \tag{1.54}$$

Near a SP frequency, $\omega \approx \omega_n$, a singular part of the polarizability (1.53) acquires a form

$$\alpha_{\alpha\beta} = -\frac{\varepsilon_d}{4\pi s'_n s_n} \frac{M_{n\alpha} M^*_{n\beta}}{\omega - \omega_n + i\,\gamma_n}\,. \tag{1.55}$$

Also, for the reference sake, we give a general expression for the SP radiative decay rate, $\gamma_n^{(r)}$. This can be obtained from Eq. (1.55) taking into account Eqs. (1.10) and (1.15) as

$$\gamma_n^{(r)} = \frac{\varepsilon_d^{3/2} \omega^3 \left|\mathbf{M}_n\right|^2}{9\pi c^3 s'_n s_n}\,. \tag{1.56}$$

Note that $|\mathbf{M}_n|^2 \sim V_n$, where V_n is the modal volume of the n-th eigenmode. Thus Eq. (1.56) is consistent with Eq. (1.16) obtained earlier in this chapter.

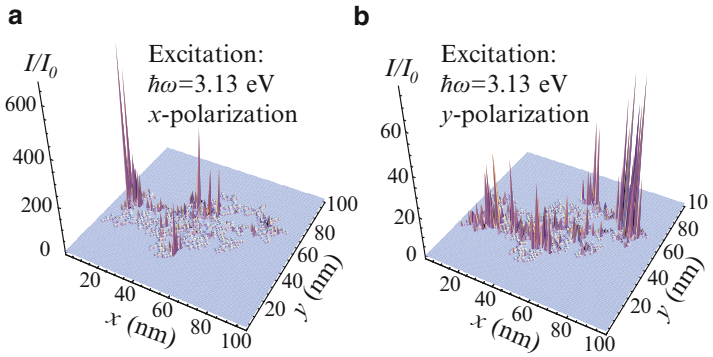

Fig. 1.8 Spatial distributions of local field intensity I relative to the external intensity I_0 for an individual CCA cluster of $N = 1{,}500$ silver nanospheres in water ($\varepsilon_d = 2.0$) for the frequency $\hbar\omega = 3.13\,\text{eV}$. The polarizations of the excitation radiation is x (**a**) and y (**b**), as indicated in the panels. The projection of the cluster nanospheres to the xy plane is also shown (Adapted from Ref. [158])

1.3.5 Examples of Local Fields and their Hot Spots

Let us give an example of local fields computed using Eq. (1.39). We start with the results of the original publications Ref. [158, 159] where the hot spots of the plasmonic local fields have been predicted. This prediction was made for fractal clusters because the fractals were expected to possess highly inhomogeneous and fluctuating local optical fields as was shown in pioneering papers in a subfield of physical optics that today is called nanoplasmonics [117, 150, 181].

In Fig. 1.8 adapted from Ref. [158], we illustrate the local-field hot spots for a silver CCA cluster of $N = 1{,}500$ identical nanospheres embedded in water. We show local field intensity $I = |\mathbf{E}(\mathbf{r}, \omega)|^2$ relative to the excitation field intensity I_0 at the surface of the silver nanospheres at a relatively high frequency $\hbar\omega = 3.13\,\text{eV}$ corresponding to vacuum wavelength $\lambda = 390\,\text{nm}$ in the far blue end of the visible spectrum. We can clearly see that the local intensity is highly non-uniform, exhibiting pronounced singular hot spots. These hot spots are localized at the minimum scale of the system (on the order of the radius of the nanospheres). The local intensity in the hot spots is greatly enhanced (by a factor of up to $\sim$600) as one would expect from an estimate $I/I_0 \sim Q^2$ – cf. Fig. 1.2.

This hot spotting is nothing else as random nanofocusing. It is similar in this respect to the formation of speckles in the wave optics, as we have discussed above in conjunction with Fig. 1.5. However, reflecting the properties of the corresponding SP eigenmodes, there is no characteristic wavelength that limits this hot spot singularity by defining the characteristic size L_s of the speckles, which is also a characteristic separation between them – see Eq. (1.31).

Another property of the local fields of a great significance is the dramatic dependence of the intensity distribution on the polarization: the local distributions or

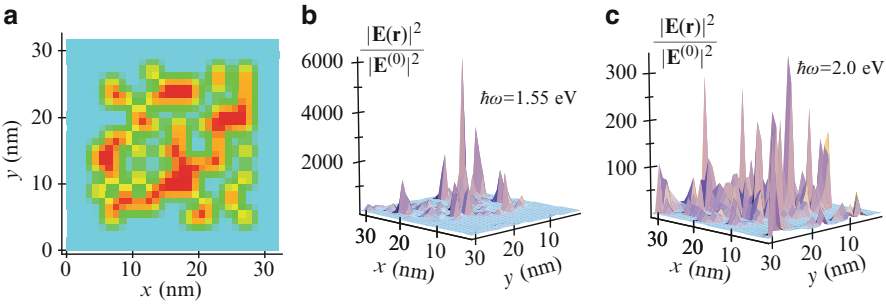

Fig. 1.9 (**a**) Geometry of nanostructured random planar composite (RPC): characteristic function $\Theta(\mathbf{r})$ is displayed in the xz plane of the RPC. Axes unit is nm; thickness of the system in the y direction (normal to its plane) is 2 nm. The fill factor is $p = 0.5$. Characteristic function $\Theta(\mathbf{r})$ is smoothed by a Gaussian filter with a radius of 1 nm to improve numerical accuracy (shown in the panel by the halftone density). (**b**) Local field intensity $|\mathbf{E}(\mathbf{r})|^2$ in the plane of the nanostructure displayed relative to the excitation field intensity $|\mathbf{E}^{(0)}|^2$; excitation frequency $\hbar\omega = 1.55\,\mathrm{eV}$; computed using Eq. (1.38). The metal is silver embedded in the dielectric with $\varepsilon_d = 2$. (**c**) Same as (**b**) but for $\hbar\omega = 2.0\,\mathrm{eV}$ (Adapted from data computed for Ref. [182])

the x-polarization (Fig. 1.5a) and y-polarization (panel b) are completely different. An experimental observation of this effect has been obtained in Ref. [118] already at a very early stage of the development of nanoplasmonics.

Note that the SP eigenmode geometry is also strongly dependent on its frequency – see Fig. 1.5. However, in externally-excited local fields, this frequency dependence is obscured by the resonance broadening due to the losses, as is evident from the expression for the resonant part of the Green's function

We will present below spectral and statistical properties of the local fields using a model of random planar composite (RPC). A specific RPC system used in the computation is shown in Fig. 1.9a. To improve numerical accuracy, we smooth the unit-step characteristic function $\Theta(\mathbf{r})$ with a Gaussian filter with a radius of 1 grid step: this dramatically improves numerical accuracy of a grid method that we use to solve the eigenproblem. Such a smoothing is clearly seen in Fig. 1.9a.

In Fig. 1.9b, c, we display the spatial distribution of the local field intensity $|\mathbf{E}(\mathbf{r})|^2$in the plane of the nanostructure at the surface of the metal. These computations are described in Ref. [182]. They are done for silver whose dielectric function is adopted from Ref. [32]; the embedding dielectric has permittivity is set as $\varepsilon_d = 2.0$. This intensity is plotted relative to the excitation field intensity $|\mathbf{E}_0|^2$; thus the quantity displayed is the enhancement factor of the local field intensity. Panel (b) shows the intensity computed from Eq. (1.38). The maximum of the local intensity enhancement of $\approx$6,000 is in a reasonable agreement with the estimate $\sim Q^2 \sim 10^4$, where Q is displayed in Fig. 1.2.

Dependence of the local fields on frequency is dramatic: cf. Fig. 1.9b, c. As frequency increases from the near-IR (1.55 eV) to visible (2.0 eV), the distribution becomes much more delocalized and its magnitude dramatically decreases, which cannot be explained by some decrease of quality factor Q alone. Most importantly,

at all frequencies these near-field intensity distributions are dominated by the pronounced hots spots. These are manifestation of the hot spots of the SP eigenmodes – see Fig. 1.7.

Generally, the intensity distribution of local field intensity in Fig. 1.9b, c is highly singular: it consists of relatively narrow peaks (hot spots [159, 164]) separated by regions of a low intensity. This is a typical distribution of intensity in plasmonic nanosystems, which is a reflection of the inhomogeneous localization of the SP eigenmodes.

1.3.6 Experimental Examples of Nanoplasmonic Hot Spots

There has been a significant number of experimental studies of near-field distributions of optical fields in plasmonic nanostructures. In all cases, a pronounced picture of the hots spots [158, 159] has been exhibited, see, e.g., Refs. [123, 156, 169]. The inhomogeneous localization of the SP eigenmodes (see Sect. 1.3.2), which is inherently related to hot spots, has recently been confirmed experimentally [162].

The photoemission electron microscope (PEEM) is a powerful tool of analyzing the distribution of the local field intensity without perturbing it in any way. In the PEEM approach, the plasmonic nanosystem to be analyzed serves as a cathode and an object of an electron microscope. The electron emission is caused by the local field $\mathbf{E}(\mathbf{r}, \omega)$ of the plasmonic system. The photoelectrons are analyzed by the electron optics of the PEEM that creates a magnified image of the system in "light" of the photo-emitted electrons.

For silver, the work function W_f (i.e., the minimum energy needed to excite an electron from the Fermi surface to the zero energy that is the energy in vacuum far away from the metal) is approximately 4.2 eV. The highest energy of an optical quantum (at the vacuum wavelength of 390 nm) is 3.2 eV, i.e., it is significantly less than W_f. Thus, a single optical photon cannot emit an electron from a silver surface. Such an emission can, however, occur through two-photon absorption, leaving for the emitted electron the kinetic energy at infinity of $E_\infty \leq 2\hbar\omega - W_f$. Such a two-photon electron photoemission is in the foundation of the so-called two-photon photoemission PEEM (or, 2PP-PEEM). On the other hand, for ultraviolet radiation (say, from a Hg lamp), the energy of a photon is sufficient for the one-photon photoemission PEEM (1PP-PEEM). The 2PP-PEEM electron intensity mirrors the distribution of $I_2 = |\mathbf{E}(\mathbf{r}, \omega)|^4$.

A model system to illustrate the hot spots used in a 2PP-PEEM experiment of Ref. [123] is shown in Fig. 1.10a. This is a diffraction grating covered with silver layer with roughness of a <10 nm RMS grain size, as the scanning electron micrograph (SEM) shows in the insert. The Hg lamp illumination (the energy of the quantum $\hbar\omega = 4.89$ eV exceeds $W_f = 4.2$ eV, thus allowing one-photon photoemission, 1PP-PEEM) shows a smooth image of the underlying diffraction grating with the resolution of the PEEM ($\lesssim$100 nm).

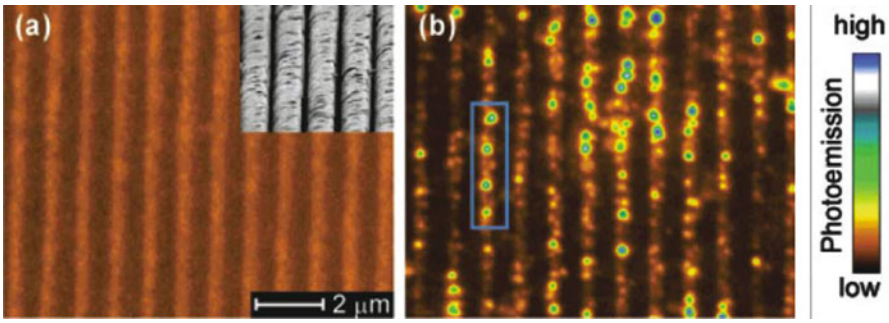

Fig. 1.10 PEEM micrographs of the same region on the silver grating obtained with (**a**) 254-nm line of a Hg lamp (1PP-PEEM) and (**b**) p-polarized 400-nm femtosecond laser excitation (2PP-PEEM). A scanning electron micrograph (SEM) of the silver grating in (**a**) is superimposed with the 1PP-PEEM image to show correspondence in the >100 nm scale topographical contrast. The surface roughness with <10 nm RMS distribution in the SEM image, which is too fine to resolve with the PEEM, gives rise to excitation of the localized SP modes seen as the hot spots in the 2PP-PEEM image of (**b**). The *blue rectangle* locates the four hot spots that were used for a coherent control experiment (Adapted from Ref. [123])

A dramatically different picture is observed in Fig. 1.10b. In this case, the irradiation is with femtosecond laser pulses of $\lambda = 400\,\text{nm}$ vacuum wavelength. The corresponding energy of the quantum is below the work function, $\hbar\omega = 3\,\text{eV} < W_f = 4.2\,\text{eV}$. Thus the electron photoemission is two-photon. The corresponding 2PP-PEEM image in Fig. 1.10b exhibits a pronounced picture of the hot spots due to the fact that in this case the optical frequency is in the plasmonic range. These hot spots are localized SPs that are excited by the p-polarized radiation with a significantly greater efficiency than by an s-polarized one. This suggests that SPPs excitation may play a role as an intermediate process for the localized SP excitation. In a full qualitative agreement with theory (see Sect. 1.3.2), these hot spots are singular, highly localized, and randomly distributed in space. The local fields in these hot spots are highly enhanced as witnessed by their dominance in the 2PP process.

Formation of the hot spots for random nanostructured plasmonic systems is a universal phenomenon whose physics is defined by the absence of the characteristic wavelength of the localized SPs, which localize at all available scales and whose fields are highly singular and highest at the minimum scale [78, 158, 159, 184].

One of the most convincing and comprehensive studies of geometry and statistics of the plasmonic hots spots is recently published Ref. [183] performed using PEEM and semicontinuous gold film whose model is RPC. Adapted from this, in Fig. 1.11, we show spatial distributions of the hot spots for a semicontinuous film with a fill factor (percentage of the area occupied by metal) $f = 0.53$. At this f, the film is close to the percolation threshold for static conductivity. The connected clusters in such a film have a fractal nature where we expect giant fluctuations and inhomogeneous localization of the SP fields [158, 159]. In fact, the distributions in Fig. 1.11 do demonstrate pronounced hot-spot behavior with inhomogeneous

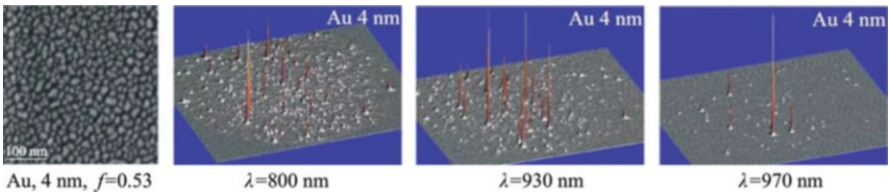

Fig. 1.11 *Left column*, scanning electron microscope images of the gold/glass films for the 4 nm grain size (filling factor $f = 0.53$). *Right*, PEEM distributions corresponding to gold/glass films for three different wavelengths. For each PEEM image, excitation wavelength λ is indicated (Adapted from Ref. [183])

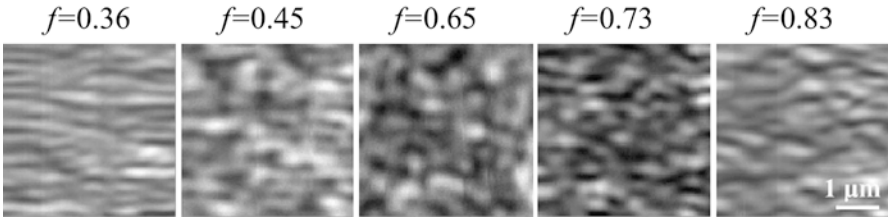

Fig. 1.12 NSOM images of $4 \times 4\,\mu m^2$ semi-continuous silver films with different metal filling fractions f as indicated above the graphs. Local intensity distribution is displayed as a function of the spatial coordinates in the plane of the film. The *white areas* correspond to higher intensities (Adapted from Ref. [169])

localization, giant fluctuations in space, where the distributions and intensities of individual hot spots strongly and randomly change with frequency. These distributions are in a full qualitative agreement with the theoretical predictions for the hot spots of local nanoplasmonic fields [158, 159] – cf. above Figs. 1.8 and 1.9.

We emphasize again that the PEEM-based observation of the plasmonic hot spots is completely non-perturbing. The photo-emitted electrons that are used in the PEEM fly away from the metal surface naturally, no matter whether they are used for imaging or not.

There has also been a series of research dealing with the observation of the plasmonic hot spots using the scanning near-field optical microscope (NSOM or SNOM) [156, 163, 169]. In fact, the first experimental evidence of the nanoplasmonic hot spots has been obtained [163] using an aperture-type NSOM, which is a based on a tapered optical fiber with the tip covered by a metal. A general concern about such observation is that they are perturbative: the tip of NSOM (or nanoscope, as it is often called) is typically much larger than a hot spot. Made of metal, it can, in principle, modify the host spot by both shifting its resonant frequency and decreasing the quality factor.

As an example, we present Fig. 1.12 adapted from Ref. [169]. This study is done on the semicontinuous metal film (random planar composite, or RPC). At relatively low values of the fill factor, $f = 0.36$ and $f = 0.45$, the local intensity distribution $I(\mathbf{r})$ shows relatively delocalized regions elongated normally to the direction of

propagation (vertical axis in the figure). These are analogous to the caustics of the usual 3d optics. Relatively close to the percolation point, $f = 0.66$ and $f = 0.73$, the distribution $I(\mathbf{r})$ becomes highly localized exhibiting singular hot spots. The behavior of $I(\mathbf{r})$ at a relatively high fill factor of $f = 0.83$ again reminds that for the low f showing delocalized caustics but not singular hot spots. This is understandable because in this case the system is basically a smooth film with a few defects. This film supports SPPs that are weakly scattered by the relatively few defects.

As we have discussed above in this section, NSOM measurements of hot spots are inherently perturbative. While PEEM is nonperturbative, the spatial resolution so far has been insufficient (due to aberrations in the electron optics and large spread of the emitted electrons over their energies). Additionally, PEEM requires clean surfaces in high vacuum.

A fundamentally different non-perturbing approach to studying nanoplasmonic hot spots has been pioneered in Refs. [185, 186]. It is based on the so-called photon-localization super-resolution far-field microscopy. This method of far-field super-resolution has originally been developed in application to biological imaging [187].

This method's fundamentals can be very briefly described as the following. Assume that there is a *single* radiating chromophore (say, fluorescing molecule) in the view field of an optical microscope. Alternatively, there may be a number of such chromophores but their concentration should be low enough so they are resolved separately by the microscope (i.e., the distance between these molecules are greater than the microscope's resolution). The center of the emission of such a single (or separately resolved) emitter can be found with any precision that is only limited by statistical fluctuations of the number of the recorded photons but not by the resolution of the microscope provided that this microscope or the system under study do not change in the course of the observation.

After the position and brightness of a given single molecule are recorded, this molecule is naturally bleached. Then another molecule comes into the hot spot and its position and brightness are recorded until it is bleached. The process is repeated until the distribution of the brightness of emitters is built with a sufficient statistical precision.

It is assumed that the emission brightness of a single chromophore is proportional to the local field intensity of the hot spot at its position and that this chromophore exerts a negligibly weak perturbation on the local field of the hot spot. Thus this photon-localization nanoscopy is a non-perturbative method allowing one to find the intensity distribution at the hot spot on the nanoscale limited only by the statistical fluctuations (inversely proportional to the accumulation time) and the size of the chromophore itself, which is negligible in realistic situations.

The results of the hot spot local intensity-distribution measurements for an aluminum surface are shown in Fig. 1.13a. This distribution is a narrow peak with

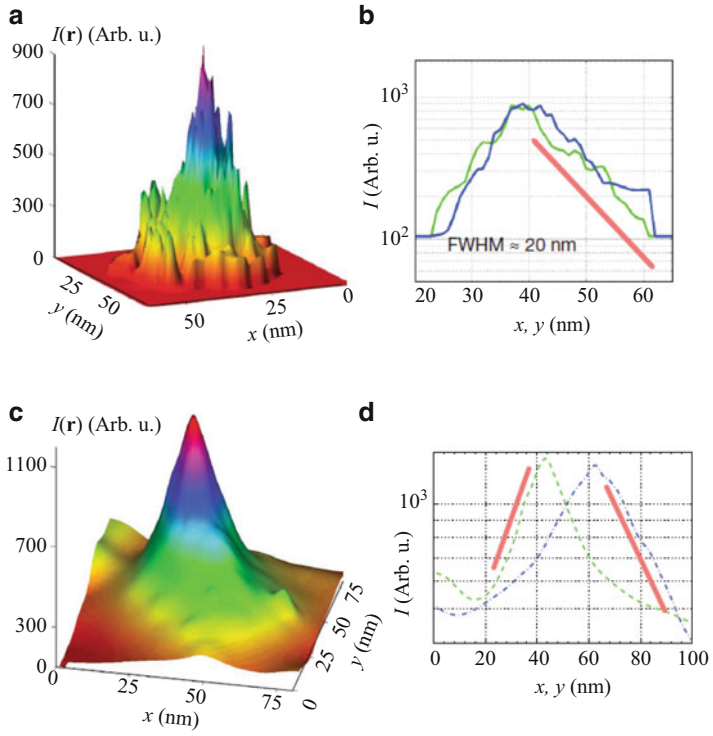

Fig. 1.13 Hot spots at the surfaces of metals measured by the photon localization method (see the text). (**a**) and (**b**) Distribution of the local intensity for a hot spot at the surface of aluminum. The kernel window size is 2.1 nm; this small window size makes the image appear noisy. The dye is Chromeo-542 with excitation at 532 nm and the emission centered around 580 nm. (**b**) An exponential decay field profile is visible, and is more evident on a log scale, shown as almost a decade of straight line (*red solid line*). The *blue* and *green curves* are two cross sections of the hot spot along x and y directions through the peak. The FWHM of the spot is ∼20 nm. (**c**) and (**d**) is the same as (**a**) and (**b**), respectively, but for the case of a silver metal colloid cluster precipitated on a surface. A Chromeo-642 dye (Active Motif) – whose emission centers around 660 nm – is used (Adapted from Ref. [185])

the width of ≈20 nm. The observed fine structure of this distribution is attributed to statistical fluctuations [185]. The cross section through this distribution displayed in Fig. 1.13b suggests an exponential decay of this distribution function in space with the FWHM = 20 nm.

Very similar results are obtained for the silver colloid clusters as shown in Fig. 1.13c, d. Note that the aluminum surface studied is nominally smooth and contains only random roughness while the silver colloid clusters are fractals whose density fundamentally possesses large and correlated fluctuations.

1.4 Ultrafast Plasmonics and Coherent Control on Nanoscale

1.4.1 Introduction

The nanoplasmonic processes can potentially be the fastest in optics: their shortest evolution times are defined by the inverse spectral width of the region of the plasmonic resonances and are on the order of 100 as [188], see also Sect. 1.2.1. The relaxation times of the SP excitations are also ultrashort, in the 10–100 fs range [189–193]. See also the SP relaxation times for gold and silver displayed in Fig. 1.3. The nanolocalization and such an ultrafast kinetics make plasmonic nanostructures promising for various applications, especially for the ultrafast computations, data control and storage on the nanoscale.

These and potentially many other applications require precise control over the optical excitations of the nanostructures in time and space on the femtosecond-nanometer scale. Such a control cannot be imposed by far-field focusing of the optical radiation because the diffraction limits its dimension to greater than half wavelength. In other words, the optical radiation does not have spatial degrees of freedom on the nanoscale. There is a different class of approaches to control a system on nanoscale based on plasmonic nanoparticles or waveguides brought to the *near-field* region of the system. Among these we mention: the tips of scanning near-field optical microscopes [194], adiabatic plasmonic waveguides [12], nanowires [195, 196], plasmonic superlenses [197] or hyperlenses [198]. In all these cases, massive amount of metal is brought to the vicinity of the plasmonic nanosystem, which will produce strong perturbations of its spectrum and SP eigenmodes, cause additional optical losses, and adversely affect the ultrafast dynamics and energy nanolocalization in the system. This nanowaveguide approach also may not work because of the excitation delocalization due to the strong interaction (capacitive coupling) at the nanoscale distances for optical frequencies.

We have proposed [199] a principally different approach to ultrafast optical control on the nanoscale based on the general idea of coherent control. The coherent control of the quantum state of atom and molecules is based on the directed interference of the different quantum pathways of the optical excitation [200–209], which is carried out by properly defining the phases of the corresponding excitation waves. This coherent control can also be imposed by an appropriate phase modulation of the excitation ultrashort (femtosecond) pulse [206,210–212]. Shaping the polarization of a femtosecond pulse has proven to be a useful tool in controlling quantum systems [213].

Our idea of the coherent control on the nanoscale by the phase modulation of the excitation pulse can be explained with a schematic shown in Fig. 1.14. Phase modulation of the excitation pulse can be thought of as changing the frequency (color) light as the pulse progresses in time. For the sake of argument, let us assume that, as shown in Fig. 1.14, that initially the pulse contains blue colors that gradually change to red with the time progression. At earlier times, the dominating blue component of the pulse will excite the SP eigenmodes with corresponding high

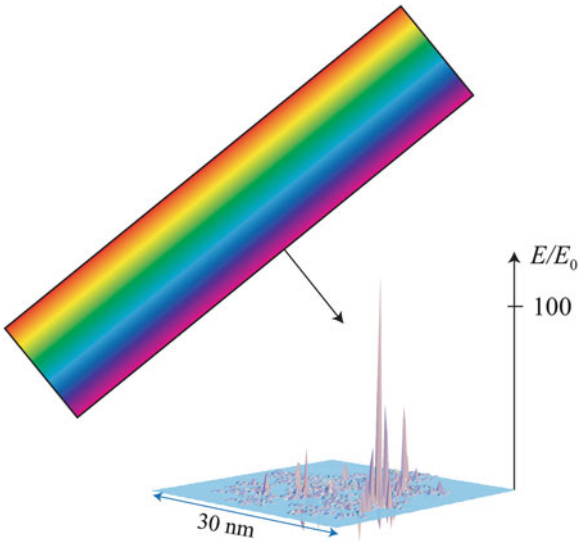

Fig. 1.14 Schematic of the fundamentals of the coherent control of nanoscale optical energy distribution. An excitation pulse is phase-modulated (shown by different colors changing with the progression of the pulse), which may be qualitatively thought of as different frequencies (colors) are incident on the nanosystem at different times, in a certain sequence. The system (a fractal cluster) is indicated by its projection on the horizontal coordinate plane. In response to this pulse, different SP eigenmodes are excited in a sequence. As time progresses, these eigenmodes interfere between themselves leading to a hot spot appearing at a required position at a given time. This leads to a large enhancement of the local field E relative to the excitation field E_0

optical frequencies. As the pulse progresses, the lower-frequency eigenmodes are excited. It is assumed that the total duration τ_p of the pulse is less than the decay (decoherence) time $\tau = \gamma^{-1}$ of the SPs, i.e., $\tau_p \lesssim \tau$ (for the decay rates and life times of the SPs see Eq. (1.3) or (1.49) and Fig. 1.3). In such a case, the SPs of different frequencies will coexist simultaneously, and their fields will interfere. This interference depends on the relative phases and amplitudes of the SPs of different frequencies that, in turn, are determined by the relative phases of different spectral components of the excitation pulse. The ultimate goal of the spatio-temporal coherent control on the nanoscale is to have a hot spot of the local fields at a given nanosite at a given femtosecond temporal interval. Below in this chapter we show that this problem is solved both theoretically and experimentally.

Another approach that we have proposed [214] invokes spatial modulation of the excitation field on the microscale in a polaritonic system. This field excites SPPs whose phases are determined by those of the original field. This determines the wave fronts of the SPP waves that focus on the nanoscale at the targeted nanofoci at the required times with femtosecond temporal resolution. The spatial-phase coherent control of the SPPs has been demonstrated experimentally by different groups [215, 216].

Our initial idea [199] has been subsequently developed theoretically [149, 213, 217, 218] and experimentally [123, 219–221]. In this coherent control approach, one sends from the far-field zone a shaped pulse (generally, modulated by phase, amplitude, and polarization) that excites a wide-band packet of SP excitations in the entire nanosystem. The phases, amplitudes, and polarizations of these modes are forced by this shaped excitation pulse in such a manner that at the required moment of time and at the targeted nanosite, these modes' oscillations add in phase while at the other sites and different moments of time they interfere destructively, which brings about the desired spatio-temporal localization.

Theoretically, the number of the effective degrees of freedom that a shaped femtosecond pulse may apply to a nanoplasmonic system can be estimated in the following way. The number of the independent frequency bands is $\sim \Delta\omega/\gamma$, where $\Delta\omega$ is the bandwidth of the plasmonic system. For each such a band, there are two degrees of freedom: amplitude and phase. Thus, the total number N_{DF} of the degrees of freedom for coherent control can be estimated as

$$N_{DF} \sim 2\frac{\Delta\omega}{\gamma} . \tag{1.57}$$

For a plasmonic system with the maximum bandwidth $\Delta\omega \sim \omega$, and Eq. (1.57) becomes

$$N_{DF} \sim 4Q , \tag{1.58}$$

where we took into account Eq. (1.5). In the optical region for noble metals $Q \sim 100$ (see Fig. 1.2), providing a rich, $\sim$100-dimensional space of controlling parameters. The coherent control approach is non-invasive: in principle, it does not perturb or change the nanosystem's material structure in any way.

However, how to actually determine a shaped femtosecond pulse that compels the optical fields in the nanosystem to localize at a targeted nanosite at the required femtosecond time interval is a formidable problem to which until now there has been no general and effective approach. To compare, our original chirped pulses possessed only two effective degrees of freedom (carrier frequency ω_0 and chirp) which allowed one to concentrate optical energy at the tip of a V-shape structure vs. its opening [149, 199]. Similarly, the two unmodulated pulses with the regulated delay τ between them used in the interferometric coherent control [123, 217, 220] also possess only two degrees of freedom (τ and ω_0) and can only select one of any two local-field hot spots against the other; it is impossible, in particular, to select one desired hot spot against *several* others.

There exists another method based on the adaptive genetic algorithms [206]. However, its application to the spatial-temporal localization in nanosystem is difficult due to the complexity of the problem. To date, the only example is the spatial concentration of the excitation on one arm of the three-pronged metal nanostar [219] where the obtained controlling pulses are very complicated and difficult to interpret though the nanosystem itself is rather simple. A general problem

with this method is that the adaptive genetic algorithms are actually refined trial-and-error methods; they do not allow one to obtain the required controlling pulses as a result of the solution of a set of deterministic equations or an application of any regular deterministic procedure such as Green's function integration.

1.4.2 Time-Reversal Solution for Coherent Control

Our solution of this major problem of the coherent control, which is proposed and theoretically developed in Ref. [222], is based on an idea of time-reversal that has originally been proposed and used to control the focusing of acoustic waves and microwave radiation [223–225]. Some of these studies required use of a reverberating chamber to cause multiple interactions of the waves with the system needed to transfer the information to the far field. The electromagnetic subwavelength focusing also required a subwavelength-scale metal structure (a metal wire brush) to be positioned in the vicinity of the target system as a focusing antenna. In contrast, in nanoplasmonics there is no need for the reverberating chamber or the metal brush antenna, because the plasmonic nanosystem plays the roles of both of them. It confines the plasmonic modes for long times relative to their oscillation periods and also nano-localizes these modes.

1.4.3 Qualitative Description of Time-Reversal Coherent Control

The idea of the time-reversal solution of the nanoscale coherent control can be described using a schematic of Fig. 1.15. Consider a metal plasmonic nanosystem, indicated by blue in Fig. 1.15a, which may be embedded in a host dielectric (or be in vacuum). The nanosystem is excited by an external ultrafast (femtosecond) nanosource of radiation at its surface. As such we choose an oscillating dipole indicated by a double red arrow. This dipole generates a local optical electric field shown by a bold red waveform. This field excites SP oscillations of the system in its vicinity. In turn these oscillations excite other, more distant regions, and so forth until the excitation spreads out over the entire system. The relatively long relaxation time of these SP modes leads to the long "reverberations" of the plasmonic fields and the corresponding far-zone optical electric field. The latter is shown in Fig. 1.15b where one can see that a complicated vector waveform is predicted. This waveform is time reversed, as shown in panel (c), and send back to the system as an excitation plane wave from the *far-field* zone. If the entire field, in the whole space including the near-field (evanescent) zone, were time reversed and the system would have been completely time-reversible, which would imply the absence of any dielectric losses, then the system would have been compelled by this field exactly to back-trace its

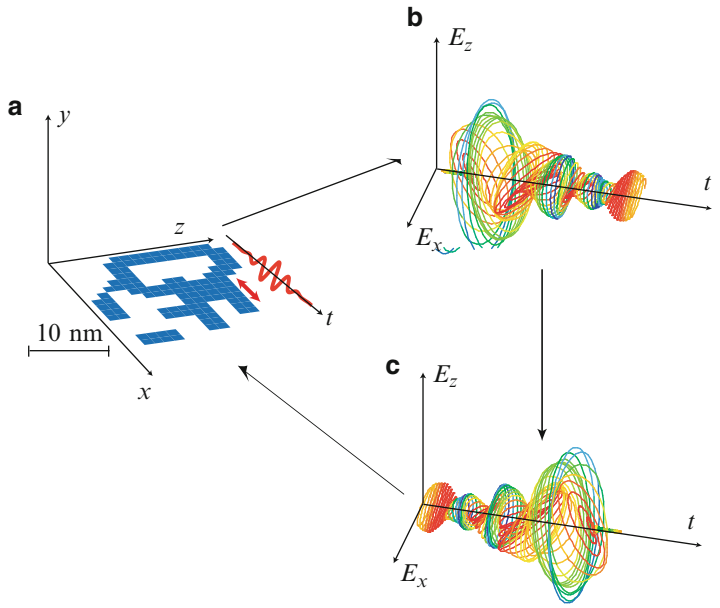

Fig. 1.15 (**a**) Geometry of nanosystem, initial seed oscillating dipole and its oscillation waveform. The nanosystem as a thin nanostructured silver film is depicted in *blue*. A position of the oscillating dipole that initially excites the system is indicated by a *double red arrow*, and its oscillation in time is shown by a *bold red waveform*. (**b**) Field in the far-field zone that is generated by the system following the excitation by the local oscillating dipole: vector $\{E_x(t), E_z(t)\}$ is shown as a function of the observation time t. The color corresponds to the instantaneous ellipticity as explained in the text. (**c**) Same as in panel (**b**) but for a time-reversed pulse in the far zone that is used as an excitation pulse to drive the optical energy nanolocalization at the position of the initial dipole

own evolution in time. This would have lead to the concentration of the local optical energy exactly at the position of the initial dipole at a time corresponding to the end of the excitation pulse.

Indeed, the system is somewhat lossy, which means that it is not exactly time reversible. Nevertheless, these losses are small, and one may expect that they will not fundamentally change the behavior of the system. Another problem appear to be more significant: the evanescent fields contain the main information of the nano-distribution of the local fields in the system, and they cannot be time reversed from the far zone because they are exponentially small, practically lost there. However, our idea is that the nanostructured metal system itself plays the role of the metal brush of Ref. [225] continuously coupling the evanescent fields to the far zone. Therefore the fields in the far zone actually contain, in their reverberations, most information about the evanescent fields that will be regenerated in the process of the time reversal.

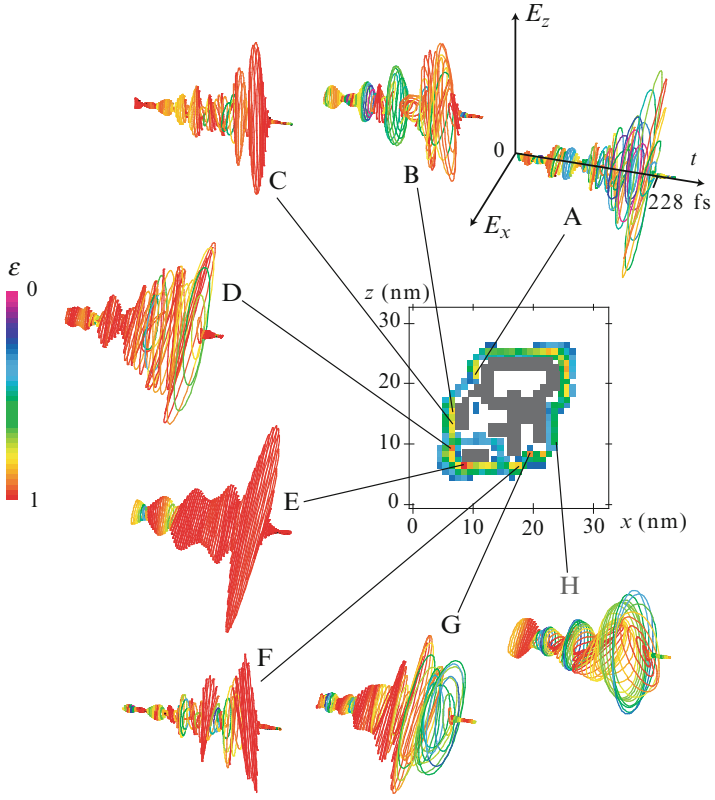

Fig. 1.16 Schematic of plasmonic-nanosystem geometry, local fields, and pulses generated in the far field. *Central insert*: The geometry of a nanosystem is shown by *dark gray*, and the local fields in the region surrounding it are shown by colors. The highest local field intensity is depicted by *red* and the lowest intensity is indicated by *blue* (in the rainbow sequence of colors). Panels *A*–*H*: The excitation waveforms in the far fields obtained as described in the text by positioning the initial excitation dipole at the metal surface at the locations indicated by the corresponding lines. Coordinate vectors $\boldsymbol{\rho}$ of points A–H in the xz plane are (in nm): $\boldsymbol{\rho}_A = (11, 22)$, $\boldsymbol{\rho}_B = (7, 16)$, $\boldsymbol{\rho}_C = (7, 14)$, $\boldsymbol{\rho}_D = (7, 10)$, $\boldsymbol{\rho}_E = (9, 7)$, $\boldsymbol{\rho}_F = (18, 7)$, $\boldsymbol{\rho}_G = (20, 9)$, and $\boldsymbol{\rho}_H = (24, 11)$. The instantaneous degree of linear polarization ε is calculated as the eccentricity of an instantaneous ellipse found from an fit to a curve formed by vector $\{E_x(t), E_y(t)\}$ during an instantaneous optical period. The pure circular polarization corresponds to $\varepsilon = 0$ and is denoted by *blue-violet color*; the pure linear polarization is for $\varepsilon = 1$ indicated by *red*. The corresponding polarization color-coding bar is shown at the left edge of the figure

We will illustrate this idea by considering a random planar composite (RPC) whose geometry is shown in gray in the center of Fig. 1.16. In specific computations, as the plasmonic metal, we consider silver whose dielectric permittivity ε_m we adopt from bulk data [32]. This system has been generated by randomly positioning $2 \times 2 \times 2\,\text{nm}^3$ metal cubes on a plane, which for certainty we will consider as the xz coordinate plane. The random system shown in the center of Fig. 1.16 has filling factor of $f = 0.5$.

The interaction of a nanosystem with electromagnetic pulses is described in Green's function approach using quasistatic approximation [149, 199, 226] – see Sect. 1.3.3. It is known that the optical excitation energy in random plasmonic nanostructures localizes in "hot spots" whose size is on the nanoscale and is determined by the minimum scale of the system inhomogeneities [78, 159, 160, 227] – see Sect. 1.3.5.

Initially, to find positions of these hot spots in our system, we apply an ultrashort near-infrared (near-ir) pulse whose spectral width was very large, covering a frequency band from 1.1 to 1.7 eV. The pulse polarization is along the z axis (the incidence direction is normal to the plane of the nanostructure, i.e. along the y axis). The resulting optical electric field $\mathbf{E}$ is expressed in terms of the external electric field of the excitation optical wave $\mathbf{E}_0$ and retarded dyadic Green's function $\mathbf{G}^r$, as given by Eqs. (1.43) and (1.44).

The hot spots are always localized at the surface of the metal, predominantly at the periphery of the system. Their intensities found as the result of these computations are depicted by colors in the center of Fig. 1.16. The highest local intensity is indicated by red, and the lowest by blue in the region surrounding the metal. We have selected eight of these hot spots for our computations as denoted by letters A–H in the figure.

To generate the field in the far zone, we take a point dipole and position it at a surface of the metal at point $\mathbf{r}_0$ at such a hot spot, as described in the discussion of Fig. 1.15 above. The near-zone field $\mathbf{E}^L(\mathbf{r}, t)$ generated in response to this point dipole is found from Green's function relation

$$\mathbf{E}^L(\mathbf{r}, t) = \frac{4\pi}{\varepsilon_d} \int dt' \mathbf{G}^r(\mathbf{r}, \mathbf{r}_0; t - t') \, \mathbf{d}(\mathbf{r}_0, t') \, . \tag{1.59}$$

Knowing this local electric field, we calculate the total radiating optical dipole moment of the nanosystem in the frequency domain as

$$\mathbf{D}(\omega) = \frac{1}{4\pi} \int d^3 r \, [\varepsilon_m(\omega) - \varepsilon_d] \, \Theta(\mathbf{r}) \mathbf{E}^L(\mathbf{r}, \omega) \, . \tag{1.60}$$

Here and below, the frequency- and time-domain quantities, as indicated by their arguments ω and t, are Fourier transforms of each other. The field in the far zone produced by this radiating dipole is given by standard electrodynamic formula – see, e.g. §67 in Ref. [228]. The time-reversed field is generated by time-reversed dipole $\mathbf{D}^T(t)$ that is complex-conjugated in the frequency domain, $\mathbf{D}^T(\omega) = \mathbf{D}(\omega)^*$.

The dependence on time of the initial excitation dipole, $\mathbf{d}(\mathbf{r}_0, t)$ is set as an ultrashort Gaussian-shaped pulse of 12 fs duration with the carrier frequency $\hbar\omega_0 = 1.2$ eV. Following the procedure described above, the fields shown in Figs. 1.15 and 1.16 have been calculated for the radiation propagating in the y direction (normal to the plane of the nanostructure). These fields simply copy the retarded time evolution of the emitting dipole.

At the completing stage of our calculations, the time-reversed excitation pulse is sent back to the system as a plane wave propagating along the y direction (normal to the nanosystem plane). To calculate the resulting local fields, we again use Green's function Eq. (1.43) where the shaped excitation pulse substitutes for field $\mathbf{E}_0$.

1.4.4 Numerical Results for Time-Reversal Coherent Control

The electric field of the excitation wave is chosen as a modulated waveform (including amplitude, phase, and polarization modulation) that has been computed as described above in the previous subsection. The optical excitation energy can only be concentrated at sites where SP eigenmodes localize. For the present system, these are the hot spots shown by color in the central insert of Fig. 1.16, labeled A–H. The corresponding calculated excitation waveforms are displayed in panels as vector plots shown as functions of time $\{E_x(t), E_z(t)\}$.

There are several important features of these waveforms deserving our attention and discussion. First, these waveforms are rather long in duration: much longer than the excitation-dipole 12 fs pulses. This confirms our understanding that the initial dipole field excites local SP fields that, in a cascade manner, excite a sequence of the system SPs, which ring down relatively long time (over 200 fs, as shown in the figure). This long ring-down process is exactly what is required for the nanostructure to transfer to the far-field zone the information on the near-zone local (evanescent) fields as is suggested by our idea presented above in the introduction. The obtained fields are by shape resembling the controlling pulses for the microwave radiation [225]. However, a fundamental difference is that in the microwave case the long ringing-down is due to the external reverberation chamber, while for the nanoplasmonic systems it is due to the intrinsic evolution of the highly resonant SP eigenmodes that possess high Q-factors (setting a reverberation chamber around a nanosystem would have been, indeed, unrealistic).

Second, one can see that the pulses in Fig. 1.16 have a very nontrivial polarization properties ranging from the pure linear polarization (indicated by red as explained in the caption to Fig. 1.16) to the circular polarization indicated by blue, including all intermediate degrees of circularity. The temporal-polarization structure of pulses A–H in Fig. 1.16 is very complicated, somewhat reminding that of Ref. [219], which was obtained by a genetic adaptive algorithm. However, in our case these pulses are obtained in a straightforward manner, by applying the well-known, deterministic Green's function of the system, which is a highly efficient and fast method.

Third, and most important, feature of the waveforms in Fig. 1.16 is that they are highly site-specific: pulses generated by the initial dipole in different positions are completely different. This is a very strong indication that they do transfer to the far-field zone the information about the complicated spatio-temporal structure of the local, near-zone fields. This creates a pre-requisite for studying a possibility to use these pulses for the coherently-controlled nano-targeting.

Now we turn to the crucial test of the nanofocusing induced by the excitation pulses discussed above in conjunction with Fig. 1.16. Because of the finite time window ($T = 228$ fs) used for the time reversal, all these excitation pulses end and should cause the concentration of the optical energy (at the corresponding sites) at the same time, $t = T = 228$ fs (counted from the moment the excitation pulse starts impinging on the system). After this concentration instant, the nanofocused fields can, in principle, disappear (dephase) during a very short period on the order of the initial dipole pulse length, i.e. $\sim$12 fs. Thus this nanofocusing is a dynamic, transient phenomenon.

Note that averaging (or, integration) of the local-field intensity $I(\mathbf{r},t) = |\mathbf{E}(\mathbf{r},t)|^2$ over time t would lead to the loss of the effects of the phase modulation. This is due to a mathematical equality $\int_{-\infty}^{\infty} I(\mathbf{r},t)dt = \int_{-\infty}^{\infty} |\mathbf{E}(\mathbf{r},\omega)|^2 d\omega/(2\pi)$, where the spectral-phase modulation of the field certainly eliminates from the expression in the right-hand side. Thus the averaged intensity of the local fields is determined only by the local power spectrum of the excitation $|\mathbf{E}(\mathbf{r},\omega)|^2$ and, consequently, is not coherently controllable. Very importantly, such a cancellation does not take place for nonlinear phenomena. In particular, two-photon processes such as two-photon fluorescence or two-photon electron emission that can be considered as proportional to the squared intensity $I^2(\mathbf{r},t) = |\mathbf{E}(\mathbf{r},t)|^4$ are coherently controllable even after time averaging (integration), as we have argued earlier [149, 217]. Note the distributions measured in nonlinear optical experiments with the detection by the PEEM [123, 219, 220, 229] and in the fluorescence upconversion experiments [230] can be modeled as such nonlinear processes that yield distributions $\langle I^n(\mathbf{r})\rangle = \int_{-\infty}^{\infty} I^n(\mathbf{r},t)dt/T$, where $n \geq 2$. Inspired by this, we will consider below, in particular, the coherent control of the two-photon process averaged intensity $\langle I^2(\mathbf{r})\rangle$.

Let us investigate how precisely one can achieve the spatio-temporal focusing of the optical excitation at a given nanosite of a plasmonic nanostructure using the full shaping (amplitude, phase, and polarization) of the excitation pulses found from the time-reversal method. The results for the present nanostructure, targeting sites A–H, are shown in Fig. 1.17. For each excitation pulse, the spatial distribution of the local field intensity is displayed for the moment of time when this local intensity acquires its global (highest) maximum. The most important conclusion that one can draw from comparing panels (a)–(h) is that for each pulse A–H this global maximum corresponds to the maximum concentration of the optical energy at the corresponding targeted nanosite A–H. This obtained spatial resolution is as good as 4 nm, which is determined by the spatial size of inhomogeneities of the underlying plasmonic metal nanosystem. It is very important that this localization occurs not only at the desired nanometer-scale location but also very close to the targeted time that in our case is $t = 228$ fs. Thus the full shaping of femtosecond pulses by the time reversal is an efficient method of controlling the spatio-temporal localization of energy at the femtosecond-nanometer scale.

Let us turn to the temporal dynamics of intensity of the nanoscale local fields at the targeted sites A–H, which is shown in Fig. 1.18a–h. As we can see, in each of the panels there is a sharp spike of the local fields very close to the target time of

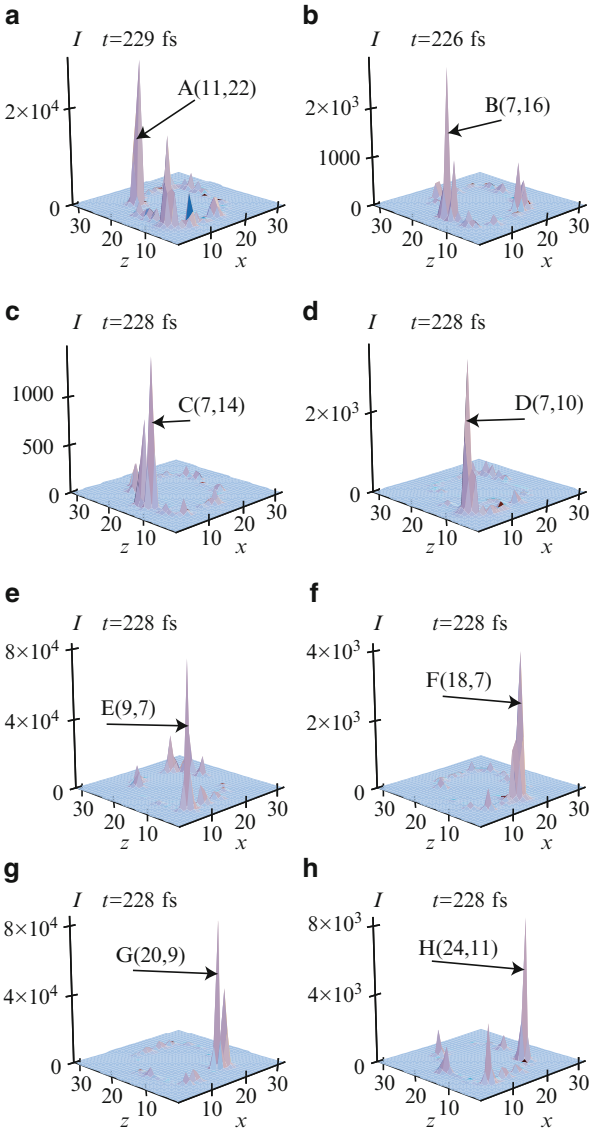

Fig. 1.17 Spatial distributions of the local optical field intensities at the surface of the metal nanostructure. Panels (**a**)–(**h**) correspond to the excitation with pulses A–H. Each such a distribution is displayed for the instance t at which the intensity for a given panel reaches its global maximum in space and time. This time t is displayed at the top of the corresponding panels. The corresponding targeted sites are indicated by *arrows* and labeled by the corresponding letters A–H and the coordinates (x, z). No special normalization has been applied so the distribution within any given panel is informative but not necessarily the magnitudes of the intensities between the panels

$t = 228$. The duration of this spike in most panels (a–f) is close to that of the initial dipole, i.e., 12 fs. This shows a trend to the reproduction of the initial excitation state due to the evolution of the time-reversed SP packet induced by the shaped pulses. There is also a pedestal that shows that this reproduction is not precise, which is expected due to the fact that the time reversal is incomplete: only the far-zone field propagating in one direction (along the y axis) is reversed. Nevertheless, as the discussion of Fig. 1.17 shows, this initial excitation-state reproduction is sufficient

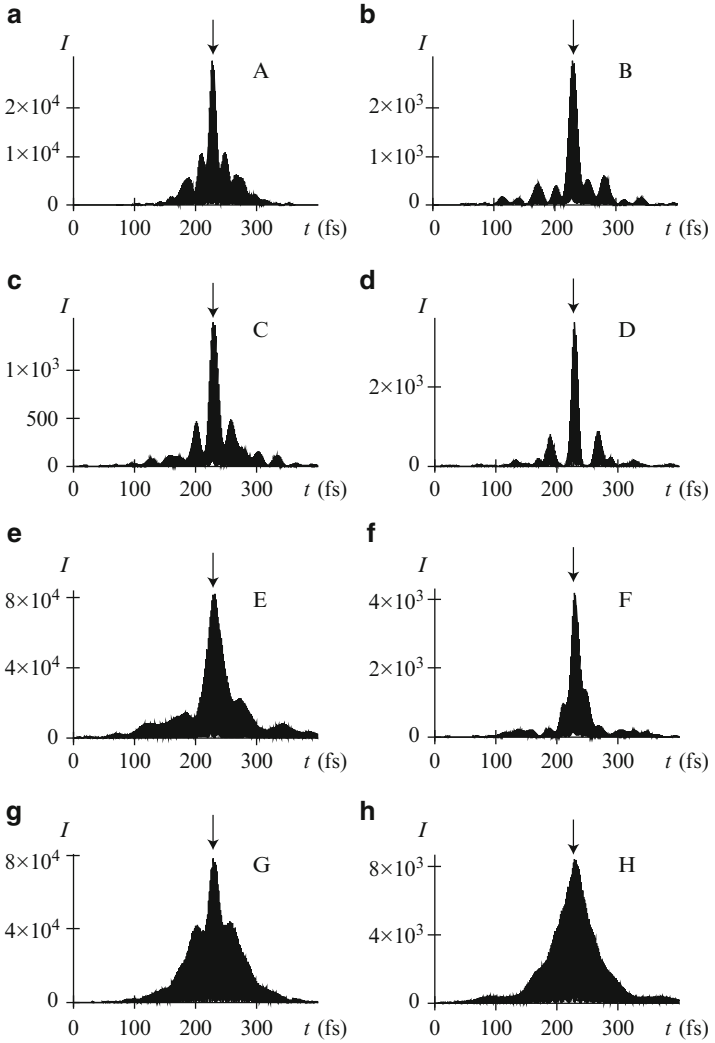

Fig. 1.18 (**a**)–(**h**) Temporal dynamics of the local field Intensity $I(\mathbf{r},t) = \mathbf{E}^2(\mathbf{r},t)$ at the corresponding hot spots A–H. The *down-arrows mark* the target time $t = 228$ fs where the local energy concentration is expected to occur

to guarantee that the targeted (initial excitation) site develops the global maximum (in time and space) of the local-field intensity. Interesting enough, the trend to reproduce the initial excitation state is also witnessed by almost symmetric (with respect to the maximum points $t = 228$ fs) shapes of all waveforms, which occurs in spite of the very asymmetric shapes of the excitation waveforms (cf. Fig. 1.16).

Apart from the ultrafast (femtosecond) dynamics of the nanolocalized optical fields discussed above in conjunction with Figs. 1.17 and 1.18, there

is a considerable interest in its the time-integrated or averaged distributions, in particular, the mean squared intensity $\langle I^2(\mathbf{r})\rangle$. This quantity defines the nanoscale spatial distribution of the incoherent two-photon processes such as two-photon electron emission or two-photon luminescence. For example, in some approximation, the spatial distribution of the two-photon electron emission recorded by PEEM [123, 219, 220, 229] is determined by $\langle I^2(\mathbf{r})\rangle$.

Now we test the spatial concentration of time-averaged mean-squared intensity $\langle I^2(\mathbf{r})\rangle$ for all sites, which is displayed in Fig. 1.19. As clearly follows from this figure, in all cases, there are leading peaks at the targeted sites. Thus the two-photon excitation, even after the time averaging, can be concentrated at desired sites using the coherent-control by the time-reversed shaped pulses.

We point out that there has recently been an experimental demonstration of a coherent spatiotemporal control on the nanoscale by polarization and phase pulse shaping [221]. The optical energy concentration at a given site on a ∼50 nm spatial scale at a given time on a ∼100 fs temporal scale has been demonstrated. Since this time scale is comparable to or longer than the SP dephasing time, the time-reversal method could not be employed.

1.4.5 Coherent Control by Spatiotemporal Pulse Shaping

For coherent control on the nanoscale, as we have described above in Sect. 1.4, the phase of the excitation waveform along with its polarization provide functional degrees of freedom to control the nanoscale distribution of energy [123, 149, 199, 217–219, 221, 229, 231]. Spatiotemporal pulse shaping permits one to generate dynamically predefined waveforms modulated both in frequency and in space to focus ultrafast pulses in the required microscopic spatial and femtosecond temporal domains [232, 233].

Here we follow Ref. [214] that has introduced a method of full coherent control on the nanoscale where a temporally and *spatially* modulated waveform is launched in a graded nanostructured system, specifically a wedge – see schematic of Fig. 1.20. Its propagation from the thick (macroscopic) to the thin (nanoscopic) edge of the wedge and the concurrent adiabatic concentration provide a possibility to focus the optical energy in nanoscale spatial and femtosecond temporal regions.

This method unifies three components that individually have been developed and experimentally tested. The coupling of the external radiation to the surface plasmon polaritons (SPPs) propagating along the wedge occurs through an array of nanoobjects (nanoparticles or nanoholes) that is situated at the thick edge of the wedge. The phases of the SPPs emitted (scattered) by individual nanoobjects are determined by a spatio-temporal modulator. The nanofocusing of the SPPs occurs due to their propagation toward the nanofocus and the concurrent adiabatic concentration [12, 234, 235].

The coupling of the external radiation to SPPs and their nanofocusing have been observed – see, e.g., Refs. [236, 237]. The second component of our approach,

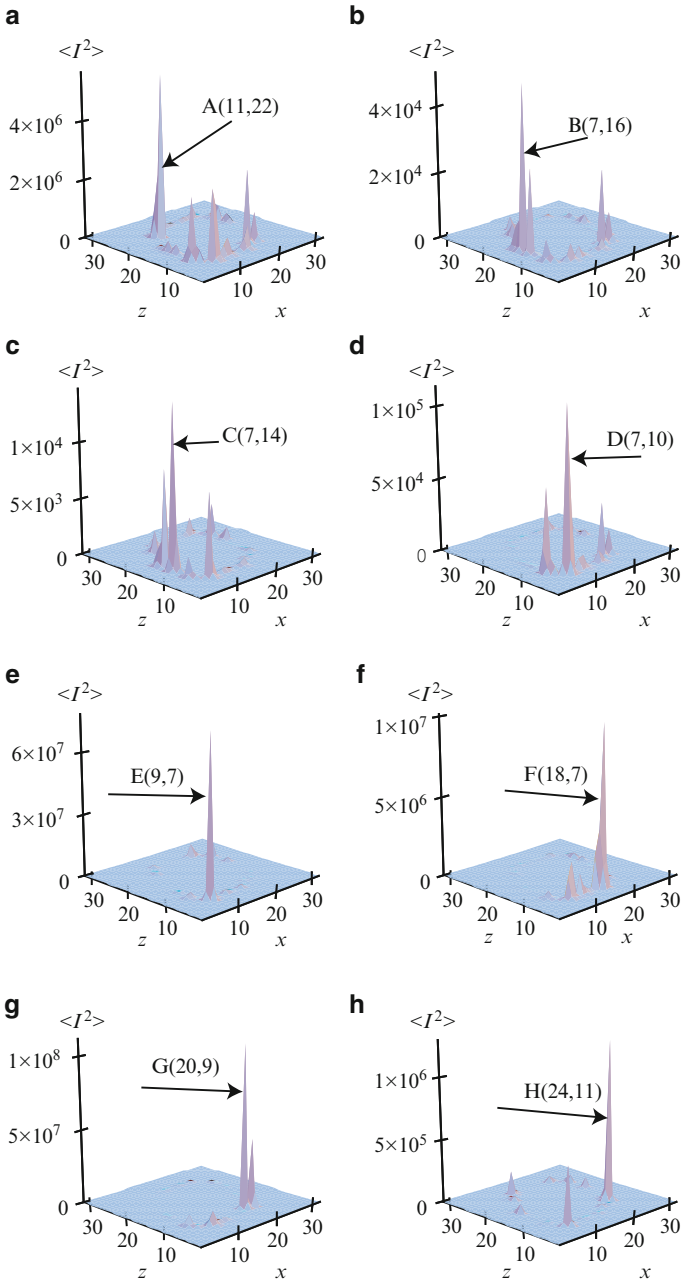

Fig. 1.19 Spatial distributions of the time-averaged mean-squared intensity $\langle I^2(\mathbf{r})\rangle$. This represents, in particular, the spatial distribution of the two-photon excited photocurrent density. Panels (**a**)–(**h**) correspond to the excitation with pulses A–H. The corresponding targeted sites are indicated by *arrows* and labeled by the corresponding letters A–H and coordinates (x, z). No special normalization has been applied so the distribution within any given panel is informative on spatial distribution but not necessarily the magnitudes of the intensities between the panels

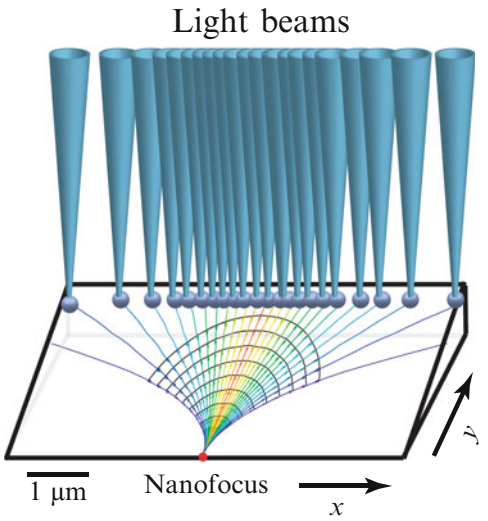

Fig. 1.20 Schematic of spatiotemporal coherent control on nanoscale (Adapted from Ref. [214]). Independently controlled light beams (shown by *blue cones*) are focused on launch pads depicted as silver spheres that are positioned on a thick edge of a wedge. SPP wavelets generated by the launchpads are shown by *black arcs*. Normal to them are rays (SPP trajectories) that are displayed by color lines coded accordingly to their origination points. These wavefronts and trajectories converge at the nanofocus indicated by the *red dot*

the spatio-temporal coherent control of such nanofocusing has been developed [232, 233]. The third component, the adiabatic concentration of SPPs also has been observed and extensively studied experimentally [13–16, 18, 19, 22].

The adiabatic concentration (nanofocusing) is based on adiabatic following by a propagating SPP wave of a graded plasmonic waveguide, where the phase and group velocities decrease while the propagating SPP wave is adiabatically transformed into a standing, localized SP mode. A new quality that is present in this approach is a possibility to arbitrary move the nanofocus along the nanoedge of the wedge. Moreover, it is possible to superimpose any number of such nanofoci simultaneously and, consequently, create any distribution of the nanolocalized fields at the thin edge of the wedge.

To illustrate this idea of the full spatiotemporal coherent control, now let us turn to a wedge that contains a line of nanosize scatterers (say, nanoparticles or nanoholes) located at the thick edge and parallel to it, i.e. in the x direction in Fig. 1.20. Consider first monochromatic light incident on these nanoparticles or nanoholes that scatter and couple it into SPP wavelets. Every such a scatterer emits SPPs in all directions; there is, of course, no favored directionality of the scattering.

At this point, we assume that the excitation radiation and, correspondingly, the scattered wavelets of the SPP are coherent, and their phases smoothly vary in space along the thick edge, i.e., in the x direction. Then the SPP wavelets emitted by different scatterers will interfere, which in accord with the Huygens-Fresnel

principle leads to formation of a smooth wavefront of the SPP wave at some distance from the scatterers in the "far SPP field", i.e., at distances much greater than the SPP wavelength $2\pi/k_{SPP}$.

Such wavefronts are shown in Fig. 1.20 with concave black curves. The energy of the SPP is transferred along the rays, which are the lines normal to the wavefronts, shown by the colored lines. By the appropriate spatial phase modulation of the excitation radiation along the line of scatterers (in the x direction) over distances of many SPP wavelengths, these wavefronts can be formed in such a way that the rays intersect at a given point, forming a nanofocus at the thin (sharp) edge of the wedge, as shown schematically in Fig. 1.20. Diffraction of the SPP waves will lead to a finite size of this focal spot.

By changing the spatial phase profile of the excitation radiation, this focal spot can be arbitrarily moved along the thin edge. This focusing and adiabatic concentration, as the SPPs slow down approaching the sharp edge, will lead to the enhancement of the intensity of the optical fields in the focal region. This dynamically-controlled concentration of energy is a plasmonic counterpart of a large phased antenna array (also known as an aperture synthesis antenna), widely used in radar technology (synthetic aperture radar or SAR) and radio astronomy [238].

Now we can consider excitation by spatiotemporally shaped ultrashort pulses independently in space. Such pulses are produced by spatio-temporal modulators [232, 233]. The field produced by them is a coherent superposition of waves with different frequencies whose amplitudes and phases can arbitrarily vary in space and with frequency. This modulation can be chosen so that all the frequency components converge at the same focal spot at the same time forming an ultrashort pulse of the nanolocalized optical fields.

As an example we consider a silver [32] nanowedge illustrated in Fig. 1.20 whose maximum thickness is $d_m = 30\,\text{nm}$, the minimum thickness is $d_f = 4\,\text{nm}$, and whose length (in the y direction) is $L = 5\,\mu\text{m}$. Trajectories calculated by the Wentzel-Kramers-Brillouin (WKB) method in Ref. [214] for $\hbar\omega = 2.5\,\text{eV}$ are shown by lines (color used only to guide eye); the nanofocus is indicated by a bold red dot. In contrast to focusing by a conventional lens, the SPP rays are progressively bent toward the wedge slope direction.

Now consider the problem of coherent control. The goal is to excite a spatiotemporal waveform at the thick edge of the wedge in such a way that the propagating SPP rays converge at an arbitrary nanofocus at the sharp edge where an ultrashort pulse is formed. To solve this problem, we use the idea of back-propagation or time-reversal [224, 225, 239]. We generate rays at the nanofocus as an ultrashort pulse containing just several oscillations of the optical field. Propagating these rays, we find amplitudes and phases of the fields at the thick edge at each frequency as given by the complex propagation phase (eikonal) $\Phi(\boldsymbol{\rho})$, where $\boldsymbol{\rho}$ is a 2-d coordinate vector in the plane of the wedge. Then we complex conjugate the amplitudes of frequency components, which corresponds to the time reversal. We also multiply these amplitudes by $\exp(2\text{Im}\,\Phi)$, which pre-compensates for the Ohmic losses. This provides the required phase and amplitude modulation at the thick edge of the wedge.

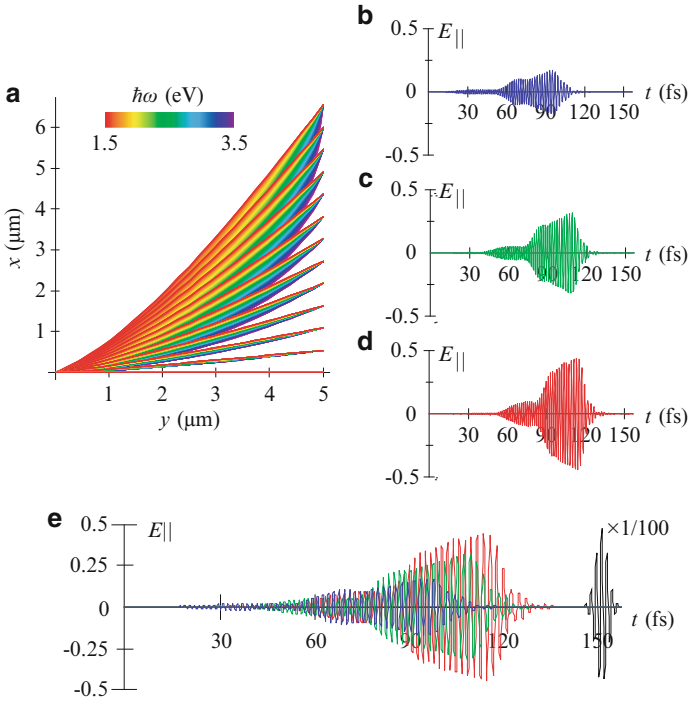

Fig. 1.21 (**a**) Trajectories (rays) of SPP packets propagating from the thick edge to the nanofocus displayed in the xy plane of the wedge. The frequencies of the individual rays in a packet are indicated by color as coded by the bar at the top. (**b**)–(**d**) Spatiotemporal modulation of the excitation pulses at the thick edge of the wedge required for nanofocusing. The temporal dependencies (waveforms) of the electric field for the phase-modulated pulses for three points at the thick edge boundary: two extreme points and one at the center, as indicated, aligned with the corresponding x points at panel (**a**). (**e**) The three excitation pulses of panels (**b**)–(**d**) (as shown by their colors), superimposed to elucidate the phase shifts, delays, and shape changes between these pulses. The resulting ultrashort pulse at the nanofocus is shown by the *black line*. The scale of the electric fields is arbitrary but consistent throughout the figure

We show an example of such calculations in Fig. 1.21. Panel (a) displays the trajectories of SPPs calculated [214] by the WKB method. The trajectories for different frequencies are displayed by colors corresponding to their visual perception. There is a very significant spectral dispersion: trajectories with higher frequencies are much more curved. The spatial-frequency modulation that we have found succeeds in bringing all these rays (with different frequencies and emitted at different x points) to the same nanofocus at the sharp edge.

The required waveforms at different x points of the thick edge of the wedge are shown in Fig. 1.21b–d where the corresponding longitudinal electric fields are shown. The waves emitted at large x, i.e., at points more distant from the nanofocus, should be emitted significantly earlier to pre-compensate for the longer propagation times. They should also have different amplitudes due to the differences

in the adiabatic compression along the different rays. Finally, there is clearly a negative chirp (gradual decrease of frequency with time). This is due to the fact that the higher frequency components propagate more slowly and therefore must be emitted earlier to form a coherent ultrashort pulse at the nanofocus.

In Fig. 1.21e we display together all three of the representative waveforms at the thick edge to demonstrate their relative amplitudes and positions in time. The pulse at the extreme point in x (shown by blue) has the longest way to propagate and therefore is the most advanced in time. The pulse in the middle point (shown by green) is intermediate, and the pulse at the center ($x = 0$, shown by red) is last. One can notice also a counterintuitive feature: the waves propagating over longer trajectories are smaller in amplitude though one may expect the opposite to compensate for the larger losses. The explanation is that the losses are actually insignificant for the frequencies present in these waveforms, and the magnitudes are determined by adiabatic concentration factor.

Figure 1.21e also shows the resulting ultrashort pulse in the nanofocus. This is a transform-limited, Gaussian pulse. The propagation along the rays completely compensates the initial phase and amplitude modulation, exactly as intended. As a result, the corresponding electric field of the waveform is increased by a factor of 100. Taking the other component of the electric field and the magnetic field into account, the corresponding increase of the energy density is by a factor $\sim 10^4$ with respect to that of the SPPs at the thick edge.

To briefly conclude, an approach [214] to full coherent control of spatiotemporal energy localization on the nanoscale has been presented. From the thick edge of a plasmonic metal nanowedge, SPPs are launched, whose phases and amplitudes are independently modulated for each constituent frequency of the spectrum and at each spatial point of the excitation. This pre-modulates the departing SPP wave packets in such a way that they reach the required point at the sharp edge of the nanowedge in phase, with equal amplitudes forming a nanofocus where an ultrashort pulse with required temporal shape is generated. This system constitutes a "nanoplasmonic portal" connecting the incident light field, whose features are shaped on the microscale, with the required point or features at the nanoscale.

1.4.6 Experimental Demonstrations of Coherent Control on the Nanoscale

The ideas of the coherent control of the nanoscale distribution of ultrafast optical fields both space and in time, which have been introduced theoretically in Refs. [149, 199, 214, 218, 222, 240, 241], have been investigated and confirmed experimentally. Using the full phase and amplitude modulation of the excitation-pulse wavefront in both polarizations (the so-called polarization pulse shaping), the experiments have achieved both spatial control [123, 219] and spatiotemporal control [221] on nanometer-femtosecond scale.

Recently spatiotemporal nanofocusing via the adiabatic concentration along the lines of ideas presented above in Sect. 1.4.5 has been successfully demonstrated experimentally [21]. In this work, a shaped femtosecond pulse has been coupled by a grating to a TM_0 SPP mode on the surface of an adiabatically-tapered nanocone. The spatiotemporal concentration of optical energy in space to a ∼10 nm region and in time to a 15 fs duration (Fourier-transform limited, i.e., the shortest possible at a given bandwidth). Indeed the position of the nanofocus in Ref. [21] is always the tip of the nanocone; so the possibility of moving the nanofocus in space is not available.

The ideas of employing the spatial modulation of the excitation wavefront [214] described above in Sect. 1.4.5 have been experimentally tested and confirmed for continuous wave (CW) excitation [215, 216]. We will present some of these experimental results below in this section.

We start with experiments on polarization-shaping coherent control that we adapt from Ref. [219]. The corresponding experimental approach is schematically illustrated in Fig. 1.22. Polarization-shaped ultrashort laser pulses illuminate a planar nanostructure, with two-photon photoemission electron microscopy (PEEM) [242] providing the feedback signal from the nanoscale field distribution that is essential for adaptive near-field control.

The spatial resolution of two-photon PEEM (∼50 nm) is determined by its electron optics and is, thus, independent of the electromagnetic light-field diffraction limit. The sensitivity of the two-photon PEEM patterns to the optical field intensities arises from the nonlinear two-photon photoemission process whose intensity is proportional to the time-integrated fourth power of the local electric-field amplitude. With these elements in place, a user-specified nanoscopic optical field distribution is realized by processing recorded photoemission patterns in an evolutionary algorithm that directs the iterative optimization of the irradiating laser pulse shape.

The basic idea of the experiment is that the measured PEEM pattern identifies the origin of ejected photoelectrons and hence the regions of high local field intensity. A controlled variation of the PEEM pattern then proves the spatial control over the nanoscopic field distribution. We have already discussed such an approach above – see Fig. 1.10 [123] and the corresponding discussion in Sect. 1.3.6.

The nanostructure used consists of circular Ag disks with 180 nm diameter and 30 nm height, fabricated by electron-beam lithography on a conductive, 40-nm-thick indium-tin oxide (ITO) film grown on a quartz substrate. The disks are arranged into three dimers that form the arms of a star-like shape (Fig. 1.22a, lower right). The whole nanostructure is about 800 nm across, while the gap between two of the dimer disks is ∼10 nm wide. After inspection by scanning-electron microscopy (SEM), the sample is mounted in the ultrahigh-vacuum PEEM set-up. The deposition of a small amount of caesium (∼0.1 monolayers) reduces the work function of the Ag nanostructure to about 3.1 eV, that is, just below the threshold for two-photon photoemission with 790 nm photons.

The PEEM pattern obtained after maximization of the photoemission from the upper two arms of the Ag nanostructure in shown in Fig. 1.22c. It shows strong emission from these two upper arms and almost no emission from the bottom arm. Analogously, the photoemission after minimization of the upper part PEEM

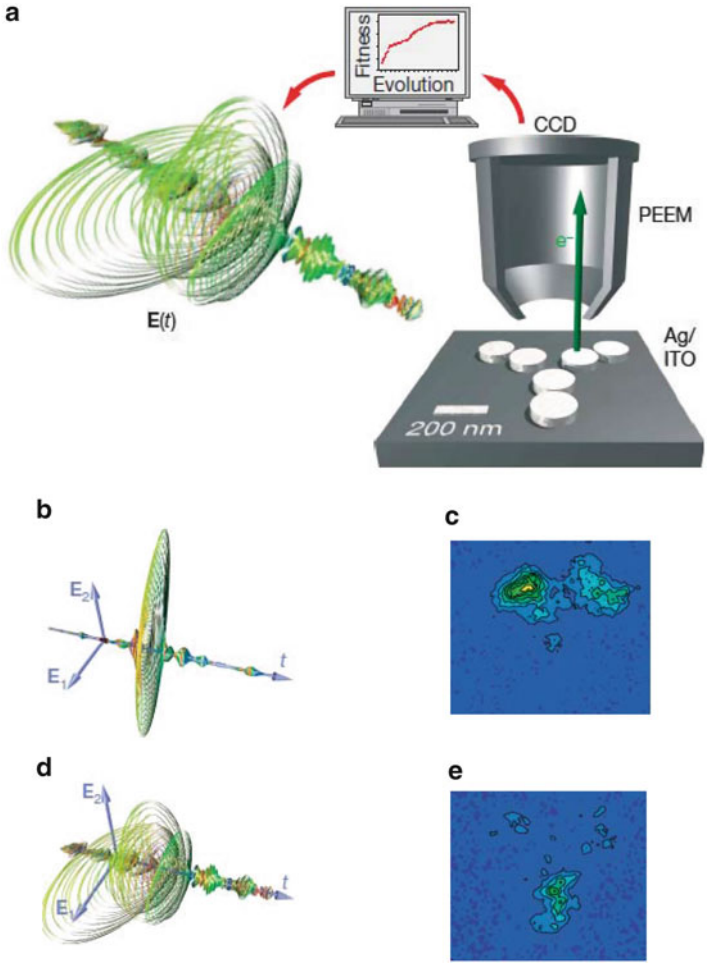

Fig. 1.22 Schematic and experimental results of coherent control with polarization shaping (Adapted from Ref. [219]). (**a**) Schematic of the experiment. A polarization shaper for ultrashort laser pulses controls the temporal evolution of the vectorial electric field $E(t)$ on a femtosecond timescale. These pulses illuminate a planar nanostructure in an ultrahigh-vacuum chamber that is equipped with a photoemission electron microscope (PEEM). The nanostructure consists of six circular Ag islands on an indium-tin oxide (ITO) film and a quartz substrate. A computer-controlled charge-coupled device (CCD) camera records the photoemission image and provides a feedback signal for an evolutionary learning algorithm. Iterative optimization of the pulse-shaper settings leads to an increase in the fitness value and correspondingly allows control over the nanooptical fields. (**b**) and (**c**) The optimal laser pulses, as experimentally characterized, display complex temporal electric-field evolution for the objectives of (**b**) minimizing and (**d**) maximizing the concentration of the excitation on the lower branch. E_1 and E_2 indicate the two field components that are phase-modulated in the polarization pulse shaper in the first and second LCD layer, respectively. They are at 45° angles with respect to the p-polarization. The overall time window shown is 2 ps. (**c**) The experimental PEEM image after adaptive maximization of the upper region intensity using complex polarization-shaped laser pulses (fittest individual of the final generation) shows predominant emission from the upper region. (**e**) Photoemission after minimization of the intensity in the upper region is concentrated in the lower region

brightness (Fig. 1.22e) occurs mainly in the lower area while the contribution from the upper two arms is extremely weak. The adaptively determined solution to each optimization problem has been proven to be robust with respect to slight imperfections in the experimental nanostructures. These successful optimizations demonstrate that polarization pulse shaping allows adaptive control of the spatial distribution of photoelectrons on a subwavelength scale, and thus of the nanoscopic optical fields that induce photoemission.

The optimally polarization-shaped laser pulses after adaptive maximization and minimization described above are shown in Fig. 1.22b, d, respectively, as determined by dual-channel spectral interferometry [243, 244]. In this representation, the shape of the quasi-three-dimensional figure indicates the temporal evolution of the polarization state of the electric field, with the color representing the instantaneous oscillation frequency. Contributions from both transverse polarization components are visible in each of the two cases. Whereas the upper-region photoemission maximization is achieved with a comparatively simple time evolution, the corresponding minimization requires a more complex field with varying degrees of ellipticity, orientation and temporal amplitudes.

Our idea [214] of the coherent control on the nanoscale by spatial modulation (shaping) of the excitation waveform has been developed theoretically [241] and experimentally [215, 216]. The coherent control of nanoscale distribution of local optical fields based on CW excitation aimed at achieving a deterministic control of plasmonic fields by using the spatial shaping of high order beams such as Hermite-Gaussian (HG) and Laguerre-Gaussian (LG) beams has been carried out in Ref. [215]. It has been shown experimentally that the spatial phase shaping of the excitation field provides an additional degree of freedom to drive optical nanoantennas and consequently control their near field response.

An example of such a deterministic coherent control is illustrated in Fig. 1.23. It shows a double gap antenna formed by three 500 nm aligned gold bars forming two identical 50 nm air gaps separated by 500 nm. For reference, in panel (a) it displays a measured two-photon luminescence (TPL) map when driving the whole antenna with a Gaussian beam linearly polarized along the x-axis. Note that similar to what has been discussed above in Sect. 1.4.4, in particular, in conjunction with Fig. 1.19, the TPL reflects the time-averaged distribution of the local field intensity $\langle I^2(\mathbf{r})\rangle$. As we see from Fig. 1.23a and as expected, a field concentration is observed in both gaps. Figure 1.23b, c show TPL maps recorded when the π-phase shift of a HG10 beam coincides, respectively, with the right and left gaps. These data demonstrate how a suitable positioning of the phase jump over the double antenna enables us to selectively switch on and off one of the two hot-spot sites.

Even closer to the original idea [214] that a plasmonic wavefront can be shaped and focused at a predetermined spot by a spatial phase modulation of the excitation waveform incident on optically-addressable launch pads is a recent publication [216]. This article achieves controlled launching and propagation of SPPs by spatially designing the amplitude and phase of the incident light. The chosen amplitude profile, consisting of four bright ("on") SPP launching platforms and one central dark ("off") arena, fully separates plasmonic effects from photonic

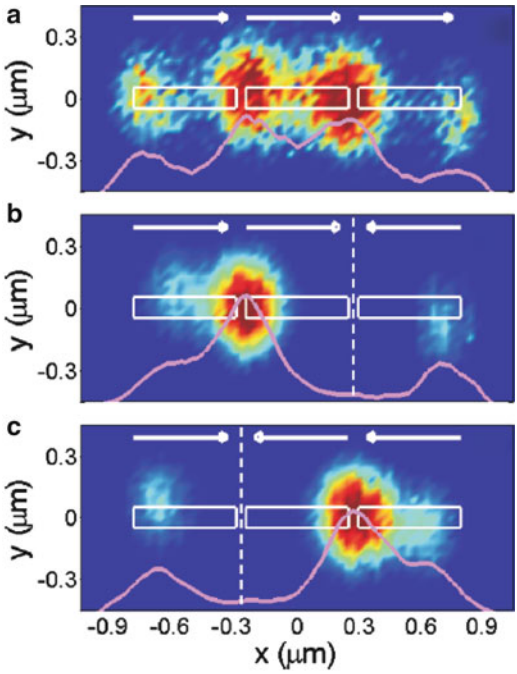

Fig. 1.23 Experimental results on spatial coherent control of nanoantennas (Adapted from Ref. [215]). Experimental two-photon luminescence (TPL) maps recorded for (**a**) a Gaussian beam and (**b**, **c**) a Hermite-Gaussian (HG10) beam whom phase shift (indicated by the *vertical dashed line*) coincides with (**b**) the right gap and (**c**) the left gap

effects and in addition is the necessary starting point for later focusing and scanning experiments. Any intensity detected inside the arena is purely plasmonic.

Adapting from Ref. [216], we present the achieved SPP focusing in Fig. 1.24. A phase optimization loop is used to focus SPPs at a pre-chosen target. This loop yields the optimal phase for each launching pad ("superpixel") as well as the relative intensity to focus. The amplitude profile is the same in all cases including the bare gold case, with four launching areas and a central dark arena where only SPPs can propagate. The incident polarization is diagonal in relation to the grating lines so as to have all available angles (2π range) contributing to the focus, thereby maximizing the numerical aperture and resolution.

Successful focusing at the center of the SPP arena is shown in Fig. 1.24a. The structured SPP wavefront produces an intensity in the designated target that is at least 20 times higher than the average SPP background of an unstructured wavefront. The measured size of the plasmonic focus is 420 nm, consistent with the diffraction limit of the SPPs. The flexibility of the method (scanning the focus) is demonstrated in Fig. 1.24b, c, which shows the SPP focus relocated without mechanical motion to controlled positions in the plasmonic arena.

The work of Ref. [216] has fully implemented the idea of Ref. [214] on the spatial-phase-modulation control of the SPP wavefronts to position a SPP nanofocus at a desired location at the surface. However, it employs only CW excitation and does not exploit a potential femtosecond temporal degree of freedom to achieve such a nanofocusing at a predetermined moment of time as in Ref. [214].

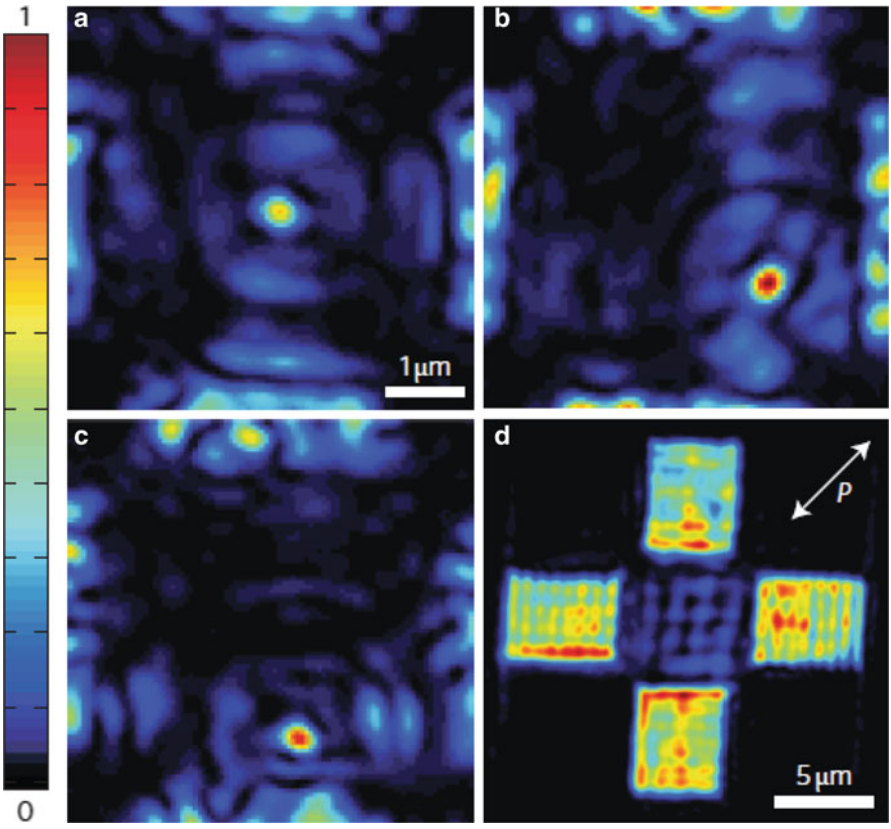

Fig. 1.24 Experiment on coherent control (dynamic focusing) of SPPs (Adapted from Ref. [216]). (**a**) Relative phases of the superpixels are optimized to focus SPPs at the center of the SPP arena. The intensity in the target spot is purely plasmonic and 20 times higher than the average background of an unstructured plasmonic wavefront. The focus size is diffraction limited by the detecting optics. (**b**) and (**c**), Demonstration of SPP focusing on freely chosen targets in the SPP arena. (**d**) Background reference of an unstructured SPP wavefront (uniform phase profile)

1.5 Quantum Nanoplasmonics: Spaser and Nanoplasmonics with Gain

1.5.1 Introduction to Spasers and Spasing

Not just a promise anymore [245], nanoplasmonics has delivered a number of important applications: ultrasensing [246], scanning near-field optical microscopy [194,247], SP-enhanced photodetectors [53], thermally assisted magnetic recording [248], generation of extreme uv [138], biomedical tests [246,249], SP-assisted thermal cancer treatment [250], plasmonic enhanced generation of extreme ultraviolet

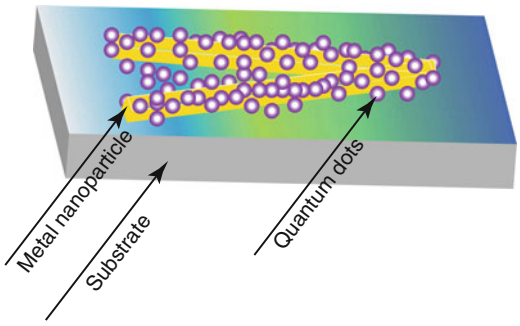

Fig. 1.25 Schematic of the spaser as originally proposed in Ref. [31]. The resonator of the spaser is a metal nanoparticle shown as a gold V-shape. It is covered by the gain medium depicted as nanocrystal quantum dots. This active medium is supported by a neutral substrate

(EUV) pulses [138] and extreme ultraviolet to soft x-ray (XUV) pulses [251], and many others – see also Ref. [23].

To continue its vigorous development, nanoplasmonics needs an active device – near-field generator and amplifier of nanolocalized optical fields, which has until recently been absent. A nanoscale amplifier in microelectronics is the metal-oxide-semiconductor field effect transistor (MOSFET) [252, 253], which has enabled all contemporary digital electronics, including computers and communications and enabled the present day technology as we know it. However, the MOSFET is limited by frequency and bandwidth to $\lesssim$100 GHz, which is already a limiting factor in further technological development. Another limitation of the MOSFET is its high sensitivity to temperature, electric fields, and ionizing radiation, which limits its use in extreme environmental conditions and nuclear technology and warfare.

An active element of nanoplasmonics is the spaser (Surface Plasmon Amplification by Stimulated Emission of Radiation), which was proposed [31, 254] as a nanoscale quantum generator of nanolocalized coherent and intense optical fields. The idea of spaser has been further developed theoretically [139–141, 255]. Spaser effect has recently been observed experimentally [256]. Also a number of SPP spasers (also called nanolasers) have been experimentally observed [257–260].

Spaser is a nanoplasmonic counterpart of laser: it is a quantum generator and nanoamplifier where photons as the generated quanta are replaced by SPs. Spaser consists of a metal nanoparticle, which plays a role of the laser cavity (resonator), and the gain medium. Figure 1.25 schematically illustrates geometry of a spaser introduced in the original article [31], which contains a V-shaped metal nanoparticle surrounded by a layer of semiconductor nanocrystal quantum dots.

1.5.2 Spaser Fundamentals

As we have already mentioned, the spaser is a nanoplasmonic counterpart of the laser [31, 255]. The laser has two principal elements: resonator (or cavity) that supports photonic mode(s) and the gain (or active) medium that is population-inverted and supplies energy to the lasing mode(s). An inherent limitation of the

laser is that the size of the laser cavity in the propagation direction is at least half wavelength and practically more than that even for the smallest lasers developed [257, 258, 261]. In the spaser [31] this limitation is overcome. The spasing modes are surface plasmons (SPs) whose localization length is on the nanoscale [78] and is only limited by the minimum inhomogeneity scale of the plasmonic metal and the nonlocality radius [35] $l_{nl} \sim 1$ nm. So, the spaser is truly nanoscopic – its minimum total size can be just a few nanometers.

The resonator of a spaser can be any plasmonic metal nanoparticle whose total size R is much less than the wavelength λ and whose metal thickness is between l_{nl} and l_s, which supports a SP mode with required frequency ω_n. This metal nanoparticle should be surrounded by the gain medium that overlaps with the spasing SP eigenmode spatially and whose emission line overlaps with this eigenmode spectrally [31]. As an example, we consider a model of a nanoshell spaser [139, 255, 262], which is illustrated in Fig. 1.26. Panel (a) shows a silver nanoshell carrying a single SP (plasmon population number $N_n = 1$) in the dipole eigenmode. It is characterized by a uniform field inside the core and hot spots at the poles outside the shell with the maximum field reaching $\sim 10^6$ V/cm. Similarly, Fig. 1.26b shows the quadrupole mode in the same nanoshell. In this case, the mode electric field is non-uniform, exhibiting hot spots of $\sim 1.5 \times 10^6$ V/cm of the modal electric field at the poles. These high values of the modal fields is the underlying physical reason for a very strong feedback in the spaser. Under our conditions, the electromagnetic retardation within the spaser volume can be safely neglected. Also, the radiation of such a spaser is a weak effect: the decay rate of plasmonic eigenmodes is dominated by the internal loss in the metal. Therefore, it is sufficient to consider only quasistatic eigenmodes [29, 78] and not their full electrodynamic counterparts [263].

For the sake of numerical illustrations of our theory, we will use the dipole eigenmode (Fig. 1.26a). There are two basic ways to place the gain medium: (i) outside the nanoshell, as shown in panel (c), and (ii) in the core, as in panel (d), which was originally proposed in Ref. [262]. As we have verified, these two designs lead to comparable characteristics of the spaser. However, the placement of the gain medium inside the core illustrated in Fig. 1.26d has a significant advantage because the hot spots of the local field are not covered by the gain medium and are sterically available for applications.

Note that any l-multipole mode of a spherical particle is, indeed, $2l + 1$-times degenerate. This may make the spasing mode to be polarization unstable, like in lasers without polarizing elements. In reality, the polarization may be clamped and become stable due to deviations from the perfect spherical symmetry, which exist naturally or can be introduced deliberately. More practical shape for a spaser may be a nanorod, which has a mode with the stable polarization along the major axis. However, a nanorod is a more complicated geometry for theoretical treatment, and we will consider it elsewhere.

The level diagram of the spaser gain medium and the plasmonic metal nanoparticle is displayed in Fig. 1.26e along with a schematic of the relevant energy transitions in the system. The gain medium chromophores may be semiconductor

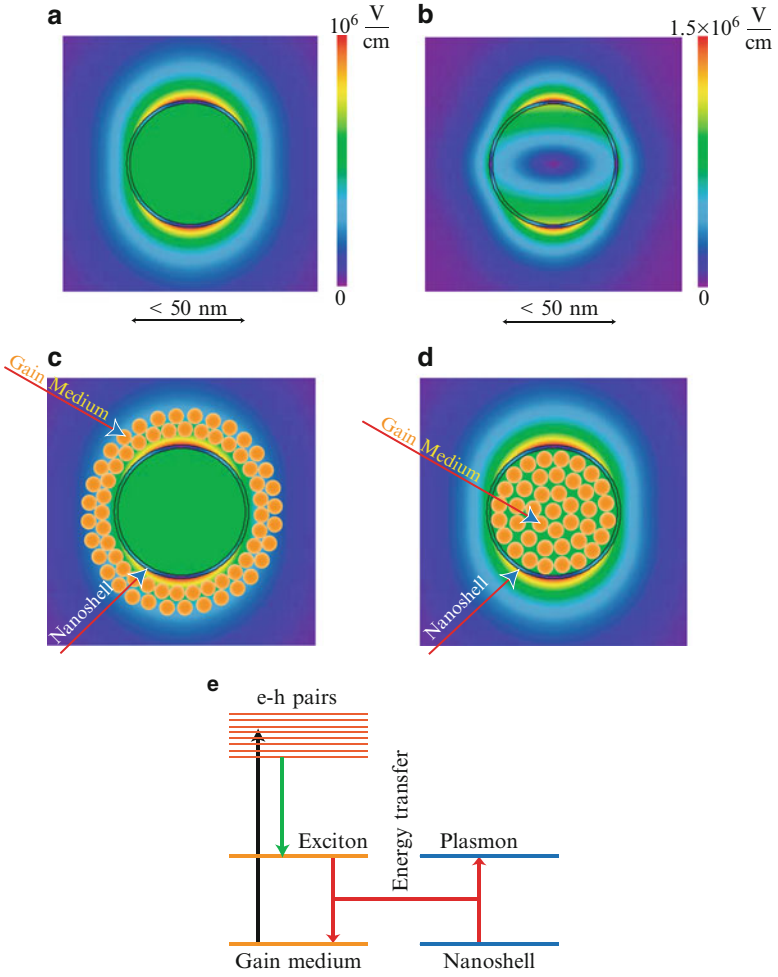

Fig. 1.26 Schematic of spaser geometry, local fields, and fundamental processes leading to spasing (Adapted from Ref. [139]). (**a**) Nanoshell geometry and the local optical field distribution for one SP in an axially-symmetric dipole mode. The nanoshell has aspect ratio $\eta = 0.95$. The local field magnitude is color-coded by the scale bar in the *right-hand side* of the panel. (**b**) The same as (**a**) but for a quadrupole mode. (**c**) Schematic of a nanoshell spaser where the gain medium is outside of the shell, on the background of the dipole-mode field. (**d**) The same as (**c**) but for the gain medium inside the shell. (**e**) Schematic of the spasing process. The gain medium is excited and population-inverted by an external source, as depicted by the *black arrow*, which produces electron-hole pairs in it. These pairs relax, as shown by the *green arrow*, to form the excitons. The excitons undergo decay to the ground state emitting SPs into the nanoshell. The plasmonic oscillations of the nanoshell stimulates this emission, supplying the feedback for the spaser action

nanocrystal quantum dots [31, 264], dye molecules [265, 266], rare-earth ions [262], or electron-hole excitations of an unstructured semiconductor [257, 261]. For certainty, we will use a semiconductor-science language of electrons and holes in quantum dots.

The pump excites electron-hole pairs in the chromophores (Fig. 1.26e), as indicated by the vertical black arrow, which relax to form excitons. The excitons constitute the two-level systems that are the donors of energy for the SP emission into the spasing mode. In vacuum, the excitons would recombine emitting photons. However, in the spaser geometry, the photoemission is strongly quenched due to the resonance energy transfer to the SP modes, as indicated by the red arrows in the panel. The probability of the radiativeless energy transfer to the SPs relative to that of the radiative decay (photon emission) is given by the so-called Purcell factor

$$\sim \frac{\lambda\!\!\!^{-3} Q}{R^3} \gg 1 \,, \tag{1.61}$$

where R is a characteristic size of the spaser metal core. Thus this radiativeless energy transfer to the spaser mode is the dominant process whose probability is by orders of magnitude greater than that of the free-space (far-field) emission.

The plasmons already in the spaser mode create the high local fields that excite the gain medium and stimulate more emission to this mode, which is the feedback mechanism. If this feedback is strong enough, and the life time of the spaser SP mode is long enough, then an instability develops leading to the avalanche of the SP emission in the spasing mode and spontaneous symmetry breaking, establishing the phase coherence of the spasing state. Thus the establishment of spasing is a non-equilibrium phase transition, as in the physics of lasers.

1.5.3 Brief Overview of Latest Progress in Spasers

After the original theoretical proposal and prediction of the spaser [31], there has been an active development in this field, both theoretical and experimental. There has also been a US patent issued on spaser [254].

Among theoretical developments, a nanolens spaser has been proposed [267], which possesses a nanofocus ("the hottest spot") of the local fields. In Refs. [31, 267], the necessary condition of spasing has been established on the basis of the perturbation theory.

There have been theories published describing the SPP spasers (or, "nanolasers" as sometimes they are called) phenomenologically, on the basis of classic linear electrodynamics by considering the gain medium as a dielectric with a negative imaginary part of the permittivity, e.g., [262]. Very close fundamentally and technically are works on the loss compensation in metamaterials [268–271]. Such linear-response approaches do not take into account the nature of the spasing

as a non-equilibrium phase transition, at the foundation of which is spontaneous symmetry breaking: establishing coherence with an arbitrary but sustained phase of the SP quanta in the system [139]. Spaser is necessarily a deeply-nonlinear (nonperturbative) phenomenon where the coherent SP field always saturates the gain medium, which eventually brings about establishment of the stationary (or, continuous wave, CW) regime of the spasing [139]. This leads to principal differences of the linear-response results from the microscopic quantum-mechanical theory in the region of spasing, as we discuss below in conjunction with Fig. 1.29.

There has also been a theoretical publication on a bowtie spaser (nanolaser) with electrical pumping [272]. It is based on balance equations and only the CW spasing generation intensity is described. Yet another theoretical development has been a proposal of the lasing spaser [273], which is made of a plane array of spasers.

There have also been a theoretical proposal of a spaser ("nanolaser") consisting of a metal nanoparticle coupled to a single chromophore [274]. In this paper, a dipole-dipole interaction is illegitimately used at very small distances r where it has a singularity (diverging for $r \to 0$), leading to a dramatically overestimated coupling with the SP mode. As a result, a completely unphysical prediction of CW spasing due to single chromophore has been obtained [274]. In contrast, our theory [139] is based on the full (exact) field of the spasing SP mode without the dipole (or, any multipole) approximation. As our results of Sect. 1.5.5 below show, hundreds of chromophores per metal nanoparticle are realistically requited for the spasing even under the most favorable conditions.

There has been a vigorous experimental investigation of the spaser and the concepts of spaser. Stimulated emission of SPPs has been observed in a proof-of-principle experiment using pumped dye molecules as an active (gain) medium [265]. There have also been later experiments that demonstrated strong stimulated emission compensating a significant part of the SPP loss [266, 275–278]. As a step toward the lasing spaser, the first experimental demonstration has been reported of a partial compensation of the Joule losses in a metallic photonic metamaterial using optically pumped PbS semiconductor quantum dots [264]. There have also been experimental investigations reporting the stimulated emission effects of SPs in plasmonic metal nanoparticles surrounded by gain media with dye molecules [279, 280].

The full loss compensation and amplification of the long-range SPPs at $\lambda = 882$ nm in a gold nanostrip waveguide with a dyes solution as a gain medium has been observed [281]. Another example of full loss compensation has recently been obtained for thin ($\sim$20 nm thickness) gold stripes (width $\sim$1 μm) surrounded by a gain medium containing donor-acceptor with a Förster energy transfer to increase the Stokes shift and decrease absorption at the probe frequency.

At the present time, there have been a number of the successful experimental observations of the spaser and SPP spasers (the so-called nanolasers). An electrically-pumped nanolaser with semiconductor gain medium have been demonstrated [257] where the lasing modes are SPPs with a one-dimensional confinement to a $\sim$50 nm size. Other electrically-pumped nanolasers (SPP spasers) have recently been fabricated and their lasing observed based on a diode with an intrinsic InGaAs

gain media and silver nanocavities as plasmonic cores [282–284]. The latest of these nanolasers [284] operates at a room temperature and has a relatively small cavity volume $V_c \approx 0.67\lambda^3$, where vacuum wavelength $\lambda = 1{,}591$ nm. This volume is still much larger than the modal volumes of the spasers with tighter confinement, especially SP-mode spasers – see below.

A nanolaser with an optically-pumped semiconductor gain medium and a hybrid semiconductor/metal (CdS/Ag) SPP waveguide has been demonstrated with an extremely tight transverse (two-dimensional) mode confinement to ∼10 nm size [258]. This has been followed by the development of CdS/Ag nanolasers generating a visible single mode at a room temperature with a tight one-dimensional confinement (∼20 nm) and a two-dimensional confinement in the plane of the structure to an area $\sim 1\,\mu m^2$ [259]. A highly efficient SPP spaser in the communication range ($\lambda = 1.46\,\mu m$) with an optical pumping based on a gold film and an InGaAs semiconductor quantum-well gain medium has recently been reported [260].

Another class of spasers observed are random spasers comprised of a rough metal nanofilm as a plasmonic component and a dye-doped polymeric film as a gain medium [285]. The spasing in such systems competes with loss compensation for SPPs propagating at the interface – see also Sect. 1.5.7.

Hitorically, the first spaser observed was a nanoparticle spaser [256]. This spaser is a chemically synthesized gold nanosphere of radius 7 nm surrounded by a dielectric shell of a 21 nm outer radius containing immobilized dye molecules. Under nanosecond optical pumping in the absorption band of the dye, this spaser develops a relatively narrow-spectrum and intense visible emission that exhibits a pronounced threshold in pumping intensity. The observed characteristics of this spaser are in an excellent qualitative agreement and can be fully understood on the basis of the corresponding theoretical results described below in Sect. 1.5.5.

1.5.3.1 Nanospaser with Semiconductor Gain Media

It is of both fundamental and applied importance to develop nanoscale-size spasers (nanospasers) with semiconductor gain media. The photochemical and electrochemical stability of the semiconductor gain media is the main attraction of such a design. Belonging to this class, spasers have recently been fabricated and their operation observed, comprised of a InGaN-core/InN-shell semiconductor-nanorod gain medium and silver film as a plasmonic component [286, 287]. They generate on localized SP modes. One of these [287] is a nanospaser with a deeply subwavelength mode size based on an epitaxial silver nanofilm [287]. Such a design bears a promise of practical applications due to its stability and small modal volume leading to high operational speed – see below Sect. 1.5.6.

In Fig. 1.27, we display geometry of this InGaN-core/InN-shell nanorod spaser and properties of its spasing mode. The active region of the spaser (Fig. 1.27a, left panel) is a core-shell nanocylinder with a 30-nm diameter core of InGaN surrounded by think shell if GaN. The latter is a wide band-gap semiconductor that plays a role of insulator. The active nanorod is separated by the metal by a 5-nm layer of silica.

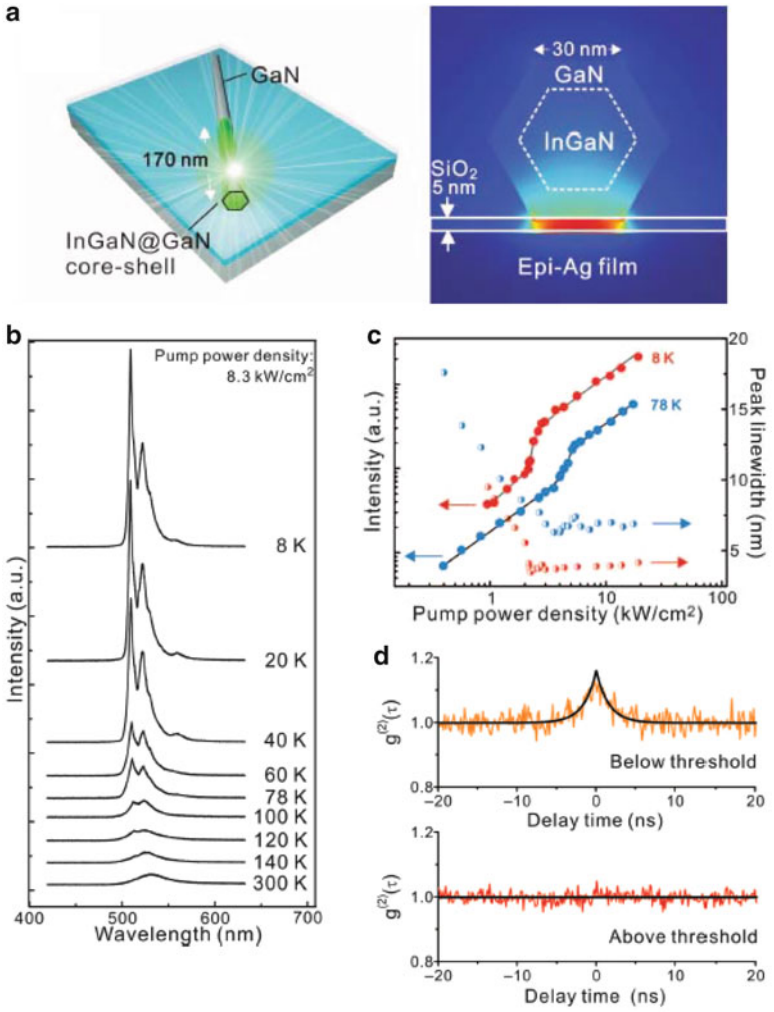

Fig. 1.27 InGaN nanospaser and its properties. (**a**) Schematics of geometry of InGaN/GaN core-shell nanospaser (*left*) and theoretical intensity of its spasing eigenmode. (**b**) Series of emission spectra: Temperature-dependent spasing behavior from 8 to 300 K. The spasing threshold at 140 K is clearly visible. (**c**) The L-L (light-light) plots at the main lasing peak (510 nm) are shown with the corresponding linewidth-narrowing behavior when the spaser is measured at 8 K (*red*) and 78 K (*blue*), with lasing thresholds of 2.1 and 3.7 $\mathrm{kW/cm^2}$, respectively. (**d**) Second-order photon correlation function $g^{(2)}(\tau)$ measured at 8 K. The *upper curve* is recorded below the spasing threshold, and the *lower* above the threshold (Adapted from Ref. [287])

The plasmonic component of this spaser is a flat layer of epitaxial silver. The high monocrystalline quality of the silver film is instrumental in reducing the threshold of the spaser and increasing its output. The calculated intensity for the spasing eigenmode is shown in the right panel of Fig. 1.27a. Similar to the gap modes introduced in Ref. [288], this eigenmode is concentrated in the thin layer of a

low-permittivity dielectric (silica) between the two high-permittivity media: GaN and silver. The modal fields do penetrate sufficiently into the gain medium providing the feedback necessary for the spaser functioning.

Under $8.3\,\mathrm{kW/cm^2}$ optical pumping with frequency above the band gap of InGaN, a series of the emission spectra of a single spaser is displayed in Fig. 1.27b, At a room temperature, $T = 300\,\mathrm{K}$, the emission is a spontaneous fluorescence in a wide yellow-green spectral band near the band gap of InGaN. The first evidence of the spasing appears at $T = 120\,\mathrm{K}$ as a small notch at the green side of the spectrum. As the temperature decreases to $T = 8\,\mathrm{K}$, the narrow line at $\lambda \approx 500\,\mathrm{nm}$ becomes dominant and narrow. This change of the spectrum over the threshold is in a qualitative agreement with theory – see below Sect. 1.5.5 and, in particular, Fig. 1.29d–f.

The light-line (L-L) line is the dependence of the light intensity out (the intensity of the radiation emitted by the spaser within the linewidth spectral range) versus the intensity of the pumping radiation. The theoretical prediction for the spaser is that after reaching the spasing threshold, the L-L line becomes linear with universally unit slope – see Fig. 1.29a and its discussion in Sect. 1.5.5.

The experimentally obtained L-L line of the nanorod spaser shown in Fig. 1.27c is in an excellent agreement with this prediction. Note that this figure is presented in the double-logarithmic scale. There are two curves in this figure taken at different temperatures, which are similar though at a lower temperature the intensity out is higher and the threshold is lower. The parts of the curves at lower pumping intensities are also unit-slope straight lines corresponding to spontaneous fluorescence. With the increased intensity, the curves enter a transitional regime of amplified spontaneous emission where the slopes are greater than one. The regime of developed spasing takes place at high intensities where the L-L curves become unit-slope straight lines without a saturation. As have already been mentioned above, this is a universal behavior.

This universal unsaturable behavior can be very simply understood qualitatively – cf. Ref. [289]. The excitation rate $\dot{N}_e$ of the upper spasing level is linearly proportional to pumping intensity I_p, $\dot{N}_e = \sigma_e I_p$, where σ_e is the total excitation cross section into the conduction band of the semiconductor gain medium. In the developed spasing regime, plasmon population N_n of the spasing eigenmode becomes large, asymptotically $N_n \to \infty$. Correspondingly, the stimulated decay rate, which is $\propto N_n$, becomes large and dominates over any spontaneous decay rate. Thus, all the excitation events to the conduction band end up with the emission of a SP into the spasing mode whose SP population becomes $N_n = \dot{N}_e \big/ \gamma_n$, where γ_n is the SP decay rate – see above Eq. (1.48). Finally, radiation rate $\dot{N}_r$ for a spaser becomes

$$\dot{N}_r = \sigma_e \gamma^{(r)} \big/ \gamma_n \,, \tag{1.62}$$

where $\gamma^{(r)}$ is the SP radiative decay rate, which for a plasmonic metal sphere is given by Eq. (1.16) and in, general case, by Eq. (1.56). Of course, in reality the straight-line, unsaturable L-L curves will end when the pumping intensities become

so high that the nonlinearity in the spaser metal develops (including, but not limited to, thermal nonlinearity), or optical breakdown occurs, or heat production will physically damage the spaser.

As theory shows (see below Sect. 1.5.6.1 and Fig. 1.30a), under steady pumping, the generating spaser reaches its stationary regime within ∼100 fs. Correspondingly, we expect that any fluctuation in the emission radiated by the generating spaser relaxes back to the mean level within the same time. A measure of the fluctuations of the spaser-radiation intensity $I(t)$ with time t is the second-order autocorrelation function

$$g^{(2)}(\tau) = \frac{\langle I(t+\tau)I(t)\rangle}{\langle I(t)\rangle^2}\,, \tag{1.63}$$

where τ is the delay time, and $\langle\cdots\rangle$ denotes quantum-mechanical (theory) or temporal (experiment) averaging.

Experimentally, $g^{(2)}(\tau)$ has been measured for a single spaser in Ref. [287]. The result is reproduced in Fig. 1.27d. The upper curve is recorded below the spasing threshold; at the zero delay, it shows a peak, which is characteristic of incoherent radiation. If such radiation is produced by many independent emitters, it has Gaussian statistics, and the peak value should be $g^{(2)}(0) = 2$ – this effect was introduced by Hanbury Brown and Twiss and used by them for stellar interferometry [290]. For the upper curve of Fig. 1.27d, $g^{(2)}(0)$ is significantly less. This may be due to various reasons, in particular, insufficient temporal resolution of the photodetection or partial coherence between the individual emitters of the gain medium induced by their interaction via plasmonic fields.

In sharp contrast, above the spasing threshold, the autocorrelation function in Fig. 1.27d is a constant at all delays. As we have already pointed out this is due to the fact that after an emission of a photon, the number of plasmons in the spaser is restored within ∼100 fs, while the temporal resolution of the photodetection in Ref. [287] is $\Delta\tau \gtrsim 100$ ps, i.e., three orders of magnitude coarser. The physical reason for $g^{(2)}(\tau) = \text{const}$ is that the spaser under steady-state pumping tends to keep a constant plasmon population. After the emission of a photon, this population is decreased by one. However, very rapidly, within ∼100 fs, it restores to the pre-emission level. This transitional restoration process is too fast and the photodetectors of Ref. [287] miss it, producing $g^{(2)}(\tau) = \text{const}$.

1.5.4 Equations of Spaser

1.5.4.1 Quantum Density Matrix Equations (Optical Bloch Equations) for Spaser

The SP eigenmodes $\varphi_n(\mathbf{r})$ are described by a wave equation (1.25) [31, 78]. The electric field operator of the quantized SPs is an operator [31]

$$\hat{\mathbf{E}}(\mathbf{r}) = -\sum_n A_n \nabla\varphi_n(\mathbf{r})(\hat{a}_n + \hat{a}_n^\dagger)\,, \quad A_n = \left(\frac{4\pi\hbar s_n}{\varepsilon_d s_n'}\right)^{1/2}\,, \tag{1.64}$$

where $\hat{a}_n^\dagger$ and $\hat{a}_n$ are the SP creation and annihilation operators, $-\nabla\varphi_n(\mathbf{r}) = \mathbf{E}_n(\mathbf{r})$ is the modal field of an nth mode, and $s_n' = \mathrm{Re}\,[ds(\omega_n)/d\omega_n]$. Note that we have corrected a misprint in Ref. [31] by replacing the coefficient 2π by 4π.

The spaser Hamiltonian has the form

$$\hat{H} = \hat{H}_g + \hbar\sum_n \omega_n \hat{a}_n^\dagger \hat{a}_n - \sum_p \hat{\mathbf{E}}(\mathbf{r}_p)\hat{\mathbf{d}}^{(p)}\,, \tag{1.65}$$

where $\hat{H}_g$ is the Hamiltonian of the gain medium, p is a number (label) of a gain medium chromophore, $\mathbf{r}_p$ is its coordinate vector, and $\hat{\mathbf{d}}^{(p)}$ is its dipole moment operator. In this theory, we treat the gain medium quantum mechanically but the SPs quasiclassically, considering $\hat{a}_n$ as a classical quantity (c-number) a_n with time dependence as $a_n = a_{0n}\exp(-i\omega t)$, where a_{0n} is a slowly-varying amplitude. The number of coherent SPs per spasing mode is then given by $N_p = |a_{0n}|^2$. This approximation neglects the quantum fluctuations of the SP amplitudes. However, when necessary, we will take into account these quantum fluctuations, in particular, to describe the spectrum of the spaser.

Introducing $\rho^{(p)}$ as the density matrix of a pth chromophore, we can find its equation of motion in a conventional way by commutating it with the Hamiltonian (1.65) as

$$i\hbar\dot{\rho}^{(p)} = [\rho^{(p)}, \hat{H}]\,, \tag{1.66}$$

where the dot denotes temporal derivative. We use the standard rotating wave approximation (RWA), which only takes into account the resonant interaction between the optical field and chromophores. We denote $|1\rangle$ and $|2\rangle$ as the ground and excited states of a chromophore, with the transition $|2\rangle \rightleftharpoons |1\rangle$ resonant to the spasing plasmon mode n. In this approximation, the time dependence of the nondiagonal elements of the density matrix is $\left(\rho^{(p)}\right)_{12} = \bar{\rho}_{12}^{(p)}\exp(i\omega t)$, and $\left(\rho^{(p)}\right)_{21} = \bar{\rho}_{12}^{(p)*}\exp(-i\omega t)$, where $\bar{\rho}_{12}^{(p)}$ is an amplitude slowly varying in time, which defines the coherence (polarization) for the $|2\rangle \rightleftharpoons |1\rangle$ spasing transition in a pth chromophore of the gain medium.

Introducing a rate constant Γ_{12} to describe the polarization relaxation and a difference $n_{21}^{(p)} = \rho_{22}^{(p)} - \rho_{11}^{(p)}$ as the population inversion for this spasing transition, we derive an equation of motion for the non-diagonal element of the density matrix as

$$\dot{\bar{\rho}}_{12}^{(p)} = -\left[i\,(\omega - \omega_{12}) + \Gamma_{12}\right]\bar{\rho}_{12}^{(p)} + i a_{0n} n_{21}^{(p)}\tilde{\Omega}_{12}^{(p)*}\,, \tag{1.67}$$

where

$$\tilde{\Omega}_{12}^{(p)} = -A_n \mathbf{d}_{12}^{(p)} \nabla \varphi_n(\mathbf{r}_p)/\hbar \tag{1.68}$$

is the one-plasmon Rabi frequency for the spasing transition in a pth chromophore, and $\mathbf{d}_{12}^{(p)}$ is the corresponding transitional dipole element. Note that always $\mathbf{d}_{12}^{(p)}$ is either real or can be made real by a proper choice of the quantum state phases, making the Rabi frequency $\tilde{\Omega}_{12}^{(p)}$ also a real quantity.

An equation of motion for n_{21}^{p} can be found in a standard way by commutating it with $\hat{H}$. To provide conditions for the population inversion ($n_{21}^{p} > 0$), we imply existence of a third level. For simplicity, we assume that it very rapidly decays into the excited state $|2\rangle$ of the chromophore, so its own populations is negligible. It is pumped by an external source from the ground state (optically or electrically) with some rate that we will denote g. In this way, we obtain the following equation of motion:

$$\dot{\bar{n}}_{21}^{(p)} = -4\mathrm{Im}\left[a_{0n}\bar{\rho}_{12}^{(p)}\tilde{\Omega}_{21}^{(p)}\right] - \gamma_2\left(1 + n_{21}^{(p)}\right) + g\left(1 - n_{21}^{(p)}\right) , \tag{1.69}$$

where γ_2 is the decay rate $|2\rangle \to |1\rangle$.

The stimulated emission of the SPs is described as their excitation by the coherent polarization of the gain medium. The corresponding equation of motion can be obtained using Hamiltonian (1.65) and adding the SP relaxation with a rate of γ_n as

$$\dot{a}_{0n} = [i\,(\omega - \omega_n) - \gamma_n]\,a_{0n} + i\,a_{0n}\sum_p \rho_{12}^{(p)*}\tilde{\Omega}_{12}^{(p)} . \tag{1.70}$$

As an important general remark, the system of Eqs. (1.67), (1.69), and (1.70) is highly nonlinear: each of these equations contains a quadratic nonlinearity: a product of the plasmon-field amplitude a_{0n} by the density matrix element ρ_{12} or population inversion n_{21}. Altogether, this is a six-order nonlinearity. This nonlinearity is a fundamental property of the spaser equations, which makes the spaser generation always an essentially nonlinear process that involves a noneqilibrium phase transition and a spontaneous symmetry breaking: establishment of an arbitrary but sustained phase of the coherent SP oscillations.

A relevant process is spontaneous emission of SPs by a chromophore into a spasing SP mode. The corresponding rate $\gamma_2^{(p)}$ for a chromophore at a point $\mathbf{r}_p$ can be found in a standard way using the quantized field (1.64) as

$$\gamma_2^{(p)} = 2\frac{A_n^2}{\hbar\gamma_n}\left|\mathbf{d}_{12}\nabla\varphi_n(\mathbf{r}_p)\right|^2 \frac{(\Gamma_{12} + \gamma_n)^2}{(\omega_{12} - \omega_n)^2 + (\Gamma_{12} + \gamma_n)^2} . \tag{1.71}$$

As in Schawlow-Towns theory of laser-line width [291], this spontaneous emission of SPs leads to the diffusion of the phase of the spasing state. This defines width γ_s of the spasing line as

$$\gamma_s = \frac{\sum_p \left(1 + n_{21}^{(p)}\right) \gamma_2^{(p)}}{2(2N_p + 1)} \,. \tag{1.72}$$

This width is small for a case of developed spasing when $N_p \gg 1$. However, for $N_p \sim 1$, the predicted width may be too high because the spectral diffusion theory assumes that $\gamma_s \lesssim \gamma_n$. To take into account this limitation in a simplified way, we will interpolate to find the resulting spectral width Γ_s of the spasing line as $\Gamma_s = \left(\gamma_n^{-2} + \gamma_s^{-2}\right)^{-1/2}$.

We will also examine the spaser as a bistable (logical) amplifier. One of the ways to set the spaser in such a mode is to add a saturable absorber. This is described by the same Eqs. (1.67)–(1.70) where the chromophores belonging to the absorber are not pumped by the external source directly, i.e., for them in Eq. (1.69) one has to set $g = 0$.

Numerical examples are given for a silver nanoshell where the core and the external dielectric have the same permittivity of $\varepsilon_d = 2$; the permittivity of silver is adopted from Ref. [32]. The following realistic parameters of the gain medium are used (unless indicated otherwise): $d_{12} = 1.5 \times 10^{-17}$ esu, $\hbar\Gamma_{12} = 10\,\text{meV}$, $\gamma_2 = 4 \times 10^{12}\,\text{s}^{-1}$ (this value takes into account the spontaneous decay into SPs), and density of the gain medium chromophores is $n_c = 2.4 \times 10^{20}\,\text{cm}^{-3}$, which is realistic for dye molecules but may be somewhat high for semiconductor quantum dots that were proposed as the chromophores [31] and used in experiments [264]. We will assume a dipole SP mode and chromophores situated in the core of the nanoshell as shown in Fig. 1.26d. This configuration are of advantage both functionally (because the region of the high local fields outside the shell is accessible for various applications) and computationally (the uniformity of the modal fields makes the summation of the chromophores trivial, thus greatly facilitating numerical procedures).

1.5.4.2 Equations for CW Regime

Physically, the spaser action is a result of spontaneous symmetry breaking when the phase of the coherent SP field is established from the spontaneous noise. Mathematically, the spaser is described by homogeneous differential Eqs. (1.67)–(1.70). These equations become homogeneous algebraic equations for the CW case. They always have a trivial, zero solution. However, they may also possess a nontrivial solution describing spasing. An existence condition of such a nontrivial solution is

$$(\omega_s - \omega_n + i\,\gamma_n)^{-1} \times (\omega_s - \omega_{21} + i\,\Gamma_{12})^{-1} \sum_p \left|\tilde{\Omega}_{12}^{(p)}\right|^2 n_{21}^{(p)} = -1 \,. \tag{1.73}$$

The population inversion of a pth chromophore $n_{21}^{(p)}$ is explicitly expressed as

$$n_{21}^{(p)} = (g - \gamma_2) \times \left\{ g + \gamma_2 + 4N_n \left| \tilde{\Omega}_{12}^{(p)} \right|^2 \Big/ \left[(\omega_s - \omega_{21})^2 + \Gamma_{12}^2 \right] \right\}^{-1} . \quad (1.74)$$

From the imaginary part of Eq. (1.74) we immediately find the spasing frequency ω_s,

$$\omega_s = \left(\gamma_n \omega_{21} + \Gamma_{12} \omega_n \right) / \left(\gamma_n + \Gamma_{12} \right) , \quad (1.75)$$

which generally does not coincide with either the gain transition frequency ω_{21} or the SP frequency ω_n, but is between them (this is a frequency walk-off phenomenon similar to that of laser physics). Substituting Eq. (1.75) back into Eqs. (1.74) and (1.75), we obtain a system of equations

$$\frac{\left(\gamma_n + \Gamma_{12} \right)^2}{\gamma_n \Gamma_{12} \left[(\omega_{21} - \omega_n)^2 + (\Gamma_{12} + \gamma_n)^2 \right]} \times \sum_p \left| \tilde{\Omega}_{12}^{(p)} \right|^2 n_{21}^{(p)} = 1 , \quad (1.76)$$

$$n_{21}^{(p)} = (g - \gamma_2) \times \left[g + \gamma_2 + \frac{4N_n \left| \tilde{\Omega}_{12}^{(p)} \right|^2 (\Gamma_{12} + \gamma_n)}{(\omega_{12} - \omega_n)^2 + (\Gamma_{12} + \gamma_n)^2} \right]^{-1} . \quad (1.77)$$

This system defines the stationary (CW-generation) number of SPs per spasing mode, N_n.

Since $n_{21}^{(p)} \leq 1$, from Eqs. (1.76), (1.77) we immediately obtain a necessary condition of the existence of spasing,

$$\frac{\left(\gamma_n + \Gamma_{12} \right)^2}{\gamma_n \Gamma_{12} \left[(\omega_{21} - \omega_n)^2 + (\Gamma_{12} + \gamma_n)^2 \right]} \sum_p \left| \tilde{\Omega}_{12}^{(p)} \right|^2 \geq 1 . \quad (1.78)$$

This expression is fully consistent with Ref. [31]. The following order of magnitude estimate of this spasing condition has a transparent physical meaning and is of heuristic value,

$$\frac{d_{12}^2 Q N_c}{\hbar \Gamma_{12} V_n} \gtrsim 1 , \quad (1.79)$$

where $Q = \omega / \gamma_n$ is the quality factor of SPs, V_n is the volume of the spasing SP mode, and N_c is the of number of the gain medium chromophores within

this volume. Deriving this estimate, we have neglected the detuning, i.e., set $\omega_{21} - \omega_n = 0$. We also used the definitions of A_n of Eq. (1.64) and $\tilde{\Omega}_{12}^{(p)}$ given by Eq. (1.68), and the estimate $|\nabla\varphi_n(\mathbf{r})|^2 \sim 1/V$ following from the normalization of the SP eigenmodes $\int |\nabla\varphi_n(\mathbf{r})|^2 d^3r = 1$ of Ref. [78]. The result of Eq. (1.79) is, indeed, in agreement with Ref. [31] where it was obtained in different notations.

It follows from Eq. (1.79) that for the existence of spasing it is beneficial to have a high quality factor Q, a high density of the chromophores, and a large transition dipole (oscillator strength) of the chromophore transition. The small modal volume V_n (at a given number of the chromophores N_c) is beneficial for this spasing condition: physically, it implies strong feedback in the spaser. Note that for the given density of the chromophores $n_c = N_c/V_n$, this spasing condition does not explicitly depend on the spaser size, which opens up a possibility of spasers of a very small size limited from the bottom by only the nonlocality radius $l_{nl} \sim 1\,\text{nm}$. Another important property of Eq. (1.79) is that it implies the quantum-mechanical nature of spasing and spaser amplification: this condition essentially contains the Planck constant $\hbar$ and, thus, does not have a classical counterpart. Note that in contrast to lasers, the spaser theory and Eqs. (1.78), (1.79) in particular do not contain speed of light, i.e., they are quasistatic.

Now we will examine the spasing condition and reduce it to a requirement for the gain medium. First, we substitute all the definitions and assume the perfect resonance between the generating SP mode and the gain medium, i.e., $\omega_n = \omega_{21}$. As a result, we obtain from Eq. (1.78),

$$\frac{4\pi}{3}\frac{s_n\,|\mathbf{d}_{12}|^2}{\hbar\gamma_n\Gamma_{12}\varepsilon_d s_n'}\int_V [1-\Theta(\mathbf{r})]\,|\mathbf{E}_n(\mathbf{r})|^2\,d^3r \geq 1\,, \tag{1.80}$$

where the integral is extended over the volume V of the system, and the Θ-function takes into account a simplifying realistic assumption that the gain medium occupies the entire space free from the core's metal. We also assume that the orientations of the transition dipoles $\mathbf{d}_{12}^{(p)}$ are random and average over them, which results in the factor of 3 in the denominator in Eq. (1.80).

From Eqs. (1.27) and (1.34), it follows that

$$\int_V [1-\Theta(\mathbf{r})]\,|\mathbf{E}_n(\mathbf{r})|^2\,d^3r = 1 - s_n\,. \tag{1.81}$$

Next, we give approximate expressions for the spectral parameter (1.4), which are very accurate for the realistic case of $Q \gg 1$,

$$\operatorname{Im} s(\omega) = \frac{s_n^2}{\varepsilon_d}\operatorname{Im}\varepsilon_m(\omega) = \frac{1}{Q}s_n\,(1-s_n)\,, \tag{1.82}$$

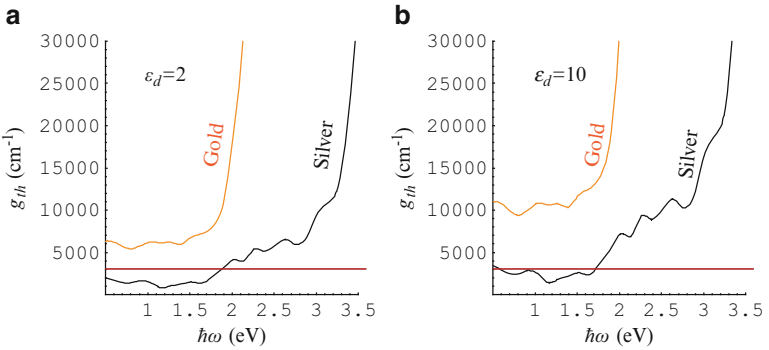

Fig. 1.28 Threshold gain for spasing g_{th} for silver and gold, as indicated in the graphs, as a function of the spasing frequency ω. The *red line* separates the area $g_{th} < 3 \times 10^3$ cm^{-1}, which can relatively easily be achieved with direct band-gap semiconductors (DBGSs). The real part of the gain medium permittivity is denoted in the corresponding panels as ε_d

where definition (1.6) is used. Taking into account Eqs. (1.47), (1.48) and (1.81), (1.82), we obtain from Eq. (1.80) a necessary condition of spasing at a frequency ω as

$$\frac{4\pi}{3}\frac{|\mathbf{d}_{12}|^2 n_c\,[1-\mathrm{Re}\,s(\omega)]}{\hbar\Gamma_{12}\mathrm{Re}\,s(\omega)\mathrm{Im}\,\varepsilon_m(\omega)} \geq 1\,, \tag{1.83}$$

For the sake of comparison, consider a continuous gain medium comprised of the same chromophores as the gain shell of the spaser. Its gain g (whose dimensionality is cm^{-1}) is given by a standard expression

$$g = \frac{4\pi}{3}\frac{\omega}{c}\frac{\sqrt{\varepsilon_d}\,|\mathbf{d}_{12}|^2 n_c}{\hbar\Gamma_{12}}\,. \tag{1.84}$$

Substituting it into Eq. (1.83), we obtain the spasing criterion in terms of the gain as

$$g \geq g_{th}\,, \quad g_{th} = \frac{\omega}{c\sqrt{\varepsilon_d}}\frac{\mathrm{Re}\,s(\omega)}{1-\mathrm{Re}\,s(\omega)}\mathrm{Im}\,\varepsilon_m(\omega)\,, \tag{1.85}$$

where g_{th} has a meaning of the threshold gain needed for spasing. Importantly, this gain depends only on the dielectric properties of the system and spasing frequency but not on the geometry of the system or the distribution of the local fields of the spasing mode (hot spots, etc.) explicitly. However note that the system's geometry (along with the permittivities) does define the spasing frequencies.

In Fig. 1.28a, b, correspondingly, we illustrate the analytical expression (1.85) for gold and silver embedded in a dielectric with $\varepsilon_d = 2$ (simulating a light glass) and $\varepsilon_d = 10$ (simulating a semiconductor), correspondingly. These are computed from Eq. (1.85) assuming that the metal core is embedded into the gain medium with the

real part of the dielectric function equal to ε_d. As we see from Fig. 1.28, the spasing is possible for silver in the near-ir communication range and the adjacent red portion of the visible spectrum for a gain $g < 3{,}000\,\mathrm{cm}^{-1}$ (regions below the red line in Fig. 1.28), which is realistically achievable with direct band-gap semiconductors (DBDSs).

1.5.5 Spaser in CW Mode

The "spasing curve" (a counterpart of the light-light curve, or L-L curve, for lasers), which is the dependence of the coherent SP population N_n on the excitation rate g, obtained by solving Eqs. (1.76) and (1.77), is shown in Fig. 1.29a for four types of the silver nanoshells with the frequencies of the spasing dipole modes as indicated, which are in the range from near-ir ($\hbar\omega_s = 1.2\,\mathrm{eV}$) to mid-visible ($\hbar\omega_s = 2.2\,\mathrm{eV}$). In all cases, there is a pronounced threshold of the spasing at an excitation rate $g_{th} \sim 10^{12}\,\mathrm{s}^{-1}$. Soon after the threshold, the dependence $N_n(g)$ becomes linear, which means that every quantum of excitation added to the active medium with a high probability is stimulated to be emitted as a SP, adding to the coherent SP population.

While this is similar to conventional lasers, there is a dramatic difference for the spaser. In lasers, a similar relative rate of the stimulated emission is achieved at a photon population of $\sim 10^{18}$–10^{20}, while in the spaser the SP population is $N_n \lesssim 100$. This is due to the much stronger feedback in spasers because of the much smaller modal volume V_n – see discussion of Eq. (1.79). The shape of the spasing curves of Fig. 1.29a (the well-pronounced threshold with the linear dependence almost immediately above the threshold) is in a qualitative agreement with the experiment [256].

The population inversion number n_{21} as a function of the excitation rate g is displayed in Fig. 1.29b for the same set of frequencies (and with the same color coding) as in panel (a). Before the spasing threshold, n_{21} increases with g to become positive with the onset of the population inversion just before the spasing threshold. For higher g, after the spasing threshold is exceeded, the inversion n_{21} becomes constant (the inversion clamping). The clamped levels of the inversion are very low, $n_{21} \sim 0.01$, which again is due to the very strong feedback in the spaser.

The spectral width Γ_s of the spaser generation is due to the phase diffusion of the quantum SP state caused by the noise of the spontaneous emission of the SPs into the spasing mode, as described by Eq. (1.72). This width is displayed in Fig. 1.29c as a function of the pumping rate g. At the threshold, Γ_s is that of the SP line γ_n but for stronger pumping, as the SPs accumulate in the spasing mode, it decreases $\propto N_n^{-1}$, as given by Eq. (1.72). This decrease of Γ_s reflects the higher coherence of the spasing state with the increased number of SP quanta and, correspondingly, lower quantum fluctuations. As we have already mentioned, this is similar to the lasers as described by the Schawlow-Townes theory [291].

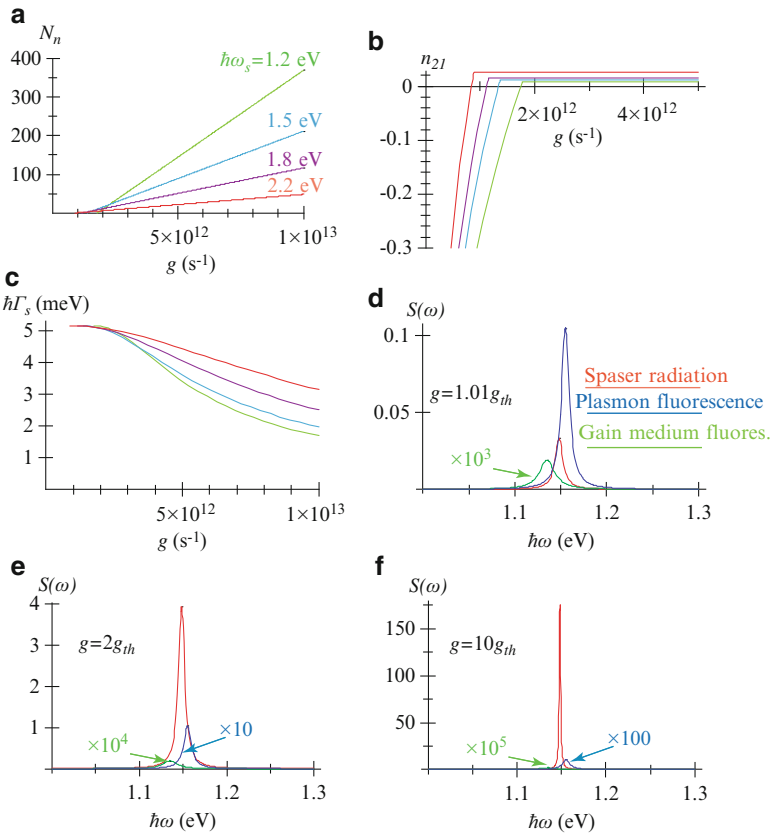

Fig. 1.29 Spaser SP population and spectral characteristics in the stationary state. The computations are done for a silver nanoshell with the external radius $R_2 = 12\,\text{nm}$; the detuning of the gain medium from the spasing SP mode is $\hbar(\omega_{21} - \omega_n) = -0.02\,\text{eV}$. The other parameters are indicated in Sect. 1.5.4. (**a**) Number N_n of plasmons per spasing mode as a function of the excitation rate g (per one chromophore of the gain medium). Computations are done for the dipole eigenmode with the spasing frequencies ω_s as indicated, which were chosen by the corresponding adjustment of the nanoshell aspect ratio. (**b**) Population inversion n_{12} as a function of the pumping rate g. The color coding of the lines is the same as in panel (**a**). (**c**) The spectral width Γ_s of the spasing line (expressed as $\hbar\Gamma_s$ in meV) as a function of the pumping rate g. The color coding of the lines is the same as in panel (**a**). (**d**)–(**f**) Spectra of the spaser for the pumping rates g expressed in the units of the threshold rate g_{th}, as indicated in the panels. The curves are color coded and scaled as indicated

The developed spasing in a dipole SP mode will show itself in the far field as an anomalously narrow and intense radiation line. The shape and intensity of this line in relation to the lines of the spontaneous fluorescence of the isolated gain medium and its SP-enhanced fluorescence line in the spaser is illustrated in Fig. 1.29d–f. Note that for the system under consideration, there is a 20 meV red shift of the gain medium fluorescence with respect to the SP line center. It is

chosen so to illustrate the spectral walk-off of the spaser line. For one percent in the excitation rate above the threshold of the spasing (panel d), a broad spasing line (red color) appears comparable in intensity to the SP-enhanced spontaneous fluorescence line (blue color). The width of this spasing line is approximately the same as of the fluorescence, but its position is shifted appreciably (spectral walk-off) toward the isolated gain medium line (green color). For the pumping twice more intense (panel e), the spaser-line radiation dominates, but its width is still close to that of the SP line due to significant quantum fluctuations of the spasing state phase. Only when the pumping rate is an order of magnitude above the threshold, the spaser line strongly narrows (panel f), and it also completely dominates the spectrum of the radiation. This is a regime of small quantum fluctuations, which is desired in applications.

These results in the spasing region are different in the most dramatic way from previous phenomenological models, which are based on linear electrodynamics where the gain medium that has negative imaginary part of its permittivity plus lossy metal nanosystem, described purely electrodynamically [262, 269]. For instance, in a "toy model" [269], the width of the resonance line tends to zero at the threshold of spasing and then broadens up again. This distinction of the present theory is due the nature of the spasing as a spontaneous symmetry breaking (nonequilibrium phase transition with a randomly established but sustained phase) leading to the establishment of a coherent SP state. This non-equilibrium phase transition to spasing and the spasing itself are contained in the present theory due to the fact that the fundamental equations of the spasing (1.67), (1.69), and (1.70) are nonlinear, as we have already discussed above in conjunction with these equations – see the text after Eq. (1.70). The previous publications on gain compensation by loss [262, 269, 271] based on linear electrodynamic equations do not contain spasing. Therefore, they are not applicable in the region of the complete loss compensation and spasing, though their results are presented for that region.

1.5.6 Spaser as Ultrafast Quantum Nanoamplifier

1.5.6.1 Problem of Setting Spaser as an Amplifier

As we have already mentioned in Sect. 1.5.1, a fundamental and formidable problem is that, in contrast to the conventional lasers and amplifiers in quantum electronics, the spaser has an inherent feedback that typically cannot be removed. Such a spaser will develop generation and accumulation of the macroscopic number of coherent SPs in the spasing mode. This leads to the population inversion clamping in the CW regime at a very low level – cf. Fig. 1.29b. This CW regime corresponds to the net amplification equal zero, which means that the gain exactly compensates the loss, which condition is expressed by Eq. (1.76). This is a consequence of the nonlinear gain saturation. This holds for any stable CW generator (including any spaser or laser) and precludes using them as amplifiers.

There are several ways to set a spaser as a quantum amplifier. One of them is to reduce the feedback, i.e., to allow some or most of the SP energy in the spaser to escape from the active region, so the spaser will not generate in the region of amplification. Such a root has successfully been employed to build a SPP plasmonic amplifier on the long-range plasmon polaritons [281]. A similar root for the SP spasers would be to allow some optical energy to escape either by a near-field coupling or by a radiative coupling to far-field radiation. The near-field coupling approach is promising for building integrated active circuits out of the spasers. Another root has been used in Ref. [292], which employed symmetric SPP modes in a thin gold strip. Such modes have much lower loss that the antisymmetric modes at the expense of much weaker confinement (transverse modal area $\sim\lambda^2$). The lower loss allows one to use the correspondingly lower gain and, therefore, avoid both spasing at localized SP modes and random lasing due to back-scattering from gold imperfections.

Following Ref. [139], we consider here two distinct approaches for setting the spasers as quantum nanoamplifiers. The first is a transient regime based on the fact that the establishment of the CW regime and the consequent inversion clamping and the total gain vanishing require some time that is determined mainly by the rate of the quantum feedback and depends also on the relaxation rates of the SPs and the gain medium. After the population inversion is created by the onset of pumping and before the spasing spontaneously develops, as we show below in this section, there is a time interval of approximately 250 fs, during which the spaser provides usable (and as predicted, quite high) amplification – see Sect. 1.5.6.2 below.

The second approach to set the spaser as a logical quantum nanoamplifier is a bistable regime that is achieved by introducing a saturable absorber into the active region, which prevents the spontaneous spasing. Then injection of a certain above-threshold amount of SP quanta will saturate the absorber and initiate the spasing. Such a bistable quantum amplifier will be considered in Sect. 1.5.6.3.

The temporal behavior of the spaser has been found by direct numerical solution of Eqs. (1.67)–(1.70). This solution is facilitated by the fact that in the model under consideration all the chromophores experience the same local field inside the nanoshell, and there are only two types of such chromophores: belonging to the gain medium and the saturable absorber, if it is present.

1.5.6.2 Monostable spaser as a Nanoamplifier in Transient Regime

Here we consider a monostable spaser in a transient regime. This implies that no saturable absorber is present. We will consider two pumping regimes: stationary and pulse.

Starting with the stationary regime, we assume that the pumping at a rate (per one chromophore) of $g = 5 \times 10^{12}\,\mathrm{s}^{-1}$ starts at a moment of time $t = 0$ and stays constant after that. Immediately at $t = 0$, a certain number of SPs are injected into the spaser. We are interested in its temporal dynamics from this moment on.

The dynamical behavior of the spaser under this pumping regime is illustrated in Figs. 1.30a, b. As we see, the spaser, which starts from an arbitrary initial population N_n, rather rapidly, within a few hundred femtoseconds approaches the same stationary ("logical") level. At this level, an SP population of $N_n = 67$ is established, while the inversion is clamped at a low level of $n_{21} = 0.02$. On the way to this stationary state, the spaser experiences relaxation oscillations in both the SP numbers and inversion, which have a trend to oscillate out of phase (compare panels (a) and (b)). This temporal dynamics of the spaser is quite complicated and highly nonlinear (unharmonic). It is controlled not by a single relaxation time but by a set of the relaxation rates. Clearly, among these are the energy transfer rate from the gain medium to the SPs and the relaxation rates of the SPs and the chromophores.

In this mode, the main effect of the initial injection of the SPs (described theoretically as different initial values of N_n) is in the interval of time it is required for the spaser to reach the final (CW) state. For very small N_n, which in practice can be supplied by the noise of the spontaneous SP emission into the mode, this time is approximately 250 fs (cf.: the corresponding SP relaxation time is less then 50 fs). In contrast, for the initial values of $N_n = 1$–5, this time shortens to 150 fs.

Now consider the second regime: pulse pumping. The gain-medium population of the spaser is inverted at $t = 0$ to saturation with a short (much shorter than 100 fs) pump pulse. Simultaneously, at $t = 0$, some number of plasmons are injected (say, by an external nanoplasmonic circuitry). In response, the spaser should produce an amplified pulse of the SP excitation. Such a function of the spaser is illustrated in Fig. 1.30c, d.

As we see from panel (c), independently from the initial number of SPs, the spaser always generates a series of SP pulses, of which only the first pulse is large (at or above the logical level of $N_n \sim 100$). (An exception is a case of little practical importance when the initial $N_n = 120$ exceeds this logical level, when two large pulses are produced.) The underlying mechanism of such a response is the rapid depletion of the inversion seen in panel (d), where energy is dissipated in the metal of the spaser. The characteristic duration of the SP pulse ~100 fs is defined by this depletion, controlled by the energy transfer and SP relaxation rates. This time is much shorter than the spontaneous decay time of the gain medium. This acceleration is due to the stimulated emission of the SPs into the spasing mode (which can be called a "stimulated Purcell effect"). There is also a pronounced trend: the lower is initial SP population N_n, the later the spaser produces the amplified pulse. In a sense, this spaser functions as a pulse-amplitude to time-delay converter.

1.5.6.3 Bistable Spaser with Saturable Absorber as an Ultrafast Nanoamplifier

Now let us consider a bistable spaser as a quantum threshold (or, logical) nanoamplifier. Such a spaser contains a saturable absorber mixed with the gain medium with parameters indicated at the end of Sect. 1.5.4.1 and the concentration of the saturable absorber $n_a = 0.66 n_c$. This case of a bistable spaser amplifier is of

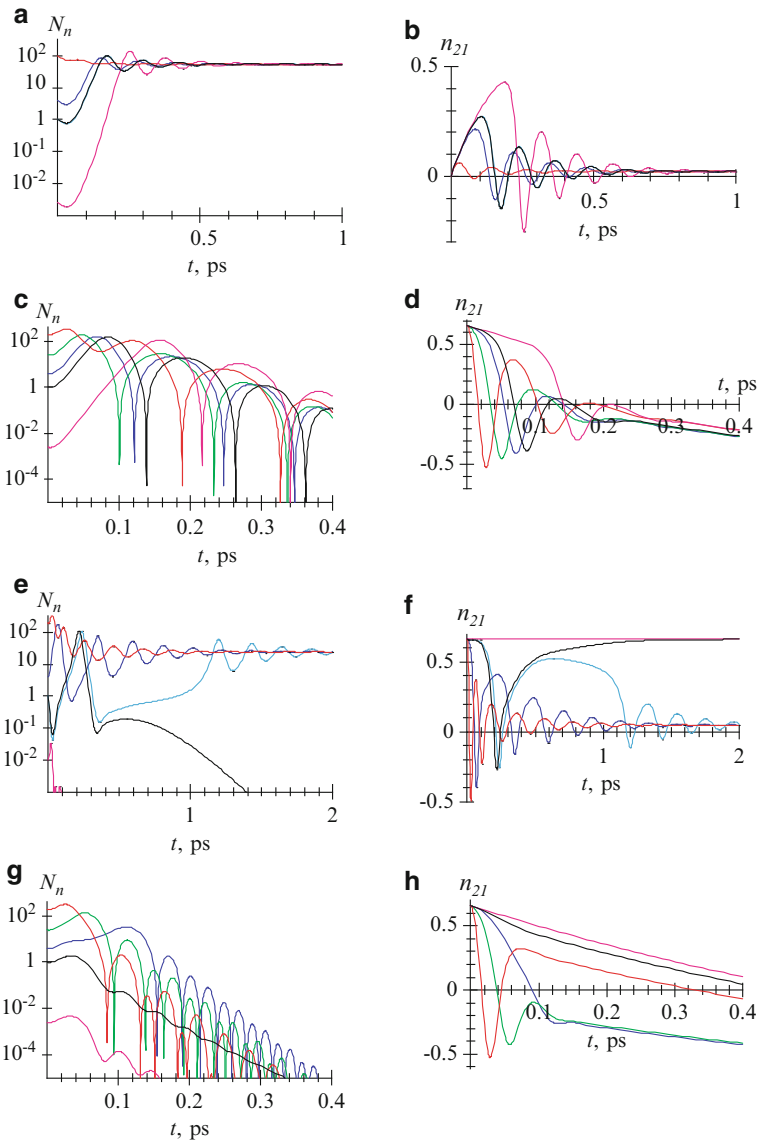

Fig. 1.30 Ultrafast dynamics of spaser. (**a**) For monostable spaser (without a saturable absorber), dependence of SP population in the spasing mode N_n on time t. The spaser is stationary pumped at a rate of $g = 5 \times 10^{12}\ \mathrm{s}^{-1}$. The color-coded curves correspond to the initial conditions with the different initial SP populations, as shown in the graphs. (**b**) The same as (**a**) but for the temporal behavior of the population inversion n_{21}. (**c**) Dynamics of a monostable spaser (no saturable absorber) with the pulse pumping described as the initial inversion $n_{21} = 0.65$. Coherent SP population N_n is displayed as a function of time t. Different initial populations are indicated by color-coded curves. (**d**) The same as (**c**) but for the corresponding population inversion n_{21}. (**e**) The same as (**a**) but for bistable spaser with the saturable absorber in concentration $n_a = 0.66 n_c$. (**f**) The same as (**b**) but for the bistable spaser. (**g**) The same as (**e**) but for the pulse pumping with the initial inversion $n_{21} = 0.65$. (**h**) The same as (**g**) but for the corresponding population inversion n_{21}

a particular interest because in this regime the spaser comes as close as possible in its functioning to the semiconductor-based (mostly, MOSFET-based) digital nanoamplifiers. As in the previous Subsection, we will consider two cases: the stationary and short-pulse pumping.

We again start with the case of the stationary pumping at a rate of $g = 5 \times 10^{12}\,\mathrm{s}^{-1}$. We show in Fig. 1.30e, f the dynamics of such a spaser. For a small initial population $N_n = 5 \times 10^{-3}$ simulating the spontaneous noise, the spaser is rapidly (faster than in 50 fs) relaxing to the zero population (panel e), while its gain-medium population is equally rapidly approaching a high level (panel f) $n_{21} = 0.65$ that is defined by the competition of the pumping and the enhanced decay into the SP mode (the purple curves). This level is so high because the spasing SP mode population vanishes and the stimulated emission is absent. After reaching this stable state (which one can call, say, "logical zero"), the spaser stays in it indefinitely long despite the continuing pumping.

In contrast, for initial values N_n of the SP population large enough (for instance, for $N_n = 5$, as shown by the blue curves in Figs. 1.30e, f), the spaser tends to the "logical one" state where the stationary SP population reaches the value of $N_n \approx 60$. Due to the relaxation oscillations, it actually exceeds this level within a short time of $\lesssim$100 fs after the seeding with the initial SPs. As the SP population N_n reaches its stationary (CW) level, the gain medium inversion n_{21} is clamped down at a low level of a few percent, as typical for the CW regime of the spaser. This "logical one" state salso persists indefinitely, as long as the inversion is supported by the pumping.

There is a critical curve (separatrix) that divide the two stable dynamics types (leading to the logical levels of zero and one). For the present set of parameters this separatrix starts with the initial population of $N_n \approx 1$. For a value of the initial N_n slightly below 1, the SP population N_n experiences a slow (hundreds fs in time) relaxation oscillation but eventually relaxes to zero (Fig. 1.30e, black curve), while the corresponding chromophore population inversion n_{21} relaxes to the high value $n_{21} = 0.65$ (panel (f), black curve). In contrast, for a value of N_n slightly higher than 1 (light blue curves in panels (e) and (f)), the dynamics is initially close to the separaratrix but eventually the initial slow dynamics tends to the high SP population and low chromophore inversion through a series of the relaxation oscillations. The dynamics close to the separatrix is characterized by a wide range of oscillation times due to its highly nonlinear character. The initial dynamics is slowest (the "decision stage" of the bistable spaser that lasts $\gtrsim$1 ps). The "decision time" is diverging infinitesimally close to the separatrix, as is characteristic of any threshold (logical) amplifier.

The gain (amplification coefficient) of the spaser as a logical amplifier is the ratio of the high CW level to the threshold level of the SP population N_n. For this specific spaser with the chosen set of parameters, this gain is $\approx$60, which is more than sufficient for the digital information processing. Thus this spaser can make a high-gain, $\sim$10 THz-bandwidth logical amplifier or dynamical memory cell with excellent prospects of applications.

The last but not the least regime to consider is that of the pulse pumping in the bistable spaser. In this case, the population inversion ($n_{21} = 0.65$) is created by a

short pulse at $t = 0$ and simultaneously initial SP population N_n is created. Both are simulated as the initial conditions in Eqs. (1.67)–(1.70). The corresponding results are displayed in Fig. 1.30g, h.

When the initial SP population exceeds the critical one of $N_n = 1$ (the blue, green, and red curves), the spaser responds with generating a short (duration less than 100 fs) pulse of the SP population (and the corresponding local fields) within a time $\lesssim$100 fs (panel g). Simultaneously, the inversion is rapidly (within $\sim$100 fs) exhausted (panel h).

In contrast, when the initial SP population N_n is less than the critical one (i.e., $N_n < 1$ in this specific case), the spaser rapidly (within a time $\lesssim$100 fs) relaxes as $N_n \to 0$ through a series of realaxation oscillations – see the black and magenta curves in Fig. 1.30g. The corresponding inversion decays in this case almost exponentially with a characteristic time $\sim$1 ps determined by the enhanced energy transfer to the SP mode in the metal – see the corresponding curves in panel (h). Note that the SP population decays faster when the spaser is above the generation threshold due to the stimulated SP emission leading to the higher local fields and enhanced relaxation.

1.5.7 Compensation of Loss by Gain and Spasing

1.5.7.1 Introduction to Loss Compensation by Gain

A problem for many applications of plasmonics and metamaterials is posed by losses inherent in the interaction of light with metals. There are several ways to bypass, mitigate, or overcome the detrimental effects of these losses, which we briefly discuss below.

(i) The most common approach consists in employing effects where the losses are not fundamentally important such as surface plasmon polariton (SPP) propagation used in sensing [23], ultramicroscopy [16, 19], and solar energy conversion [26]. For realistic losses, there are other effects and applications that are not prohibitively suppressed by the losses and useful, in particular, sensing based on SP resonances and surface enhanced Raman scattering (SERS) [23, 182, 246, 293, 294].

(ii) Another promising idea is to use superconducting plasmonics to dramatically reduce losses [74, 295–297]. However, this is only applicable for frequencies below the superconducting gaps, i.e., in the terahertz region.

(iii) Yet another proposed direction is using highly doped semiconductors where the Ohmic losses can be significantly lower due to much lower free carrier concentrations [298]. However, a problem with this approach may lie in the fact that the usefulness of plasmonic modes depends not on the loss per se but on the quality factor Q, which for doped semiconductors may not be higher than for the plasmonic metals.

(iv) One of the alternative approaches to low-loss plasmonic metamaterials is based on our idea of the spaser: it is using a gain to compensate the dielectric (Ohmic) losses [299, 300]. In this case the gain medium is included into the metamaterials. It surrounds the metal plasmonic component in the same manner as in the spasers. The idea is that the gain will provide quantum amplification compensating the loss in the metamaterials quite analogously to the spasers.

We will consider theory of the loss compensation in the plasmonic metamaterials using gain [140, 141]. Below we show that the full compensation or overcompensation of the optical loss in a dense resonant gain metamaterial leads to an instability that is resolved by its spasing (i.e., by becoming a generating spaser). We further show analytically that the conditions of the complete loss compensation by gain and the threshold condition of spasing – see Eqs. (1.83) and (1.85) – are identical. Thus the full compensation (overcompensation) of the loss by gain in such a metamaterial will cause spasing. This spasing limits (clamps) the gain – see Sect. 1.5.5 – and, consequently, inhibits the complete loss compensation (overcompensation) at any frequency.

1.5.7.2 Permittivity of Nanoplasmonic Metamaterial

We will consider, for certainty, an isotropic and uniform metamaterial that, by definition, in a range of frequencies ω can be described by the effective permittivity $\bar{\varepsilon}(\omega)$ and permeability $\bar{\mu}(\omega)$. We will concentrate below on the loss compensation for the optical electric responses; similar consideration with identical conclusions for the optical magnetic responses is straightforward. Our theory is applicable for the true three-dimensional (3d) metamaterials whose size is much greater than the wavelength λ (ideally, an infinite metamaterial).

Consider a small piece of such a metamaterial with sizes much greater that the unit cell but much smaller than λ. Such a piece is a metamaterial itself. Let us subject this metamaterial to a uniform electric field $\mathbf{E}(\omega) = -\nabla\phi(\mathbf{r}, \omega)$ oscillating with frequency ω. Note that $\mathbf{E}(\omega)$ is the amplitude of the macroscopic electric field inside the metamaterial. We will denote the local field at a point $\mathbf{r}$ inside this metamaterial as $\mathbf{e}(\mathbf{r}, \omega) = -\nabla\varphi(\mathbf{r}, \omega)$. We assume standard boundary conditions

$$\varphi(\mathbf{r}, \omega) = \phi(\mathbf{r}, \omega), \tag{1.86}$$

for $\mathbf{r}$ belonging to the surface S of the volume under consideration.

To present our results in a closed form, we first derive a homogenization formula used in Ref. [301] (see also references cited therein). By definition, the electric displacement in the volume V of the metamaterial is given by a formula

$$\mathbf{D}(\mathbf{r}, \omega) = \frac{1}{V}\int_V \varepsilon(\mathbf{r}, \omega)\mathbf{e}(\mathbf{r}, \omega)dV\ , \tag{1.87}$$

where $\varepsilon(\mathbf{r},\omega)$ is a position-dependent permittivity. This can be identically expressed (by multiplying and dividing by the conjugate of the macroscopic field E^*) and, using the Gauss theorem, transformed to a surface integral as

$$D = \frac{1}{VE^*(\omega)}\int_V \mathbf{E}^*(\omega)\varepsilon(\mathbf{r},\omega)\mathbf{e}(\mathbf{r},\omega)dV$$
$$= \frac{1}{VE^*(\omega)}\int_S \phi^*(\mathbf{r},\omega)\varepsilon(\mathbf{r},\omega)\mathbf{e}(\mathbf{r},\omega)d\mathbf{S}\,, \tag{1.88}$$

where we took into account the Maxwell continuity equation $\nabla\left[\boldsymbol{\varepsilon}(\mathbf{r},\omega)\mathbf{e}(\mathbf{r},\omega)\right] = 0$. Now, using the boundary conditions of Eq. (1.86), we can transform it back to the volume integral as

$$D = \frac{1}{VE^*(\omega)}\int_S \varphi^*(\mathbf{r})\varepsilon(\mathbf{r},\omega)\mathbf{e}(\mathbf{r},\omega)d\mathbf{S}$$
$$= \frac{1}{VE^*(\omega)}\int_V \varepsilon(\mathbf{r},\omega)\left|\mathbf{e}(\mathbf{r},\omega)\right|^2 dV\,. \tag{1.89}$$

From the last equality, we obtain the required homogenization formula as an expression for the effective permittivity of the metamaterial:

$$\bar{\varepsilon}(\omega) = \frac{1}{V\left|E(\omega)\right|^2}\int_V \varepsilon(\mathbf{r},\omega)\left|\mathbf{e}(\mathbf{r},\omega)\right|^2 dV\,. \tag{1.90}$$

1.5.7.3 Plasmonic Eigenmodes and Effective Resonant Permittivity of Metamaterials

This piece of the metamaterial with the total size $R \ll \lambda$ can be treated in the quasistatic approximation. The local field inside the nanostructured volume V of the metamaterial is given by the eigenmode expansion [78, 149, 222]

$$\mathbf{e}(\mathbf{r},\omega) = \mathbf{E}(\omega) - \sum_n \frac{a_n}{s(\omega)-s_n}\mathbf{E}_n(\mathbf{r})\,, \tag{1.91}$$
$$a_n = \mathbf{E}(\omega)\int_V \theta(\mathbf{r})\mathbf{E}_n(\mathbf{r})dV,$$

where we remind that $\mathbf{E}(\omega)$ is the macroscopic field. In the resonance, $\omega = \omega_n$, only one term at the pole of in Eq. (1.91) dominates, and it becomes

$$\mathbf{e}(\mathbf{r},\omega) = \mathbf{E}(\omega) + i\frac{a_n}{\mathrm{Im}\,s(\omega_n)}\mathbf{E}_n(\mathbf{r})\,. \tag{1.92}$$

The first term in this equation corresponds to the mean (macroscopic) field and the second one describes the deviations of the local field from the mean field containing contributions of the hot spots [159]. The mean root square ratio of the second term (local field) to the first (mean field) is estimated as

$$\sim \frac{f}{\mathrm{Im}\, s(\omega_n)} = \frac{fQ}{s_n(1-s_n)} , \tag{1.93}$$

where we took into account that, in accord with Eq. (1.34), $E_n \sim V^{-1/2}$, and

$$f = \frac{1}{V}\int_V \theta(\mathrm{r})dV , \tag{1.94}$$

where f is the metal fill factor of the system, and Q is the plasmonic quality factor. Deriving expression (1.93), we have also taken into account an equality $\mathrm{Im}\, s(\omega_n) = s_n(1-s_n)/Q$, which is valid in the assumed limit of the high quality factor, $Q \gg 1$ (see the next paragraph).

For a good plasmonic metal $Q \gg 1$ – see Fig. 1.2. For most metal-containing metamaterials, the metal fill factor is not small, typically $f \gtrsim 0.5$. Thus, keeping Eq. (1.28) in mind, it is very realistic to assume the following condition

$$\frac{fQ}{s_n(1-s_n)} \gg 1 . \tag{1.95}$$

If so, the second (local) term of the field (1.92) dominates and, with a good precision, the local field is approximately the eigenmode's field:

$$\mathbf{e}(\mathbf{r},\omega) = i\frac{a_n}{\mathrm{Im}\, s(\omega_n)}\mathbf{E}_n(\mathbf{r}) . \tag{1.96}$$

Substituting this into Eq. (1.90), we obtain a homogenization formula

$$\bar{\varepsilon}(\omega) = b_n \int_V \varepsilon(\mathbf{r},\omega)\,[\mathbf{E}_n(\mathbf{r})]^2\, dV , \tag{1.97}$$

where $b_n > 0$ is a real positive coefficient whose specific value is

$$b_n = \frac{1}{3V}\left(\frac{Q\int_V \theta(\mathbf{r})\mathbf{E}_n(\mathbf{r})dV}{s_n\,(1-s_n)}\right)^2 \tag{1.98}$$

Using Eqs. (1.97) and (1.27), (1.34), it is straightforward to show that the effective permittivity (1.97) simplifies exactly to

$$\bar{\varepsilon}(\omega) = b_n\,[s_n\varepsilon_m(\omega) + (1-s_n)\varepsilon_h(\omega)] . \tag{1.99}$$

1.5.8 Conditions of Loss Compensation by Gain and Spasing

In the case of the full inversion (maximum gain) and in the exact resonance, the host medium permittivity acquires the imaginary part describing the stimulated emission as given by the standard expression

$$\varepsilon_h(\omega) = \varepsilon_d - i\frac{4\pi}{3}\frac{|\mathbf{d}_{12}|^2 n_c}{\hbar\Gamma_{12}}\,, \tag{1.100}$$

where $\varepsilon_d = \mathrm{Re}\,\varepsilon_h$, $\mathbf{d}_{12}$ is a dipole matrix element of the gain transition in a chromophore center of the gain medium, Γ_{12} is a spectral width of this transition, and n_c is the concentration of these centers (these notations are consistent with those used above in Sects. 1.5.4.1–1.5.6.3). Note that if the inversion is not maximum, then this and subsequent equations are still applicable if one sets as the chromophore concentration n_c the inversion density: $n_c = n_2 - n_1$, where n_2 and n_1 are the concentrations of the chromophore centers of the gain medium in the upper and lower states of the gain transition, respectively.

The condition for the full electric loss compensation in the metamaterial and amplification (overcompensation) at the resonant frequency $\omega = \omega_n$ is

$$\mathrm{Im}\,\bar{\varepsilon}(\omega) \le 0 \tag{1.101}$$

Taking Eq. (1.99) into account, this reduces to

$$s_n \mathrm{Im}\,\varepsilon_m(\omega) - \frac{4\pi}{3}\frac{|\mathbf{d}_{12}|^2 n_c(1-s_n)}{\hbar\Gamma_{12}} \le 0\,. \tag{1.102}$$

Finally, taking into account Eqs. (1.28), (1.47) and that $\mathrm{Im}\,\varepsilon_m(\omega) > 0$, we obtain from Eq. (1.102) the condition of the loss (over)compensation as

$$\frac{4\pi}{3}\frac{|\mathbf{d}_{12}|^2 n_c\,[1 - \mathrm{Re}\,s(\omega)]}{\hbar\Gamma_{12}\mathrm{Re}\,s(\omega)\mathrm{Im}\,\varepsilon_m(\omega)} \ge 1\,, \tag{1.103}$$

where the strict inequality corresponds to the overcompensation and net amplification. In Eq. (1.100) we have assumed non-polarized gain transitions. If these transitions are all polarized along the excitation electric field, the concentration n_c should be multiplied by a factor of 3.

Equation (1.103) is a fundamental condition, which is precise (assuming that the requirement (1.95) is satisfied, which is very realistic for metamaterials) and general. Moreover, it is fully analytical and, actually, very simple. Remarkably, it depends only on the material characteristics and does not contain any geometric properties of the metamaterial system or the local fields. (Note that the system's geometry does affect the eigenmode frequencies and thus enters the problem implicitly.) In particular, the hot spots, which are prominent in the local fields of nanostructures [78, 159], are completely averaged out due to the integrations in Eqs. (1.90) and (1.97).

The condition (1.103) is completely non-relativistic (quasistatic) – it does not contain speed of light c, which is characteristic of also of the spaser. It is useful to express this condition also in terms of the total stimulated emission cross section $\sigma_e(\omega)$ (where ω is the central resonance frequency) of a chromophore of the gain medium as

$$\frac{c\sigma_e(\omega)\sqrt{\varepsilon_d}n_c\left[1-\mathrm{Re}\,s(\omega)\right]}{\omega\mathrm{Re}\,s(\omega)\mathrm{Im}\,\varepsilon_m(\omega)} \geq 1\,. \tag{1.104}$$

We see that Eq. (1.103) *exactly* coincides with a spasing condition expressed by Eq. (1.83). This brings us to an important conclusion: the full compensation (overcompensation) of the optical losses in a metamaterial (which is resonant and dense enough to satisfy condition (1.95)) and the spasing occur under precisely the same conditions.

We have considered above in Sect. 1.5.4.2 the conditions of spasing, which are equivalent to (1.104). These are given by one of equivalent conditions of Eqs. (1.83), (1.85), (1.103). It is also illustrated in Fig. 1.28. We stress that exactly the same conditions are for the full loss compensation (overcompensation) of a dense resonant plasmonic metamaterial with gain.

We would like also to point out that the criterion given by the equivalent conditions of Eqs. (1.83), (1.85), (1.103), or (1.104) is derived for localized SPs, which are describable in the quasistatic approximation, and is not directly applicable to the propagating plasmonic modes (SPPs). However, we expect that very localized SPPs, whose wave vector $k \lesssim l_s$, can be described by these conditions because they are, basically, quasistatic. For instance, the SPPs on a thin metal wire of a radius $R \lesssim l_s$ are described by a dispersion relation [12]

$$k \approx \frac{1}{R}\left[-\frac{\varepsilon_m}{2\varepsilon_d}\left(\ln\sqrt{-\frac{4\varepsilon_m}{\varepsilon_d}}-\gamma\right)\right]^{-1/2}\,, \tag{1.105}$$

where $\gamma \approx 0.57721$ is the Euler constant. This relation is obviously quasistatic because it does not contain speed of light c.

1.5.8.1 Discussion of Spasing and Loss Compensation by Gain

This fact of the equivalence of the full loss compensation and spasing is intimately related to the general criteria of the thermodynamic stability with respect to small fluctuations of electric and magnetic fields – see Chap. IX of Ref. [30],

$$\mathrm{Im}\,\bar{\varepsilon}(\omega) > 0\,, \quad \mathrm{Im}\,\bar{\mu}(\omega) > 0\,, \tag{1.106}$$

which must be *strict* inequalities for all frequencies for electromagnetically stable systems. For systems in thermodynamic equilibrium, these conditions are automatically satisfied.

However, for the systems with gain, the conditions (1.106) can be violated, which means that such systems can be electromagnetically unstable. The first of conditions (1.106) is opposite to Eqs. (1.101) and (1.103). This has a transparent meaning: the electrical instability of the system is resolved by its spasing.

The significance of these stability conditions for gain systems can be elucidated by the following *gedanken* experiment. Take a small isolated piece of such a metamaterial (which is a metamaterial itself). Consider that it is excited at an optical frequency ω either by a weak external optical field $\mathbf{E}$ or acquires such a field due to fluctuations (thermal or quantum). The energy density $\mathscr{E}$ of such a system is given by the Brillouin formula [30]

$$\mathscr{E} = \frac{1}{16\pi}\frac{\partial \omega \mathrm{Re}\,\bar{\varepsilon}}{\partial \omega}|\mathbf{E}|^2 \ . \tag{1.107}$$

Note that for the energy of the system to be definite, it is necessary to assume that the loss is not too large, $|\mathrm{Re}\,\bar{\varepsilon}| \gg \mathrm{Im}\,\bar{\varepsilon}$. This condition is realistic for many metamaterials, including all potentially useful ones.

The internal optical energy-density loss per unit time Q (i.e., the rate of the heat-density production in the system) is [30]

$$Q = \frac{\omega}{8\pi}\mathrm{Im}\,\bar{\varepsilon}\,|\mathbf{E}|^2 \ . \tag{1.108}$$

Assume that the internal (Ohmic) loss dominates over other loss mechanisms such as the radiative loss, which is also a realistic assumption since the Ohmic loss is very large for the experimentally studied systems and the system itself is very small (the radiative loss rate is proportional to the volume of the system). In such a case of the dominating Ohmic losses, we have $d\mathscr{E}/dt = Q$. Then Eqs. (1.107) and (1.108) can be resolved together yielding the energy $\mathscr{E}$ and electric field $|\mathbf{E}|$ of this system to evolve with time t exponentially as

$$|\mathbf{E}| \propto \sqrt{\mathscr{E}} \propto e^{-\Gamma t} \ , \quad \Gamma = \omega \mathrm{Im}\,\bar{\varepsilon} \Big/ \frac{\partial(\omega \mathrm{Re}\,\bar{\varepsilon})}{\partial \omega} \ . \tag{1.109}$$

We are interested in a resonant case when the metamaterial possesses a resonance at some eigenfrequency $\omega_n \approx \omega$. For this to be true, the system's behavior must be plasmonic, i.e., $\mathrm{Re}\,\bar{\varepsilon}(\omega) < 0$. Then the dominating contribution to $\bar{\varepsilon}$ comes from a resonant SP eigenmode n with a frequency $\omega_n \approx \omega$. In such a case, the dielectric function [78] $\bar{\varepsilon}(\omega)$ has a simple pole at $\omega = \omega_n$. As a result, $\partial\left(\omega \mathrm{Re}\,\bar{\varepsilon}\right)/\partial\omega \approx \omega \partial \mathrm{Re}\,\bar{\varepsilon}/\partial\omega$ and, consequently, $\Gamma = \gamma_n$, where γ_n is the SP decay rate given by Eqs. (1.3) or (1.48), and the metal dielectric function ε_m is replaced by the effective permittivity $\bar{\varepsilon}$ of the metamaterial. Thus, Eq. (1.109) is fully consistent with the spectral theory of SPs – see Sect. 1.3.4.

If the losses are not very large so that energy of the system is meaningful, the Kramers-Kronig causality requires [30] that $\partial(\omega \mathrm{Re}\,\bar{\varepsilon})/\partial\omega > 0$. Thus, $\mathrm{Im}\,\bar{\varepsilon} < 0$ in Eq. (1.109) would lead to a negative decrement,

$$\Gamma < 0\,, \tag{1.110}$$

implying that the initial small fluctuation starts exponentially grow in time in its field and energy, which is an instability. Such an instability is indeed not impossible: it will result in spasing that will eventually stabilize $|\mathbf{E}|$ and $\mathscr{E}$ at finite stationary (CW) levels of the spaser generation.

Note that the spasing limits (clamps) the gain and population inversion making *the net gain to be precisely zero* [139] in the stationary (continuous wave or CW) regime see Sect. 1.5.6 and Fig. 1.29b. Above the threshold of the spasing, the population inversion of the gain medium is clamped at a rather low level $n_{21} \sim 1\,\%$. The corresponding net amplification in the CW spasing regime is exactly zero, which is a condition for the CW regime. This makes the complete loss compensation and its overcompensation impossible in a dense resonant metamaterial where the feedback is created by the internal inhomogeneities (including its periodic structure) and the facets of the system.

1.5.8.2 Discussion of Published Research on Spasing and Loss Compensations

In an experimental study of the lasing spaser [264], a nanofilm of PbS quantum dots (QDs) was positioned over a two-dimensional metamaterial consisting of an array of negative split ring resonators. When the QDs were optically pumped, the system exhibited an increase of the transmitted light intensity on the background of a strong luminescence of the QDs but apparently did not reach the lasing threshold. The polarization-dependent loss compensation was only $\sim$1 %. Similarly, for an array of split ring resonators over a resonant quantum well, where the inverted electron-hole population was excited optically [302], the loss compensation did not exceed $\sim$8 %. The relatively low loss compensation in these papers may be due either to random spasing and/or spontaneous or amplified spontaneous emission enhanced by this plasmonic array, which reduces the population inversion.

A dramatic example of possible random spasing is presented in Ref. [266]. The system studied was a Kretschmann-geometry SPP setup [303] with an added $\sim$1 μm polymer film containing Rodamine 6G dye in the $n_c = 1.2 \times 10^{19}\,\mathrm{cm}^{-3}$ concentration. When the dye was pumped, there was outcoupling of radiation in a range of angles. This was a threshold phenomenon with the threshold increasing with the Kretschmann angle. At the maximum of the pumping intensity, the widest range of the outcoupling angles was observed, and the frequency spectrum at every angle narrowed to a peak near a single frequency $\hbar\omega \approx 2.1$ eV.

These observations of Ref. [266] can be explained by the spasing where the feedback is provided by roughness of the metal. At the high pumping, the localized

SPs (hots spots), which possess the highest threshold, start to spase in a narrow frequency range around the maximum of the spasing criterion – the left-hand side of Eq. (1.103). Because of the sub-wavelength size of these hot spots, the Kretschmann phase-matching condition is relaxed, and the radiation is outcoupled into a wide range of angles.

The SPPs of Ref. [266] excited by the Kretschmann coupling are short-range SPPs, very close to the antisymmetric SPPs. They are localized at subwavelength distances from the surface, and their wave length in the plane is much shorter the ω/c. Thus they can be well described by the quasistatic approximation and the present theory is applicable to them. Substituting the above-given parameters of the dye and the extinction cross section $\sigma_e = 4 \times 10^{-16}$ cm^2 into Eq. (1.104), we find that the conditions of Ref. [266] are above the threshold, supporting our assertion of the spasing. Likewise, the amplified spontaneous emission and, possibly spasing, appear to have prevented the full loss compensation in a SPP system of Ref. [278]. Note that recently, random spasing for rough surfaces surrounded by dye gain media was shown experimentally in two independent observations [285, 304].

Note that the long-range SPPs of Ref. [281] are localized significantly weaker (at distances $\sim\lambda$) than those excited in Kretschmann geometry. Thus the long-range SPPs experience a much weaker feedback, and the amplification instead of the spasing can be achieved. Generally, the long-range SPPs are fully electromagnetic (non-quasistatic) and are not describable in the present theory. Similarly, relatively weakly confined, full electromagnetic are symmetric SPP modes on thin gold strips in Ref. [292] where the amplification has been demonstrated.

As we have already discussed in conjunction with Fig. 1.28, the spasing is readily achievable with the gain medium containing common DBGSs or dyes. There have been numerous experimental observations of the spaser. Among them is a report of a SP spaser with a 7-nm gold nanosphere as its core and a laser dye in the gain medium [256], observations of the SPP spasers (also known as nanolasers) with silver as a plasmonic-core metal and DBGS as the gain medium with a 1d confinement [257, 260], a tight 2d confinement [258], and a 3d confinement [259]. There also has been a report on observation of a SPP microcylinder spaser [305]. A high efficiency room-temperature semiconductor spaser with a DBGS InGaAS gain medium operating near 1.5 μm (i.e., in the communication near-ir range) has been reported [260].

The research and development in the area of spasers (nanolasers) as quantum nano-generators is very active and will undoubtedly lead to further rapid advances. The next in line is the spaser as an ultrafast nanoamplifier, which is one of the most important tasks in nanotechnology.

In periodic metamaterials, plasmonic modes generally are propagating waves (SPPs) that satisfy Bloch theorem [306] and are characterized by quasi-wavevector $\mathbf{k}$. These are propagating waves except for the band edges where $\mathbf{ka} = \pm\pi$, where $\mathbf{a}$ is the lattice vector. At the band edges, the group velocity v_g of these modes is zero, and these modes are localized, i.e., they are SPs. Their wave function is periodic with period $2a$, which may be understood as a result of the Bragg reflection from the crystallographic planes. Within this $2a$ period, these band-edge modes can, indeed, be treated quasistatically because $2a \ll l_s, \lambda\!\!\!^{-}$. If any of the band-edge frequencies

is within the range of compensation (where the condition (1.83) [or, (1.85)] is satisfied), the system will spase. In fact, at the band edge, this metamaterial with gain is similar to a distributed feedback (DFB) laser [307]. It actually is a DFB spaser, which, as all the DFB lasers, generates in a band-edge mode.

In fact, there have recently been two observations of lasing spasers with optical pumping generating on the band–edge modes [308, 309], see also our Research Highlight in Ref. [310]. In Ref. [308], the metal component of the lasing spaser was a periodic nanohole array in a silver nanofilm, and the gain component was semiconductor diode of InGaAs/InP. In Ref. [309], the plasmonic metal component was a periodic planar array of eithet gold or silver nanoparticle while the gain medium was a polymer nanolayer composed of polyurethane and IR-140 dye.

Moreover, not only the SPPs, which are exactly at the band edge, will be localized. Due to unavoidable disorder caused by fabrication defects in metamaterials, there will be scattering of the SPPs from these defects. Close to the band edge, the group velocity becomes small, $v_g \to 0$. Because the scattering cross section of any wave is $\propto v_g^{-2}$, the corresponding SPPs experience Anderson localization [311]. Also, there always will be SPs nanolocalized at the defects of the metamaterial, whose local fields are hot spots – see Fig. 1.10 and, generally, Sect. 1.3.5 and the publications referenced therein. Each of such hot spots within the bandwidth of conditions (1.83) or (1.85) will be a generating spaser, which clamps the inversion and precludes the full loss compensation.

Acknowledgements The primary support for this work was provided by MURI Grant No. N00014-13-1-0649 from the U.S. Office of Navy Research. Additional support was provided by Grant No. DE-FG02-11ER46789 from the Materials Sciences and Engineering Division, Office of the Basic Energy Sciences, Office of Science, U.S. Department of Energy, and Grant No. DE-FG02-01ER15213 from the Chemical Sciences, Biosciences and Geosciences Division, Office of the Basic Energy Sciences, Office of Science, U.S. Department of Energy.

References

1. Moskovits M (1985) Surface-enhanced spectroscopy. Rev Mod Phys 57:783–826
2. Stockman MI, Shalaev VM, Moskovits M, Botet R, George TF (1992) Enhanced Raman scattering by fractal clusters: scale invariant theory. Phys Rev B 46:2821–2830
3. Gunnarsson L, Petronis S, Kasemo B, Xu H, Bjerneld J, Kall M (1999) Optimizing nanofabricated substrates for surface enhanced Raman scattering. Nanostruct Mater 12:783–788
4. Xu HX, Bjerneld EJ, Kall M, Borjesson L (1999) Spectroscopy of single hemoglobin molecules by surface enhanced Raman scattering. Phys Rev Lett 83:4357–4360
5. Xu H, Aizpurua J, Kall M, Apell P (2000) Electromagnetic contributions to single-molecule sensitivity in surface-enhanced Raman scattering. Phys Rev E 62:4318–4324
6. Kneipp K, Moskovits M, Kneipp H (eds) (2006) Electromagnetic theory of SERS, vol 103. Springer, Heidelberg
7. Ebbesen TW, Lezec HJ, Ghaemi HF, Thio T, Wolff PA (1998) Extraordinary optical transmission through sub-wavelength hole arrays. Nature 391:667–669
8. Lezec HJ, Degiron A, Devaux E, Linke RA, Martin-Moreno L, Garcia-Vidal FJ, Ebbesen TW (2002) Beaming light from a subwavelength aperture. Science 297:820–822

9. Martin-Moreno L, Garcia-Vidal FJ, Lezec HJ, Degiron A, Ebbesen TW (2003) Theory of highly directional emission from a single subwavelength aperture surrounded by surface corrugations. Phys Rev Lett 90:167401–1–4
10. Genet C, Ebbesen TW (2007) Light in tiny holes. Nature 445:39–46
11. Garcia-Vidal FJ, Martin-Moreno L, Ebbesen TW, Kuipers L (2010) Light passing through subwavelength apertures. Rev Mod Phys 82:729–787
12. Stockman MI (2004) Nanofocusing of optical energy in tapered plasmonic waveguides. Phys Rev Lett 93:137404–1–4
13. Verhagen E, Polman A, Kuipers L (2008) Nanofocusing in laterally tapered plasmonic waveguides. Opt Express 16:45–57
14. Verhagen E, Spasenovic M, Polman A, Kuipers L (2009) Nanowire plasmon excitation by adiabatic mode transformation. Phys Rev Lett 102:203904–1–4
15. De Angelis F, Patrini M, Das G, Maksymov I, Galli M, Businaro L, Andreani LC, Di Fabrizio E (2008) A hybrid plasmonic-photonic nanodevice for label-free detection of a few molecules. Nano Lett 8:2321–2327
16. De Angelis F, Das G, Candeloro P, Patrini M, Galli M, Bek A, Lazzarino M, Maksymov I, Liberale C, Andreani LC, Di Fabrizio E (2009) Nanoscale chemical mapping using three-dimensional adiabatic compression of surface plasmon polaritons. Nat Nanotechnol 5:67–72
17. Angelis FD, Gentile F, Das FMG, Moretti M, Candeloro P, Coluccio ML, Cojoc G, Accardo A, Liberale C, Zaccaria RP, Perozziello G, Tirinato L, Toma A, Cuda G, Cingolani R, Di Fabrizio E (2011) Breaking the diffusion limit with super-hydrophobic delivery of molecules to plasmonic nanofocusing SERS structures. Nat Photonics 5:682–687
18. Ropers C, Neacsu CC, Elsaesser T, Albrecht M, Raschke MB, Lienau C (2007) Grating-coupling of surface plasmons onto metallic tips: a nano-confined light source. Nano Lett 7:2784–2788
19. Neacsu CC, Berweger S, Olmon RL, Saraf LV, Ropers C, Raschke MB (2010) Near-field localization in plasmonic superfocusing: a nanoemitter on a tip. Nano Lett 10:592–596
20. Raschke MB, Berweger S, Atkin JM, Olmon RL (2010) Adiabatic tip-plasmon focusing for nano-Raman spectroscopy. J Phys Chem Lett 1:3427–3432
21. Berweger S, Atkin JM, Xu XG, Olmon RL, Raschke MB (2011) Femtosecond nanofocusing with full optical waveform control. Nano Lett 11:4309–4313
22. Sadiq D, Shirdel J, Lee JS, Selishcheva E, Park N, Lienau C (2011) Adiabatic nanofocusing scattering-type optical nanoscopy of individual gold nanoparticles. Nano Lett 11:1609–1613
23. Stockman MI (2011) Nanoplasmonics: the physics behind the applications. Phys Today 64:39–44
24. Lal S, Clare SE, Halas NJ (2008) Nanoshell-enabled photothermal cancer therapy: impending clinical impact. Acc Chem Res 41:1842–1851
25. Huang XH, Neretina S, El-Sayed MA (2009) Gold nanorods: from synthesis and properties to biological and biomedical applications. Adv Mater 21:4880–4910
26. Atwater HA, Polman A (2010) Plasmonics for improved photovoltaic devices. Nat Mater 9:205–213
27. Mukherjee S, Libisch F, Large N, Neumann O, Brown LV, Cheng J, Lassiter JB, Carter EA, Nordlander P, Halas NJ (2012) Hot electrons do the impossible: plasmon-induced dissociation of H_2 on Au. Nano Lett 13:240–247
28. Mubeen S, Lee J, Singh N, Kramer S, Stucky GD, Moskovits M (2013) An autonomous photosynthetic device in which all charge carriers derive from surface plasmons. Nat Nano 8:247–251
29. Bergman DJ, Stroud D (1992) Properties of macroscopically inhomogeneous media. In: Ehrenreich H, Turnbull D (eds) Solid state physics, vol 46. Academic, Boston, pp 148–270
30. Landau LD, Lifshitz EM (1984) Electrodynamics of continuous media. Pergamon, Oxford/New York
31. Bergman DJ, Stockman MI (2003) Surface plasmon amplification by stimulated emission of radiation: quantum generation of coherent surface plasmons in nanosystems. Phys Rev Lett 90:027402–1–4

32. Johnson PB, Christy RW (1972) Optical constants of noble metals. Phys Rev B 6:4370–4379
33. Feigenbaum E, Orenstein M (2008) Ultrasmall volume plasmons, yet with complete retardation effects. Phys Rev Lett 101:163902–1–4
34. Larkin IA, Stockman MI, Achermann M, Klimov VI (2004) Dipolar emitters at nanoscale proximity of metal surfaces: giant enhancement of relaxation in microscopic theory. Phys Rev B 69:121403(R)–1–4
35. Larkin IA, Stockman MI (2005) Imperfect perfect lens. Nano Lett 5:339–343
36. Bozhevolny SI (ed) (2008) Plasmonic nanoguides and circuits. World Scientific, Singapore
37. Kramer A, Keilmann F, Knoll B, Guckenberger R (1996) The coaxial tip as a nano-antenna for scanning near-field microwave transmission microscopy. Micron 27:413–417
38. Oldenburg SJ, Hale GD, Jackson JB, Halas NJ (1999) Light scattering from dipole and quadrupole nanoshell antennas. Appl Phys Lett 75:1063–1065
39. Kalkbrenner T, Hkanson U, Schadle A, Burger S, Henkel C, Sandoghdar V (2005) Optical microscopy via spectral modifications of a nanoantenna. Phys Rev Lett 95:200801–1–4
40. Muhlschlegel P, Eisler HJ, Martin OJF, Hecht B, Pohl DW (2005) Resonant optical antennas. Science 308:1607–1609
41. Schuck PJ, Fromm DP, Sundaramurthy A, Kino GS, Moerner WE (2005) Improving the mismatch between light and nanoscale objects with gold bowtie nanoantennas. Phys Rev Lett 94:017402–1–4
42. Kuhn S, Hakanson U, Rogobete L, Sandoghdar V (2006) Enhancement of single-molecule fluorescence using a gold nanoparticle as an optical nanoantenna. Phys Rev Lett 97:017402–1–4
43. Novotny L (2007) Effective wavelength scaling for optical antennas. Phys Rev Lett 98:266802–1–4
44. Taminiau TH, Segerink FB, Moerland RJ, Kuipers L, van Hulst NF (2007) Near-field driving of a optical monopole antenna. J Opt A 9:S315–S321
45. Taminiau TH, Segerink FB, van Hulst NF (2007) A monopole antenna at optical frequencies: single-molecule near-field measurements. IEEE Trans Antennas Propag 55:3010–3017
46. Behr N, Raschke MB (2008) Optical antenna properties of scanning probe tips: plasmonic light scattering, tip-sample coupling, near-field enhancement. J Phys Chem C 112:3766–3773
47. Bryant GW, de Abajo FJG, Aizpurua J (2008) Mapping the plasmon resonances of metallic nanoantennas. Nano Lett 8:631–636
48. Ghenuche P, Cherukulappurath S, Taminiau TH, van Hulst NF, Quidant R (2008) Spectroscopic mode mapping of resonant plasmon nanoantennas. Phys Rev Lett 101:116805–1–4
49. Guo HC, Meyrath TP, Zentgraf T, Liu N, Fu LW, Schweizer H, Giessen H (2008) Optical resonances of bowtie slot antennas and their geometry and material dependence. Opt Express 16:7756–7766
50. Bakker RM, Yuan HK, Liu ZT, Drachev VP, Kildishev AV, Shalaev VM, Pedersen RH, Gresillon S, Boltasseva A (2008) Enhanced localized fluorescence in plasmonic nanoantennae. Appl Phys Lett 92:043101–1–3
51. Olmon RL, Krenz PM, Jones AC, Boreman GD, Raschke MB (2008) Near-field imaging of optical antenna modes in the mid-infrared. Opt Express 16:20295–20305
52. Taminiau TH, Stefani FD, Segerink FB, Hulst NFV (2008) Optical antennas direct single-molecule emission. Nat Photonics 2:234–237
53. Tang L, Kocabas SE, Latif S, Okyay AK, Ly-Gagnon DS, Saraswat KC, Miller DAB (2008) Nanometre-scale germanium photodetector enhanced by a near-infrared dipole antenna. Nat Photonics 2:226–229
54. Bharadwaj P, Deutsch B, Novotny L (2009) Optical antennas. Adv Opt Photonics 1:438–483
55. Eghlidi H, Lee KG, Chen XW, Gotzinger S, Sandoghdar V (2009) Resolution and enhancement in nanoantenna-based fluorescence microscopy. Nano Lett 9:4007–4011
56. Hanke T, Krauss G, Trauetlein D, Wild B, Bratschitsch R, Leitenstorfer A (2009) Efficient nonlinear light emission of single gold optical antennas driven by few-cycle near-infrared pulses. Phys Rev Lett 103:257404–1–4

57. Palomba S, Danckwerts M, Novotny L (2009) Nonlinear plasmonics with gold nanoparticle antennas. J Opt A 11:114030
58. Cao LY, Park JS, Fan PY, Clemens B, Brongersma ML (2010) Resonant germanium nanoantenna photodetectors. Nano Lett 10:1229–1233
59. Giannini V, Vecchi G, Rivas JG (2010) Lighting up multipolar surface plasmon polaritons by collective resonances in arrays of nanoantennas. Phys Rev Lett 105:266801–1–4
60. Weber-Bargioni A, Schwartzberg A, Schmidt M, Harteneck B, Ogletree DF, Schuck PJ, Cabrini S (2010) Functional plasmonic antenna scanning probes fabricated by induced-deposition mask lithography. Nanotechnology 21:065306–1–6
61. Knight MW, Sobhani H, Nordlander P, Halas NJ (2011) Photodetection with active optical antennas. Science 332:702–704
62. Li W-D, Ding F, Hu J, Chou SY (2011) Three-dimensional cavity nanoantenna coupled plasmonic nanodots for ultrahigh and uniform surface-enhanced Raman scattering over large area. Opt Express 19:3925–3936
63. Liu N, Tang ML, Hentschel M, Giessen H, Alivisatos AP (2011) Nanoantenna-enhanced gas sensing in a single tailored nanofocus. Nat Mater 10:631–636
64. Maksymov IS, Miroshnichenko AE (2011) Active control over nanofocusing with nanorod plasmonic antennas. Opt Express 19:5888–5894
65. Novotny L, van Hulst N (2011) Antennas for light. Nat Photonics 5:83–90
66. Schnell M, Gonzalez PA, Arzubiaga L, Casanova F, Hueso LE, Chuvilin A, Hillenbrand R (2011) Nanofocusing of mid-infrared energy with tapered transmission lines. Nat Photonics 5:283–287
67. Berestetskii VB, Lifshits EM, Pitaevskii LP (1982) Quantum electrodynamics. Pergamon, Oxford/New York
68. Fano U (1935) On the absorption spectrum of noble gases at the arc spectrum limit. Nuovo Cimento 12:154–161
69. Fedotov VA, Rose M, Prosvirnin SL, Papasimakis N, Zheludev NI (2007) Sharp trapped-mode resonances in planar metamaterials with a broken structural symmetry. Phys Rev Lett 99:147401–1–4
70. Hao F, Sonnefraud Y, Dorpe PV, Maier SA, Halas NJ, Nordlander P (2008) Symmetry breaking in plasmonic nanocavities: subradiant LSPR sensing and a tunable Fano resonance. Nano Lett 8:3983–3988
71. Mirin NA, Bao K, Nordlander P (2009) Fano resonances in plasmonic nanoparticle aggregates. J Phys Chem A 113:4028–4034
72. Brown LV, Sobhani H, Lassiter JB, Nordlander P, Halas NJ (2010) Heterodimers: plasmonic properties of mismatched nanoparticle pairs. ACS Nano 4:819–832
73. Fan JA, Wu CH, Bao K, Bao JM, Bardhan R, Halas NJ, Manoharan VN, Nordlander P, Shvets G, Capasso F (2010) Self-assembled plasmonic nanoparticle clusters. Science 328:1135–1138
74. Fedotov VA, Tsiatmas A, Shi JH, Buckingham R, de Groot P, Chen Y, Wang S, Zheludev NI (2010) Temperature control of Fano resonances and transmission in superconducting metamaterials. Opt Express 18:9015–9019
75. Hentschel M, Saliba M, Vogelgesang R, Giessen H, Alivisatos AP, Liu N (2010) Transition from isolated to collective modes in plasmonic oligomers. Nano Lett 10:2721–2726
76. Luk'yanchuk B, Zheludev NI, Maier SA, Halas NJ, Nordlander P, Giessen H, Chong CT (2010) The Fano resonance in plasmonic nanostructures and metamaterials. Nat Mater 9:707–715
77. Stockman MI (2010) Dark-hot resonances. Nature 467:541–542
78. Stockman MI, Faleev SV, Bergman DJ (2001) Localization versus delocalization of surface plasmons in nanosystems: can one state have both characteristics? Phys Rev Lett 87:167401–1–4
79. Novotny L (2001) Forces in optical near-fields. In: Kawata S, Ohtsu M, Irie M (eds) Near-field optics and surface plasmon polaritons, vol 81. Springer, Berlin, pp 123–141

80. Ignatovich FV, Novotny L (2003) Experimental study of nanoparticle detection by optical gradient forces. Rev Sci Instrum 74:5231–5235
81. Joulain K, Mulet J-P, Marquier F, Carminati R, Greffet J-J (2005) Surface electromagnetic waves thermally excited: radiative heat transfer, coherence properties and Casimir forces revisited in the near field. Surf Sci Rep 57:59–112
82. Li XT, Bergman DJ, Stroud D (2005) Electric forces among nanospheres in a dielectric host. Europhys Lett 69:1010–1016
83. Volpe G, Quidant R, Badenes G, Petrov D (2006) Surface plasmon radiation forces. Phys Rev Lett 96:238101
84. Zelenina AS, Quidant R, Nieto-Vesperinas M (2007) Enhanced optical forces between coupled resonant metal nanoparticles. Opt Lett 32:1156–1158
85. Takuya I, Hajime I (2008) Theory of resonant radiation force exerted on nanostructures by optical excitation of their quantum states: from microscopic to macroscopic descriptions. Phys Rev B 77:245319–1–16
86. Quidant R, Zelenina S, Nieto-Vesperinas M (2007) Optical manipulation of plasmonic nanoparticles. Appl Phys A 89:233–239
87. Righini M, Zelenina AS, Girard C, Quidant R (2007) Parallel and selective trapping in a patterned plasmonic landscape. Nat Phys 3:477–480
88. Quidant R, Girard C (2008) Surface-plasmon-based optical manipulation. Laser Photonics Rev 2:47–57
89. Righini M, Volpe G, Girard C, Petrov D, Quidant R (2008) Surface plasmon optical tweezers: tunable optical manipulation in the femtonewton range. Phys Rev Lett 100:186804–1–4
90. Juan ML, Gordon R, Pang YJ, Eftekhari F, Quidant R (2009) Self-induced back-action optical trapping of dielectric nanoparticles. Nat Phys 5:915–919
91. Righini M, Ghenuche P, Cherukulappurath S, Myroshnychenko V, de Abajo FJG, Quidant R (2009) Nano-optical trapping of Rayleigh particles and Escherichia coli bacteria with resonant optical antennas. Nano Lett 9:3387–3391
92. Tong LM, Righini M, Gonzalez MU, Quidant R, Kall M (2009) Optical aggregation of metal nanoparticles in a microfluidic channel for surface-enhanced Raman scattering analysis. Lab Chip 9:193–195
93. Durach M, Rusina A, Stockman MI (2009) Giant surface-plasmon-induced drag effect in metal nanowires. Phys Rev Lett 103:186801–1–4
94. Ritchie RH (1957) Plasma losses by fast electrons in thin films. Phys Rev 106:874–881
95. Blackstock AW, Ritchie RH, Birkhoff RD (1955) Mean free path for discrete electron energy losses in metallic foils. Phys Rev 100:1078
96. Swanson N, Powell CJ (1966) Inelastic scattering cross sections for 20-keV electrons in Al, Be, polystyrene. Phys Rev 145:195
97. de Abajo FJG (2010) Optical excitations in electron microscopy. Rev Mod Phys 82:209
98. Reyes-Coronado A, Barrera RG, Batson PE, Echenique PM, Rivacoba A, Aizpurua J (2010) Electromagnetic forces on plasmonic nanoparticles induced by fast electron beams. Phys Rev B 82:235429–1–19
99. Dasgupta BB, Fuchs R (1981) Polarizability of a small sphere including nonlocal effects. Phys Rev B 24:554–561
100. Pendry JB (2000) Negative refraction makes a perfect lens. Phys Rev Lett 85:3966–3969
101. de Abajo FJG (2008) Nonlocal effects in the plasmons of strongly interacting nanoparticles, dimers, and waveguides. J Phys Chem C 112:17983–17987
102. Kreibig U, Vollmer M (1995) Optical properties of metal clusters. Springer, New York
103. Pustovit VN, Shahbazyan TV (2005) Quantum-size effects in SERS from noble-metal nanoparticles. Microelectron J 36:559–563
104. Pustovit VN, Shahbazyan TV (2006) Finite-size effects in surface-enhanced Raman scattering in noble-metal nanoparticles: a semiclassical approach. J Opt Soc Am A 23:1369–1374
105. Pustovit VN, Shahbazyan TV (2006) Surface-enhanced Raman scattering on the nanoscale: a microscopic approach. J Opt A 8:S208–S212

106. Pustovit VN, Shahbazyan TV (2006) SERS from molecules adsorbed on small Ag nanoparticles: a microscopic model. Chem Phys Lett 420:469–473
107. Pustovit VN, Shahbazyan TV (2006) Microscopic theory of surface-enhanced Raman scattering in noble-metal nanoparticles. Phys Rev B 73:085408–1–7
108. Zuloaga J, Prodan E, Nordlander P (2009) Quantum description of the plasmon resonances of a nanoparticle dimer. Nano Lett 9:887–891
109. Nordlander P, Zuloaga J, Prodan E (2010) Quantum plasmonics: optical properties and tunability of metallic nanorods. ACS Nano 4:5269–5276
110. Palik ED (1998) Handbook of optical constants of solids. Academic, San Diego
111. Chang DE, Sorensen AS, Hemmer PR, Lukin MD (2006) Quantum optics with surface plasmons. Phys Rev Lett 97:053002–1–4
112. Akimov AV, Mukherjee A, Yu CL, Chang DE, Zibrov AS, Hemmer PR, Park H, Lukin MD (2007) Generation of single optical plasmons in metallic nanowires coupled to quantum dots. Nature 450:402–406
113. Berini P, Akbari A, Tait RN (2010) Surface plasmon waveguide Schottky detector. Opt Express 18:8505–8514
114. Scales C, Breukelaar I, Berini P (2010) Surface-plasmon Schottky contact detector based on a symmetric metal stripe in silicon. Opt Lett 35:529–531
115. Levy U, Goykhman I, Desiatov B, Khurgin J, Shappir J (2011) Locally oxidized silicon surface-plasmon Schottky detector for telecom regime. Nano Lett 11:2219–2224
116. Sze SM (2007) Physics of semiconductor devices. Wiley-Interscience, Hoboken
117. Butenko AV, Shalaev VM, Stockman MI (1988) Giant impurity nonlinearities in optics of fractal clusters. Sov Phys JETP 67:60–69
118. Karpov AV, Popov AK, Rautian SG, Safonov VP, Slabko VV, Shalaev VM, Stockman MI (1988) Observation of a wavelength- and polarization-selective photomodification of silver clusters. JETP Lett 48:571–573
119. Rautian SG, Safonov VP, Chubakov PA, Shalaev VM, Stockman MI (1988) Surface-enhanced parametric scattering of light by silver clusters. JETP Lett 47:243–246
120. Shalaev VM, Stockman MI, Botet R (1992) Resonant excitations and nonlinear optics of fractals. Physica A 185:181–186
121. Boyd RW (2003) Nonlinear optics. Academic, London/San Diego
122. Kneipp J, Kneipp H, Kneipp K (2006) Two-photon vibrational spectroscopy for biosciences based on surface-enhanced hyper-Raman scattering. Proc Natl Acad Sci U S A 103:17149–17153
123. Kubo A, Onda K, Petek H, Sun Z, Jung YS, Kim HK (2005) Femtosecond imaging of surface plasmon dynamics in a nanostructured silver film. Nano Lett 5:1123–1127
124. Zayats AV, Smolyaninov II, Davis CC (1999) Observation of localized plasmonic excitations in thin metal films with near-field second-harmonic microscopy. Opt Commun 169:93–96
125. Bouhelier A, Beversluis M, Hartschuh A, Novotny L (2003) Near-field second-harmonic generation induced by local field enhancement. Phys Rev Lett 90:13903–1–4
126. Bozhevolnyi SI, Beermann J, Coello V (2003) Direct observation of localized second-harmonic enhancement in random metal nanostructures. Phys Rev Lett 90:197403–1–4
127. Labardi M, Allegrini M, Zavelani-Rossi M, Polli D, Cerullo G, Silvestri SD, Svelto O (2004) Highly efficient second-harmonic nanosource for near-field optics and microscopy. Opt Lett 29:62–64
128. Stockman MI, Bergman DJ, Anceau C, Brasselet S, Zyss J (2004) Enhanced second-harmonic generation by metal surfaces with nanoscale roughness: nanoscale dephasing, depolarization, and correlations. Phys Rev Lett 92:057402–1–4
129. Zheludev NI, Emelyanov VI (2004) Phase matched second harmonic generation from nanostructured metal surfaces. J Opt A 6:26–28
130. Jin RC, Jureller JE, Kim HY, Scherer NF (2005) Correlating second harmonic optical responses of single Ag nanoparticles with morphology. J Am Chem Soc 127:12482–12483

131. Canfield BK, Husu H, Laukkanen J, Bai BF, Kuittinen M, Turunen J, Kauranen M (2007) Local field asymmetry drives second-harmonic generation in noncentrosymmetric nanodimers. Nano Lett 7:1251–1255
132. Zdanowicz M, Kujala S, Husu H, Kauranen M (2011) Effective medium multipolar tensor analysis of second-harmonic generation from metal nanoparticles. New J Phys 13:023025–1–12
133. Renger J, Quidant R, van Hulst N, Novotny L (2010) Surface-enhanced nonlinear four-wave mixing. Phys Rev Lett 104:046803–1–4
134. Utikal T, Stockman MI, Heberle AP, Lippitz M, Giessen H (2010) All-optical control of the ultrafast dynamics of a hybrid plasmonic system. Phys Rev Lett 104:113903–1–4
135. Pacifici D, Lezec HJ, Atwater HA (2007) All-optical modulation by plasmonic excitation of CdSe quantum dots. Nat Photonics 1:402–406
136. Samson ZL, MacDonald KF, De Angelis F, Gholipour B, Knight K, Huang CC, Di Fabrizio E, Hewak DW, Zheludev NI (2010) Metamaterial electro-optic switch of nanoscale thickness. Appl Phys Lett 96:143105–1–3
137. MacDonald KF, Samson ZL, Stockman MI, Zheludev NI (2009) Ultrafast active plasmonics. Nat Photonics 3:55–58
138. Kim S, Jin JH, Kim YJ, Park IY, Kim Y, Kim SW (2008) High-harmonic generation by resonant plasmon field enhancement. Nature 453:757–760
139. Stockman MI (2010) The spaser as a nanoscale quantum generator and ultrafast amplifier. J Opt 12:024004–1–13
140. Stockman MI (2011) Spaser action, loss compensation, stability in plasmonic systems with gain. Phys Rev Lett 106:156802–1–4
141. Stockman MI (2011) Loss compensation by gain and spasing. Philos Trans R Soc A 369:3510–3524
142. Ginzburg P, Hayat A, Berkovitch N, Orenstein M (2010) Nonlocal ponderomotive nonlinearity in plasmonics. Opt Lett 35:1551–1553
143. Feigenbaum E, Orenstein M (2007) Plasmon-soliton. Opt Lett 32:674–676
144. Zherebtsov S, Fennel T, Plenge J, Antonsson E, Znakovskaya I, Wirth A, Herrwerth O, Suessmann F, Peltz C, Ahmad I, Trushin SA, Pervak V, Karsch S, Vrakking MJJ, Langer B, Graf C, Stockman MI, Krausz F, Ruehl E, Kling MF (2011) Controlled near-field enhanced electron acceleration from dielectric nanospheres with intense few-cycle laser fields. Nat Phys 7:656–662
145. Kruger M, Schenk M, Hommelhoff P (2011) Attosecond control of electrons emitted from a nanoscale metal tip. Nature 475:78–81
146. Durach M, Rusina A, Kling MF, Stockman MI (2010) Metallization of nanofilms in strong adiabatic electric fields. Phys Rev Lett 105:086803–1–4
147. Durach M, Rusina A, Kling MF, Stockman MI (2011) Predicted ultrafast dynamic metallization of dielectric nanofilms by strong single-cycle optical fields. Phys Rev Lett 107:086602–1–5
148. Bergman DJ, Stroud D (1992) Properties of macroscopically inhomogeneous media. In: Ehrenreich H, Turnbull D (eds) Solid state physics, vol 46. Academic, Boston, pp 148–270
149. Stockman MI, Bergman DJ, Kobayashi T (2004) Coherent control of nanoscale localization of ultrafast optical excitation in nanosystems. Phys Rev B 69:054202–1–10
150. Shalaev VM, Stockman MI (1987) Optical properties of fractal clusters (susceptibility, surface enhanced Raman scattering by impurities). Sov Phys JETP 65:287–294
151. Shalaev VM, Botet R, Butenko AV (1993) Localization of collective dipole excitations on fractals. Phys Rev B 48:6662–6664
152. Shalaev VM, Botet R, Tsai DP, Kovacs J, Moskovits M (1994) Fractals – localization of dipole excitations and giant optical polarizabilities. Physica A 207:197–207
153. Sarychev AK, Shubin VA, Shalaev VM (2000) Anderson localization of surface plasmons and Kerr nonlinearity in semicontinuous metal films. Physica B 279:87–89

154. Bozhevolnyi SI, Markel VA, Coello V, Kim W, Shalaev VM (1998) Direct observation of localized dipolar excitations on rough nanostructured surfaces. Phys Rev B 58:11441–11448
155. Sarychev AK, Shubin VA, Shalaev VM (1999) Anderson localization of surface plasmons and nonlinear optics of metal-dielectric composites. Phys Rev B 60:16389–16408
156. Gresillon S, Aigouy L, Boccara AC, Rivoal JC, Quelin X, Desmarest C, Gadenne P, Shubin VA, Sarychev AK, Shalaev VM (1999) Experimental observation of localized optical excitations in random metal-dielectric films. Phys Rev Lett 82:4520–4523
157. Shalaev VM (2000) Nonlinear optics of random media: fractal composites and metal-dielectric films. Springer, Berlin/New York
158. Stockman MI (1997) Inhomogeneous eigenmode localization, chaos, and correlations in large disordered clusters. Phys Rev E 56:6494–6507
159. Stockman MI, Pandey LN, George TF (1996) Inhomogeneous localization of polar eigenmodes in fractals. Phys Rev B 53:2183–2186
160. Stockman MI (1997) Chaos and spatial correlations for dipolar eigenproblems. Phys Rev Lett 79:4562–4565
161. Stockman MI (2000) Giant attosecond fluctuations of local optical fields in disordered nanostructured media. Phys Rev B 62:10494–10497
162. Krachmalnicoff V, Castanie E, Wilde YD, Carminati R (2010) Fluctuations of the local density of states probe localized surface plasmons on disordered metal films. Phys Rev Lett 105:183901–1–4
163. Tsai DP, Kovacs J, Wang Z, Moskovits M, Shalaev VM, Suh JS, Botet R (1994) Photon scanning tunneling microscopy images of optical excitations of fractal metal colloid clusters. Phys Rev Lett 72:4149–4152
164. Stockman MI, Pandey LN, Muratov LS, George TF (1995) Photon scanning-tunneling-microscopy images of optical-excitations of fractal metal colloid clusters – comment. Phys Rev Lett 75:2450
165. Negro LD, Boriskina SV (2012) Deterministic aperiodic nanostructures for photonics and plasmonics applications. Laser Photonics Rev 6:178–218
166. Kolb M, Botet R, Julienne J (1983) Scaling of kinetically growing clusters. Phys Rev Lett 51:1123–1126
167. Weitz DA, Oliveria M (1984) Fractal structures formed by kinetic aggregation of aqueous gold colloids. Phys Rev Lett 52:1433–1436
168. Westcott SL, Halas NJ (2002) Electron relaxation dynamics in semicontinuous metal films on nanoparticle surfaces. Chem Phys Lett 356:207–213
169. Seal K, Sarychev AK, Noh H, Genov DA, Yamilov A, Shalaev VM, Ying ZC, Cao H (2005) Near-field intensity correlations in semicontinuous metal-dielectric films. Phys Rev Lett 94:226101–1–4
170. Stockman MI (2005) Giant fluctuations of second harmonic generation on nanostructured surfaces. Chem Phys 318:156–162
171. Fort E, Gresillon S (2008) Surface enhanced fluorescence. J Phys D 41:013001–1–31
172. Efros AL (1986) Physics and geometry of disorder: percolation theory. Mir, Moscow
173. Levitov LS (1990) Delocalization of vibrational modes caused by electric dipole interaction. Phys Rev Lett 64:547–550
174. Parshin DA, Schober HR (1998) Multifractal structure of eigenstates in the Anderson model with long-range off-diagonal disorder. Phys Rev B 57:10232–10235
175. Burin AL, Kagan Y, Maksimov LA, Polischuk IY (1998) Dephasing rate in dielectric glasses at ultralow temperatures. Phys Rev Lett 80:2945–2948
176. Stockman MI, Pandey LN, Muratov LS, George TF (1994) Giant fluctuations of local optical fields in fractal clusters. Phys Rev Lett 72:2486–2489
177. Stockman MI, Pandey LN, George TF (1996) Inhomogeneous localization of polar eigenmodes in fractals. Phys Rev B 53:2183–2186
178. Stockman MI (1997) Chaos and spatial correlations for dipolar eigenproblem. Phys Rev Lett 79:4562–4565

179. Stockman MI (1997) Inhomogeneous eigenmode localization, chaos, and correlations in large disordered clusters. Phys Rev E 56:6494–6507
180. Ginzburg P, Berkovitch N, Nevet A, Shor I, Orenstein M (2011) Resonances on-demand for plasmonic nano-particles. Nano Lett 11:2329–2333
181. Markel VA, Muratov LS, Stockman MI, George TF (1991) Theory and numerical simulation of optical properties of fractal clusters. Phys Rev B 43:8183
182. Stockman MI (2006) Electromagnetic theory of SERS. In: Kneipp MMK, Kneipp H (eds) Surface enhanced Raman scattering, vol 103. Springer, Heidelberg, pp 47–66
183. Awada C, Barbillon G, Charra F, Douillard L, Greffet JJ (2012) Experimental study of hot spots in gold/glass nanocomposite films by photoemission electron microscopy. Phys Rev B 85:045438–1–6
184. Stockman M, George T (1994) Photon tunneling microscope reveals local hot-spots. Phys World 7:27–28
185. Cang H, Labno A, Lu CG, Yin XB, Liu M, Gladden C, Liu YM, Zhang X (2011) Probing the electromagnetic field of a 15-nanometre hotspot by single molecule imaging. Nature 469:385–388
186. McLeod A, Weber-Bargioni A, Zhang Z, Dhuey S, Harteneck B, Neaton JB, Cabrini S, Schuck PJ (2011) Nonperturbative visualization of nanoscale plasmonic field distributions via photon localization microscopy. Phys Rev Lett 106:037402
187. Yildiz A, Forkey JN, McKinney SA, Ha T, Goldman YE, Selvin PR (2003) Myosin V walks hand-over-hand: single fluorophore imaging with 1.5-nm localization. Science 300:2061–2065
188. Stockman MI, Kling MF, Kleineberg U, Krausz F (2007) Attosecond nanoplasmonic field microscope. Nat Photonics 1:539–544
189. Klar T, Perner M, Grosse S, von Plessen G, Spirkl W, Feldman J (1998) Surface-plasmon resonances in single metallic nanoparticles. Phys Rev Lett 80:4249–4252
190. Lehmann J, Merschdorf M, Pfeiffer W, Thon A, Voll S, Gerber G (2000) Surface plasmon dynamics in silver nanoparticles studied by femtosecond time-resolved photoemission. Phys Rev Lett 85:2921–2924
191. Bosbach J, Hendrich C, Stietz F, Vartanyan T, Trager F (2002) Ultrafast dephasing of surface plasmon excitation in silver nanoparticles: influence of particle size, shape, and chemical surrounding. Phys Rev Lett 89:257404–1–4
192. Hendrich C, Bosbach J, Stietz F, Hubenthal F, Vartanyan T, Trager F (2003) Chemical interface damping of surface plasmon excitation in metal nanoparticles: a study by persistent spectral hole burning. Appl Phys B 76:869–875
193. Zentgraf T, Christ A, Kuhl J, Giessen H (2004) Tailoring the ultrafast dephasing of quasiparticles in metallic photonic crystals. Phys Rev Lett 93:243901–1–4
194. Novotny L, Hecht B (2006) Principles of nano-optics. Cambridge University Press, Cambridge/New York
195. Ono A, Kato J, Kawata S (2005) Subwavelength optical imaging through a metallic nanorod array. Phys Rev Lett 95:267407–1–4
196. Shvets G, Trendafilov S, Pendry JB, Sarychev A (2007) Guiding, focusing, and sensing on the subwavelength scale using metallic wire arrays. Phys Rev Lett 99:053903–1–4
197. Pendry JB (2003) Perfect cylindrical lenses. Opt Express 11:755–760
198. Liu Z, Lee H, Xiong Y, Sun C, Zhang X (2007) Far-field optical hyperlens magnifying sub-diffraction-limited objects. Science 315:1686
199. Stockman MI, Faleev SV, Bergman DJ (2002) Coherent control of femtosecond energy localization in nanosystems. Phys Rev Lett 88:067402–1–4
200. Tannor DJ, Rice SA (1985) Control of selectivity of chemical reaction via control of wave packet evolution. J Chem Phys 83:5013–5018
201. Brumer P, Shapiro M (2003) Principles of the quantum control of molecular processes. Wiley, New York
202. Judson RS, Rabitz H (1992) Teaching lasers to control molecules. Phys Rev Lett 68:1500

203. Kurizki G, Shapiro M, Brumer P (1989) Phase-coherent control of photocurrent directionality in semiconductors. Phys Rev B 39:3435–3437
204. Weinacht TC, Ahn J, Bucksbaum PH (1999) Controlling the shape of a quantum wavefunction. Nature 397:233–235
205. Brumer P, Shapiro M (1992) Laser control of molecular processes. Ann Rev Phys Chem 43:257–282
206. Rabitz H, de Vivie-Riedle R, Motzkus M, Kompa K (2000) Chemistry – whither the future of controlling quantum phenomena? Science 288:824–828
207. Geremia JM, Rabitz H (2002) Optimal identification of Hamiltonian information by closed-loop laser control of quantum systems. Phys Rev Lett 89:263902–1–4
208. Nguyen NA, Dey BK, Shapiro M, Brumer P (2004) Coherent control in nanolithography: Rydberg atoms. J Phys Chem A 108:7878–7888
209. Shapiro M, Brumer P (2006) Quantum control of bound and continuum state dynamics. Phys Rep 425:195–264
210. Assion A, Baumert T, Bergt M, Brixner T, Kiefer B, Seyfried V, Strehle M, Gerber G (1998) Control of chemical reactions by feedback-optimized phase-shaped femtosecond laser pulses. Science 282:919–922
211. Bartels R, Backus S, Zeek E, Misoguti L, Vdovin G, Christov IP, Murnane MM, Kapteyn HC (2000) Shaped-pulse optimization of coherent emission of high-harmonic soft X-rays. Nature 406:164–166
212. Dudovich N, Oron D, Silberberg Y (2002) Single-pulse coherently controlled nonlinear Raman spectroscopy and microscopy. Nature 418:512–514
213. Brixner T, Krampert G, Pfeifer T, Selle R, Gerber G, Wollenhaupt M, Graefe O, Horn C, Liese D, Baumert T (2004) Quantum control by ultrafast polarization shaping. Phys Rev Lett 92:208301–1–4
214. Durach M, Rusina A, Nelson K, Stockman MI (2007) Toward full spatio-temporal control on the nanoscale. Nano Lett 7:3145–3149
215. Volpe G, Cherukulappurath S, Parramon RJ, Molina-Terriza G, Quidant R (2009) Controlling the optical near field of nanoantennas with spatial phase-shaped beams. Nano Lett 9:3608–3611
216. Gjonaj B, Aulbach J, Johnson PM, Mosk AP, Kuipers L, Lagendijk A (2011) Active spatial control of plasmonic fields. Nat Photonics 5:360–363
217. Stockman MI, Hewageegana P (2005) Nanolocalized nonlinear electron photoemission under coherent control. Nano Lett 5:2325–2329
218. Sukharev M, Seideman T (2006) Phase and polarization control as a route to plasmonic nanodevices. Nano Lett 6:715–719
219. Aeschlimann M, Bauer M, Bayer D, Brixner T, de Abajo FJG, Pfeiffer W, Rohmer M, Spindler C, Steeb F (2007) Adaptive subwavelength control of nano-optical fields. Nature 446:301–304
220. Bauer M, Wiemann C, Lange J, Bayer D, Rohmer M, Aeschlimann M (2007) Phase propagation of localized surface plasmons probed by time-resolved photoemission electron microscopy. Appl Phys A 88:473–480
221. Aeschlimann M, Bauer M, Bayer D, Brixner T, Cunovic S, Dimler F, Fischer A, Pfeiffer W, Rohmer M, Schneider C, Steeb F, Struber C, Voronine DV (2010) Spatiotemporal control of nanooptical excitations. Proc Natl Acad Sci U S A 107:5329–5333
222. Li X, Stockman MI (2008) Highly efficient spatiotemporal coherent control in nanoplasmonics on a nanometer-femtosecond scale by time reversal. Phys Rev B 77:195109–1–10
223. Derode A, Tourin A, de Rosny J, Tanter M, Yon S, Fink M (2003) Taking advantage of multiple scattering to communicate with time-reversal antennas. Phys Rev Lett 90:014301–1–4
224. Lerosey G, de Rosny J, Tourin A, Derode A, Montaldo G, Fink M (2004) Time reversal of electromagnetic waves. Phys Rev Lett 92:193904–1–3
225. Lerosey G, de Rosny J, Tourin A, Fink M (2007) Focusing beyond the diffraction limit with far-field time reversal. Science 315:1120–1122

226. Stockman MI (2006) Electromagnetic theory of SERS. In: Kneipp K, Moskovits M, Kneipp H (eds) Surface Enhanced Raman scattering – physics and applications. Springer, Heidelberg/New York/Tokyo, pp 47–66
227. Stockman MI, Pandey LN, Muratov LS, George TF (1995) Optical-absorption and localization of eigenmodes in disordered clusters. Phys Rev B 51:185–195
228. Landau LD, Lifshitz EM (1975) The classical theory of fields. Pergamon, Oxford, New York
229. Kubo A, Pontius N, Petek H (2007) Femtosecond microscopy of surface plasmon polariton wave packet evolution at the silver/vacuum interface. Nano Lett 7:470–475
230. Verhagen E, Kuipers L, Polman A (2007) Enhanced nonlinear optical effects with a tapered plasmonic waveguide. Nano Lett 7:334–337
231. Sukharev M, Seideman T (2007) Coherent control of light propagation via nanoparticle arrays. J Phys B 40:S283–S298
232. Wefers MM, Nelson KA (1993) Programmable phase and amplitude femtosecond pulse shaping. Opt Lett 18:2032–2034
233. Feurer T, Vaughan JC, Nelson KA (2003) Spatiotemporal coherent control of lattice vibrational waves. Science 299:374–377
234. Babajanyan AJ, Margaryan NL, Nerkararyan KV (2000) Superfocusing of surface polaritons in the conical structure. J Appl Phys 87:3785–3788
235. Gramotnev DK, Vogel MW, Stockman MI (2008) Optimized nonadiabatic nanofocusing of plasmons by tapered metal rods. J Appl Phys 104:034311–1–8
236. Nomura W, Ohtsu M, Yatsui T (2005) Nanodot coupler with a surface plasmon polariton condenser for optical far/near-field conversion. Appl Phys Lett 86:181108–1–3
237. Yin LL, Vlasko-Vlasov VK, Pearson J, Hiller JM, Hua J, Welp U, Brown DE, Kimball CW (2005) Subwavelength focusing and guiding of surface plasmons. Nano Lett 5:1399–1402
238. Mailloux RJ (2005) Phased array antenna handbook. Artech House, Boston
239. Lerosey G, de Rosny J, Tourin A, Derode A, Fink M (2006) Time reversal of wideband microwaves. Appl Phys Lett 88:154101–1–3
240. Stockman MI (2008) Ultrafast nanoplasmonics under coherent control. New J Phys 10:025031–1–20
241. Kao TS, Jenkins SD, Ruostekoski J, Zheludev NI (2011) Coherent control of nanoscale light localization in metamaterial: creating and positioning isolated subwavelength energy hot spots. Phys Rev Lett 106:085501–1–4
242. Bauer M, Schmidt O, Wiemann C, Porath R, Scharte M, Andreyev O, Schonhense G, Aeschlimann M (2002) Time-resolved two photon photoemission electron microscopy. Appl Phys B 74:223–227
243. Brixner T, Gerber G (2001) Femtosecond polarization pulse shaping. Opt Lett 26:557–559
244. Brixner T, Krampert G, Niklaus P, Gerber G (2002) Generation and characterization of polarization-shaped femtosecond laser pulses. Appl Phys B 74:S133–S144
245. Atwater HA (2007) The promise of plasmonics. Sci Am 296:56–63
246. Anker JN, Hall WP, Lyandres O, Shah NC, Zhao J, Duyne RPV (2008) Biosensing with plasmonic nanosensors. Nat Mater 7:442–453
247. Israel A, Mrejen M, Lovsky Y, Polhan M, Maier S, Lewis A (2007) Near-field imaging probes electromagnetic waves. Laser Focus World 43:99–102
248. Challener WA, Peng C, Itagi AV, Karns D, Peng W, Peng Y, Yang X, Zhu X, Gokemeijer NJ, Hsia YT, Ju G, Rottmayer RE, Seigler MA, Gage EC (2009) Heat-assisted magnetic recording by a near-field transducer with efficient optical energy transfer. Nat Photonics 3:220–224
249. Nagatani N, Tanaka R, Yuhi T, Endo T, Kerman K, Takamura Y, Tamiya E (2006) Gold nanoparticle-based novel enhancement method for the development of highly sensitive immunochromatographic test strips. Sci Technol Adv Mater 7:270–275
250. Hirsch LR, Stafford RJ, Bankson JA, Sershen SR, Rivera B, Price RE, Hazle JD, Halas NJ, West JL (2003) Nanoshell-mediated near-infrared thermal therapy of tumors under magnetic resonance guidance. Proc Natl Acad Sci U S A 100:13549–13554
251. Park I-Y, Kim S, Choi J, Lee D-H, Kim Y-J, Kling MF, Stockman MI, Kim S-W (2011) Plasmonic generation of ultrashort extreme-ultraviolet light pulses. Nat Photonics 5:677–681

252. Kahng D (1963) Electric field controlled semiconductor device. US Patent 3,102,230
253. Tsividis Y (1999) Operation and modeling of the MOS transistor. McGraw-Hill, New York
254. Stockman MI, Bergman DJ (2009) Surface plasmon amplification by stimulated emission of radiation (spaser). US Patent 7,569,188
255. Stockman MI (2008) Spasers explained. Nat Photonics 2:327–329
256. Noginov MA, Zhu G, Belgrave AM, Bakker R, Shalaev VM, Narimanov EE, Stout S, Herz E, Suteewong T, Wiesner U (2009) Demonstration of a spaser-based nanolaser. Nature 460:1110–1112
257. Hill MT, Marell M, Leong ESP, Smalbrugge B, Zhu Y, Sun M, van Veldhoven PJ, Geluk EJ, Karouta F, Oei Y-S, Nötzel R, Ning C-Z, Smit MK (2009) Lasing in metal-insulator-metal sub-wavelength plasmonic waveguides. Opt Express 17:11107–11112
258. Oulton RF, Sorger VJ, Zentgraf T, Ma R-M, Gladden C, Dai L, Bartal G, Zhang X (2009) Plasmon lasers at deep subwavelength scale. Nature 461:629–632
259. Ma R-M, Oulton RF, Sorger VJ, Bartal G, Zhang X (2010) Room-temperature sub-diffraction-limited plasmon laser by total internal reflection. Nat Mater 10:110–113
260. Flynn RA, Kim CS, Vurgaftman I, Kim M, Meyer JR, Mäkinen AJ, Bussmann K, Cheng L, Choa FS, Long JP (2011) A room-temperature semiconductor spaser operating near 1.5 micron. Opt Express 19:8954–8961
261. Hill MT, Oei Y-S, Smalbrugge B, Zhu Y, de Vries T, van Veldhoven PJ, van Otten FWM, Eijkemans TJ, Turkiewicz JP, de Waardt H, Geluk EJ, Kwon S-H, Lee Y-H, Noetzel R, Smit MK (2007) Lasing in metallic-coated nanocavities. Nat Photonics 1:589–594
262. Gordon JA, Ziolkowski RW (2007) The design and simulated performance of a coated nano-particle laser. Opt Express 15:2622–2653
263. Bergman DJ, Stroud D (1980) Theory of resonances in the electromagnetic scattering by macroscopic bodies. Phys Rev B 22:3527–3539
264. Plum E, Fedotov VA, Kuo P, Tsai DP, Zheludev NI (2009) Towards the lasing spaser: controlling metamaterial optical response with semiconductor quantum dots. Opt Express 17:8548–8551
265. Seidel J, Grafstroem S, Eng L (2005) Stimulated emission of surface plasmons at the interface between a silver film and an optically pumped dye solution. Phys Rev Lett 94:177401–1–4
266. Noginov MA, Zhu G, Mayy M, Ritzo BA, Noginova N, Podolskiy VA (2008) Stimulated emission of surface plasmon polaritons. Phys Rev Lett 101:226806–1–4
267. Li K, Li X, Stockman MI, Bergman DJ (2005) Surface plasmon amplification by stimulated emission in nanolenses. Phys Rev B 71:115409–1–4
268. Dong ZG, Liu H, Li T, Zhu ZH, Wang SM, Cao JX, Zhu SN, Zhang X (2008) Resonance amplification of left-handed transmission at optical frequencies by stimulated emission of radiation in active metamaterials. Opt Express 16:20974–20980
269. Wegener M, Garcia-Pomar JL, Soukoulis CM, Meinzer N, Ruther M, Linden S (2008) Toy model for plasmonic metamaterial resonances coupled to two-level system gain. Opt Express 16:19785–19798
270. Fang A, Koschny T, Wegener M, Soukoulis CM (2009) Self-consistent calculation of metamaterials with gain. Phys Rev B (Rapid Commun) 79:241104(R)–1–4
271. Wuestner S, Pusch A, Tsakmakidis KL, Hamm JM, Hess O (2010) Overcoming losses with gain in a negative refractive index metamaterial. Phys Rev Lett 105:127401–1–4
272. Chang SW, Ni CYA, Chuang SL (2008) Theory for bowtie plasmonic nanolasers. Opt Express 16:10580–10595
273. Zheludev NI, Prosvirnin SL, Papasimakis N, Fedotov VA (2008) Lasing spaser. Nat Photonics 2:351–354
274. Protsenko IE, Uskov AV, Zaimidoroga OA, Samoilov VN, O'Reilly EP (2005) Dipole nanolaser. Phys Rev A 71:063812
275. Ambati M, Nam SH, Ulin-Avila E, Genov DA, Bartal G, Zhang X (2008) Observation of stimulated emission of surface plasmon polaritons. Nano Lett 8:3998–4001
276. Zhou ZK, Su XR, Peng XN, Zhou L (2008) Sublinear and superlinear photoluminescence from Nd doped anodic aluminum oxide templates loaded with Ag nanowires. Opt Express 16:18028–18033

277. Noginov MA, Podolskiy VA, Zhu G, Mayy M, Bahoura M, Adegoke JA, Ritzo BA, Reynolds K (2008) Compensation of loss in propagating surface plasmon polariton by gain in adjacent dielectric medium. Opt Express 16:1385–1392
278. Bolger PM, Dickson W, Krasavin AV, Liebscher L, Hickey SG, Skryabin DV, Zayats AV (2010) Amplified spontaneous emission of surface plasmon polaritons and limitations on the increase of their propagation length. Opt Lett 35:1197–1199
279. Noginov MA, Zhu G, Bahoura M, Adegoke J, Small C, Ritzo BA, Drachev VP, Shalaev VM (2007) The effect of gain and absorption on surface plasmons in metal nanoparticles. Appl Phys B 86:455–460
280. Noginov MA (2008) Compensation of surface plasmon loss by gain in dielectric medium. J Nanophotonics 2:021855–1–17
281. Leon ID, Berini P (2010) Amplification of long-range surface plasmons by a dipolar gain medium. Nat Photonics 4:382–387
282. Ding K, Liu ZC, Yin LJ, Hill MT, Marell MJH, van Veldhoven PJ, Noetzel R, Ning CZ (2012) Room-temperature continuous wave lasing in deep-subwavelength metallic cavities under electrical injection. Phys Rev B 85:041301–1–5
283. Ding K, Yin L, Hill MT, Liu Z, van Veldhoven PJ, Ning CZ (2013) An electrical injection metallic cavity nanolaser with azimuthal polarization. Appl Phys Lett 102:041110–1–4
284. Ding K, Hill MT, Liu ZC, Yin LJ, van Veldhoven PJ, Ning CZ (2013) Record performance of electrical injection sub-wavelength metallic-cavity semiconductor lasers at room temperature. Opt Express 21:4728–4733
285. Kitur JK, Zhu G, Yu AB, Noginov MA (2012) Stimulated emission of surface plasmon polaritons on smooth and corrugated silver surfaces. J Opt 14:114015–1–8
286. Wu CY, Kuo CT, Wang CY, He CL, Lin MH, Ahn H, Gwo S (2011) Plasmonic green nanolaser based on a metal-oxide-semiconductor structure. Nano Lett 11:4256–4260
287. Lu Y-J, Kim J, Chen H-Y, Wu C, Dabidian N, Sanders CE, Wang C-Y, Lu M-Y, Li B-H, Qiu X, Chang W-H, Chen L-J, Shvets G, Shih C-K, Gwo S (2012) Plasmonic nanolaser using epitaxially grown silver film. Science 337:450–453
288. Oulton RF, Sorger VJ, Genov DA, Pile DFP, Zhang X (2008) A hybrid plasmonic waveguide for subwavelength confinement and long-range propagation. Nat Photonics 2:496–500
289. Li D, Stockman MI (2013) Electric spaser in the extreme quantum limit. Phys Rev Lett 110:106803–1–5
290. Brown RH, Twiss RQ (1956) A test of a new type of stellar interferometer on Sirius. Nature 178:1046–1048
291. Schawlow AL, Townes CH (1958) Infrared and optical masers. Phys Rev 112:1940
292. Kéna-Cohen S, Stavrinou PN, Bradley DDC, Maier SA (2013) Confined surface plasmon-polariton amplifiers. Nano Lett 13:1323–1329
293. Kneipp K, Moskovits M, Kneipp H (eds) (2006) Surface enhanced Raman scattering: physics and applications. Springer, Heidelberg/New York/Tokyo
294. Kneipp J, Kneipp H, Wittig B, Kneipp K (2010) Novel optical nanosensors for probing and imaging live cells. Nanomed Nanotechnol Biol Med 6:214–226
295. Dunmore FJ, Liu DZ, Drew HD, Dassarma S, Li Q, Fenner DB (1995) Observation of below-gap plasmon excitations in superconducting $YBa_2Cu_3O_7$ films. Phys Rev B 52:R731–R734
296. Schumacher D, Rea C, Heitmann D, Scharnberg K (1998) Surface plasmons and Sommerfeld-Zenneck waves on corrugated surfaces: application to high-T_c superconductors. Surf Sci 408:203–211
297. Tsiatmas A, Buckingham AR, Fedotov VA, Wang S, Chen Y, de Groot PAJ, Zheludev NI (2010) Superconducting plasmonics and extraordinary transmission. Appl Phys Lett 97:111106–1–3
298. Boltasseva A, Atwater HA (2011) Low-loss plasmonic metamaterials. Science 331:290–291
299. Shalaev VM (2007) Optical negative-index metamaterials. Nat Photonics 1:41–48
300. Zheludev NI (2011) A roadmap for metamaterials. Opt Photonics News 22:30–35
301. Stockman MI, Kurlayev KB, George TF (1999) Linear and nonlinear optical susceptibilities of Maxwell Garnett composites: Dipolar spectral theory. Phys Rev B 60:17071–17083

302. Meinzer N, Ruther M, Linden S, Soukoulis CM, Khitrova G, Hendrickson J, Olitzky JD, Gibbs HM, Wegener M (2010) Arrays of Ag split-ring resonators coupled to InGaAs single-quantum-well gain. Opt Express 18:24140–24151
303. Kretschmann E, Raether H (1968) Radiative decay of nonradiative surface plasmons excited by light. Z Naturforsch A 23:2135–2136
304. Heydari E, Flehr R, Stumpe J (2013) Influence of spacer layer on enhancement of nanoplasmon-assisted random lasing. Appl Phys Lett 102:133110–4
305. Kitur JK, Podolskiy VA, Noginov MA (2011) Stimulated emission of surface plasmon polaritons in a microcylinder cavity. Phys Rev Lett 106:183903–1–4
306. Bloch F (1929) Über die Quantenmechanik der Elektronen in Kristallgittern. Z Phys A 52:555–600
307. Ghafouri-Shiraz H (2003) Distributed feedback laser diodes and optical tunable filters. Wiley, West Sussex/Hoboken
308. van Beijnum F, van Veldhoven PJ, Geluk EJ, de Dood MJA, 't Hooft GW, van Exter MP (2013) Surface plasmon lasing observed in metal hole arrays. Phys Rev Lett 110:206802–1–5
309. Zhou W, Dridi M, Suh JY, Kim CH, Co DT, Wasielewski MR, Schatz GC, Odom TW (2013) Lasing action in strongly coupled plasmonic nanocavity arrays. Nat Nanotechnol 8:506–511
310. Stockman MI (2013) Lasing spaser in two-dimensional plasmonic crystals. NPG Asia Mater 5:e71
311. Anderson PW (1958) Absence of diffusion in certain random lattices. Phys Rev 109:1492–1505